Precise single cell monitoring reveals principles of cell growth

by

Sungmin Son

Mechanical Engineering, M.S.,
Massachusetts Institute of Technology, 2008

Submitted to the Department of Mechanical Engineering
in partial fulfillment of the requirements for the degree of

Doctor of Philosophy in Mechanical Engineering

at the

MASSACHUSETTS INSTITUTE OF TECHNOLOGY

June 2013

Author .....
Department of Mechanical Engineering
February 28, 2013

Certified by .....
Scott R. Manalis
Professor
Thesis Supervisor

Accepted by .....
David E. Hardt
Chairman, Department Committee on Graduate Theses

Precise single cell monitoring reveals principles of cell growth

by

Sungmin Son

Submitted to the Department of Mechanical Engineering
on February 28, 2013, in partial fulfillment of the
requirements for the degree of
Doctor of Philosophy in Mechanical Engineering

Abstract

Accumulation of mass is a fundamental cellular process that is associated with metabolism, signaling and regulation. Despite the wealth of knowledge in molecular processes the principles of growth in mammalian cells are poorly understood since growth has never been monitored with high precision. Development of the Suspended Microchannel Resonator (SMR), a microfluidic mass measurement system, enables femtogram cell mass resolution. With this, we developed a method to simultaneously measure molecular signals and single cell mass with high precision over multiple generations.

First we investigated how cells control their size. It is known that proliferating cells govern the rate at which they build their biomass and divide, but the mechanism that is used to maintain size homeostasis remains unclear. We obtained over 1,000 hours of growth data from mouse lymphoblast and pro-B-cell lymphoid cell lines. Cell lineage analysis revealed a decrease in the growth rate variability at the G1/S phase transition, which suggests the presence of a growth rate threshold for maintaining size homeostasis. We could also identify unexpected aspects of the growth trajectory such as continuation of growth during M phase, large and switch-like drop in growth rate upon cytokinesis.

We next studied the metabolic and energetic requirements necessary for cell growth by monitoring immediate single cell growth response to nutrient depletion. To this end, we developed a method to gently exchange the fluid surrounding a cell while constantly monitoring cell growth. We observed that cells immediately change the growth rate upon depletion of key nutrients such as glucose or glutamine. The growth rate change was surprisingly large but restored upon repletion of nutrients. This implies that immediate growth response integrates both loss of nutrient uptake and signaling associated with metabolism of the particular nutrient.

We developed two platforms to measure single cell growth in high throughput. These advancements will broaden the application of the SMR to the study of primary cells or cancer cells.

Thesis supervisor: Scott R. Manalis
Title: Professor

Acknowledgements

First and foremost, I would like to thank Professor Scott Manalis for infusing his academic vision in me - he really believes in the value of precision engineering and measurement in biology and demonstrates it in the best way possible. His emphasis on the synergetic integration of engineering and biology was a paradigm shift for me, and made me reconsider my carrier as a robotics engineer. Furthermore, he developed me to become a mature biological engineer by all the opportunities and resources he provided and without his guidance in writing, communication, leadership, and ethics, it would not have been possible.

I am also grateful to Professor Marc Kirschner for his guidance in cell biology. As an expert in cell growth and cycle, he has helped advance my thesis research from what could have been a task of precision measurement to elucidation of cell growth principles. Beyond the wealth of knowledge in cell growth and cycle, he also provided the framework of biological thinking, sound experiment design, and story-telling. Professors Alan Grodzinsky and Mark Bathe have been fantastic to have as members of my thesis committee. I'm grateful for their invaluable advice and suggestions that helped me to shape the research. I want to thank Professor Matt Vander Heiden for the guidance and stimulating ideas he provided in the nutrient depletion project.

In the Manalis lab, I was privileged to work with almost every member in my thesis research or various other projects and had all the fun one can possibly have in collaboration. In particular, Thomas Burg is a pioneer of the SMR and taught me its details. Will Grover was an expert in microfluidics and a great resource for the HPLC and cell rotary chip project. Scott Knudsen oversaw the lab and helped me focus only on research. Jungchul Jay Lee taught me cantilever theories and electronics. Wesley Weng shared invaluable knowhow about system building for single cell growth monitoring. Nate Cermak provided an extensive labview code that made data acquisition and processing so much easier and also gave much advice on data analysis and growth modeling. Mark Stevens helped me in every aspect of the

nutrient depletion project, and he was also a wonderful resource for brainstorming, writing, and presentation. Steve Wasserman answered almost any question I had in optics and electronics. Kristopher Payer oversaw the fabrication of the SMR chips and significantly expedited my thesis work. I have also been privileged to work with fantastic UROPs who not only helped my work but also gave me a chance to develop management skills: I thank Jared, Jisoo, Nikita, and Sherry. Special thanks also go to my collaborators Amit Tzur, Paul Jorgensen, Ran Kafri, and Christopher Kempes.

Outside of lab I have been extremely fortunate to be surrounded by wonderful friends. James Penn bulked up not only my body but also my maturity and soul by his training in the gym and also by unfailing friendship he demonstrated through all the adventures we shared. Sungho Lee and Chris Bae have been wonderful colleagues who were always there for me to count on. Casey Adkisson and Pablo Solis were the best roommates and also quirky prodigies who are, in our own definition, in the fast lane to success in life. Kawin Setsompop has infused fun and optimism into me and also helped my professional development. I am also grateful for the friends I made through KGSAME, with whom I share the same background and similar perspectives in life.

Finally, I would like to thank my family, especially my parents and my brother. They believed in me more than I believed in myself and without their love and support, I would not have made this far.

I would like to thank the financial support from Kwanjung Scholarship Foundation.

Contents

1. Introduction 16

1.1 Background 16

1.1.1 Cell growth and size regulation 16

1.1.2 Growth response to nutrient deprivation 18

1.2 SMR description and measurements 20

1.2.1 Device concept and basic operation 20

1.2.2 Application of the SMR to single-cell growth 20

2. Measurement of single mammalian cell growth during the complete cell-cycle 23

2.1 Scale up of the SMR for mammalian cell measurement 23

2.2 Flow configuration of dynamic trap 24

2.3 Shear stress 31

2.4 Control of pH 33

2.5 Improving measurement precision 36

2.6 In-situ imaging 41

3. Principles in cell growth 48

3.1 Growth rate threshold 48

3.2 Noise in growth and size homeostasis 62

4. Higher-throughput growth measurement 69

4.1 Simultaneous measurement of a series of cells 70

4.2 Trap-and-release 75

5. Growth response to nutrient deprivation 83

5.1 Method of fluid exchange 84

5.2 Growth response to nutrient depletion 90

A. Supplementary Figures 97

A.1 Chapter 2 Supplementary Figures 97

A.2 Chapter 4 Supplementary Figures 101

A.3 Chapter 5 Supplementary Figures 102

List of Figures

2-1: Leakage flow induced by the hydrostatic pressure.. 25
2-2: Single cell loading in SMR for long-term growth measurement. 27
2-3: The schematic of dynamic trapping.. 28
2-4: Lineage growth trajectories of L1210 cells 28
2-5: Accumulated growth trajectories of L1210 single cells 30
2-6: Rapid loss of mass 30
2-7: Interdivision time of the cells grown in the SMR and the doubling time of the bulk culture 31
2-8: The effect of shear stress on cell growth 32
2-9: The effect of shear stress on bulk growth parameters.. 32
2-10: pH stability in the bypass reservoir 34
2-11: Lineage growth trajectories of L1210 and FL5.12 cells. 35
2-12: Schematic of the position-dependent error 36
2-13: Hydrodynamic focusing 37
2-14: Frequency shift during cytokinesis 38
2-15: Resonance frequency shifts of the second flexural bending mode upon point mass transit through a cantilever. 39
2-16: Measurement precision of the first and second bending mode. 40
2-17: SMR-optical system for single cell fluorescence measurement. 42
2-18: Validation of the shot-noise limited system 43
2-19: Sensitivity of the SMR optical system 44

2-20: Precision of the SMR optical system 45
2-21: Mass and fluorescent of the L1210 cell population. 46
2-22: Size distributions of steady-state cell cultures 46
3-1: Measurement of single cell growth and cell cycle progression 49
3-2: Mass and fluorescent signals from the cell cycle reporters were acquired from a L1210 mouse lymphoblast cell over four generations 50
3-3: Growth rate versus cell mass of a cell from the newborn stage through division 51
3-4: Growth rate acceleration ratio at the G1-S transition 52
3-5: Evidence for a growth rate threshold 53
3-6: Growth rate trajectories of cell lineages. 54
3-7: Coefficient of variance for buoyant mass and growth rate at various points in the cell cycle 55
3-8: Time at G1/S phase transition versus early G1 growth rate 56
3-9: G1 duration versus early G1 growth rate in media with limited isoleucine. 57
3-10: Interdivision and G1 time versus newborn cell size. 57
3-11: Single cell growth rate trajectories for a lineage of eight FL5.12 cells. 58
3-12: Time at G1/S phase transition versus early G1 growth rate for FL5.12 cells. 59
3-13: Cell cycle time versus mass at birth of FL5.12 pro–B–cell lymphoid cells.. 59
3-14: Growth of L1210 cells in media with limited isoleucine 60
3-15: Growth of L1210 cells in media with limited isoleucine. 60
3-16: Size distributions of a culture grown in limited isoleucine media 61
3-17: Lineage trajectories for cells grown in normal and media with limited isoleucine 61
3-18: Specific growth rate trajectories of L1210 cells for 5 generations. 62
3-19: Growth during division. 63
3-20: Discontinuity in specific growth rate occurs at cytokinesis 64
3-21: Growth rate is symmetric after division 65

3-22: Growth of the related progenies 65
3-23: Representative growth curves with different initial specific growth rate at newborn. 66
3-24: Negative correlation between the interdivision time and specific growth rate in newborn. 67
4-1: Micrograph of the SMR with the extended serpentine buried channel.. 71
4-2: Deconvolution of multiple peaks 72
4-3: Mass estimation error of the deconvolution method 73
4-4: Flow rate of the cell decreases with the size. 74
4-5: Skipped mass measurement due to the flow rate variation. 74
4-6: Illustration and micrograph of the SMR / trap-and-release 77
4-7: Illustration of the trap and release structure. 78
4-8: Net flow rate change as a function of total number of traps and their occupation 79
4-9: The fate of trap depends on the flow path of cells. 80
4-10: Illustration of back trap in sequence 80
4-11: Illustration of the SMR/trap-and-release array 81
5-1: Illustration of fluid exchange 85
5-2: Growth of a L1210 cell upon depletion and repletion of glutamine.. 86
5-3: Growth of FL5.12 cells upon depletion of IL-3. 87
5-4: Illustration of the instantaneous fluid exchange method 88
5-5: Environmental exchange negative control 89
5-6: Environmental exchange positive control 90
5-7: Bulk culture proliferation or volume curves for depletions of glucose and glutamine in L1210 and FL5.12 cell lines 91
5-8: Instantaneous growth response to partial nutrient depletion. 93
5-9: Growth rate change upon complete depletions of specific nutrients. 94
5-10: Average growth rate change upon nutrient depletions 95
A-1 BCECF calibration 98
A-2 Growth of FL5.12 cells under different type of stress 99
A-3 Peak shape as a determinant of the path of cell transit 100

A-4 A giant cell.....101
A-5 Instantaneous growth rate estimation error.....102

List of Tables

4.1 Trap-and-release design dimensions.....78

Chapter 1

Introduction

1.1 Background

1.1.1 Cell growth and size regulation

Cell size is one of the most intuitive phenotypes associated with various cell behaviors and pathologies. Within an organism, different types of cells come in wide range of size such as from blood cells to neurons but the size variation within the particular cell types remains fairly tight. When cells cannot maintain the size, it often leads to abnormal behaviors, such as senescence, which are associated with pathological conditions [1]. Taken together, these observations imply that cells have a mechanism to determine and regulate the size for optimal function.

Even though the precise mechanism has remained elusive, it is believed that the coordination of cell growth and division is responsible for size regulation: Fast growth with slow division makes big cells, whereas slow growth with fast division makes small cells. Several studies from unicellular organisms such as yeast have found "cell-size checkpoints" that delays division until cells have achieved a minimal size [2]. Mainly two different mechanisms are suggested as a 'sizer' for cells: i) measurement of certain molecules whose diffusion time can be monitored to sense

spatial scales, and ii) measurement of the rate of production of a limiting cell cycle activator. Consistent with the dilution model, Moseley and colleagues found that fission yeast cells measure the amount of Pom1, a protein whose concentration is high at the ends of the elongated cells but falls off toward the center at their midsection, before committing to division [3]. Alternatively, the activator model envisions a molecule produced at a constant rate per unit of cytoplasm which becomes progressively concentrated in an organelle of fixed volume (e.g., the nucleus) or on target binding sites of fixed number (e.g., chromosomes). In budding yeast, Hartwell and colleagues found that more Cln3p accumulates as the cytosol increases in size but the size of the nucleus stays relatively constant, leading to a higher concentration of Cln3p in the nucleus, which then initiates G1-S transition [4]. However, independent observations of the constant nucleo-cytoplasmic volume ratio prior to Start undermined this hypothesis [5].

Despite evidence of a size checkpoint in yeast, the existence of an analogous size checkpoint in mammalian cells is controversial. Studies that look for size checkpoint by monitoring the correlation between size and G1 duration have produced conflicting results depending on cell type [6][7]. Other studies have shown that the growth of mammalian cells is limited by extracellular signals such as mitogens or growth factors rather than nutrients, suggesting that the size is controlled at the organismal level rather than at the single cell level [8]. Alternatively, evidence of size regulation could be found by measuring a property of how individual cells grow – e.g. whether their growth is linear or exponential. For linear growth, a cell would enlarge at a constant rate until it divides. But for exponential growth, the increase would be proportional to the cell's size [9]. In the latter case, the small but natural variations in size between two cells resulting from division would rapidly expand to create a population of cells with large size differences. So if cells are growing exponentially they must have a checkpoint to rein in growth and keep themselves within the observed narrow size range. However, the measurement of different cells yielded conflicting observations of growth trajectory [10][11].

Even recent studies with novel approaches draw incompatible conclusions regarding the size regulation of mammalian cells [12][13]. Researchers speculate that different types of cells might have different size regulation mechanisms. Fast-growing immune cells might behave more like yeast, relying on their own size-measuring mechanism, whereas nervous system cells mainly heed external cues [14]. Although reasonable, cell autonomous size regulation is not incompatible with growth driven by external factors and this is supported by the fact that these cells exhibit equally tight size variation.

To understand cell autonomous size regulation, one would ideally monitor the growth pattern of single cells in constant identical conditions and compare the cell-to-cell variation of growth to understand possible mechanisms of regulation. Towards this aim, we developed the advanced suspended microchannel resonator (SMR) to simultaneously measure growth and cell cycle of single cells during the complete cell-cycle.

1.1.2 Growth response to nutrient deprivation

In proliferating cells, growth is sustained by production of required energy and bio-molecular synthesis. In comparison to non-proliferating cells that maintain cellular homeostasis almost entirely through ATP-driven reactions, proliferating cells require more nutrients. Cells convert the majority of this increase nutrient uptake into biosynthetic building blocks, and coordinate the reactions necessary to transform them into the macromolecules essential for constructing a new cell [15]. In order to fulfill these special energetic and anabolic requirements necessary for growth, proliferating cells often alter their metabolism.

Two main examples of altered metabolism are increased utilization of glucose and glutamine. Warburg observed that cancer cells directed most of the carbon through glycolysis to lactate instead of metabolizing it by oxidative phosphorylation, a phenomenon termed the Warburg effect. Similar metabolic

alterations have also been identified in nontransformed cells during rapid proliferation [16][17]. These metabolic alterations are likely to support growth by elevating carbon flux through biosynthetic pathways by maintaining high level of metabolic intermediates. Despite the wealth of knowledge in bio-molecular changes in proliferating cells, however, the effect of those changes on growth dynamics has not been clearly described. In fact, we have yet to understand the minimum metabolic requirements for growth.

To understand the mechanisms behind the growth principles that are observed in the previous aim, it is crucial to find the link between the growth phenotype and metabolic programming. Thus far, most of the studies have only investigated the minimum requirement of growth. For this, people have qualitatively monitored the long-term effect of nutrient depletion in tissue or population of cells [18]. Even though this established the basic understanding of essential nutrients, readout of population-based long-term effect only reveals lumped response such as cell cycle arrest or apoptosis and fails to elucidate the role of metabolic programming in cell growth. To better understand this, we aim to monitor both immediate and long-term growth response from single cells upon withdrawal of crucial nutrients such as glucose or glutamine. We envision that this new depletion response information in the timescale never investigated before will not only hint at the processes taking place before the endpoint response such as cell cycle arrest but also help unravel the contribution of particular metabolisms to growth phenotype.

To this end, we developed a method to gently exchange the fluid surrounding a cell while constantly monitoring the growth in high precision. By quantifying the level of growth rate change upon withdrawal of several nutrients in various cell types, we gain insights into the role of particular metabolism in growth. In addition, to further investigate the mechanism that initiates the immediate growth response, we undertake several bulk measurements such as uptake of particular nutrient, or the change of transcription or intracellular ATP upon withdrawal.

1.2 SMR description and measurements

1.2.1 Device concept and basic operation

As described in Ref 22, cells suspended in solution flow through the SMR, and the resulting frequency shift depends on the mass and position of the particles. For dilute suspensions (typically < 10^5 cells/mL), this measurement yields a series of well-separated peaks whose heights are directly proportional to the cell's buoyant mass.

SMR devices are fabricated by creating buried channels in silicon-on-insulator wafers, followed by wafer thinning and dry etching to form suspended microchannels with 2-3 μm thin walls and a 15 μm fluid layer. Two hundred devices are fabricated and vacuum-packaged on a six-inch wafer with yields exceeding eighty percent. A getter layer prevents slow degradation of the on-chip vacuum due to outgassing. Integrated under each cantilever is an electrostatic drive electrode and the cantilever vibration is detected by the optical-lever. A gain controlled oscillator circuit is used to continuously track the resonance frequency.

1.2.2 Application of the SMR to single-cell growth measurement

The lack of consensus on how mammalian cells grow over generations largely stem from technical limitations [9]. Almost all prior studies of size homeostasis have monitored populations of cells. In a typical experiment, a population of cells would be synchronized in the cell cycle and then their average cell size monitored over time as the synchronized cells grew and eventually divided. Such experiments are limited not only by the poor resolution afforded by cell cycle synchronization and the unavoidable dispersion that follows, but also by artifacts produced by the synchronization methods themselves. Techniques for synchronization typically block nuclear division but not cell growth and inevitably result in oversized cells

[8][19]. In addition, prior studies have almost always measured cell volume, even though the accumulation of biomass is more directly related to anabolic processes such as protein synthesis. In the most comprehensive single cell study yet examining the interrelationship of cell growth and the cell cycle, single yeast cells were studied microscopically using a fluorescent reporter protein as a proxy for cell mass [20]. By correlating cell mass to specific cell cycle events, a cell size threshold for cell cycle entry was observed. Although protein content may be the dominant component within a cell, the use of a fluorescent reporter protein does not guarantee a precise readout of a cell's biomass. By contrast, advanced forms of microscopy for measuring cell dry mass have been applied to cell growth but they have generally suffered from limited precision [21].

As previously mentioned, the main motivation of direct cell growth measurement is to resolve the discord between the two growth models: linear or exponential. But, over the two-fold size range experienced by most proliferating cells, linear and exponential curves differ at most by 6% [12]. No current technology allows the growth curves of individual mammalian cells to be followed with sufficient precision. SMR is ideal in that it measures cell's mass and the shape of cells does not compromise the precision. It has the potential to weigh animal cells with a precision near 0.01%. Our aim is to employ the SMR in mammalian cell growth study to find the precise growth pattern in normal condition or in the situation where certain key nutrients are depleted.

Chapter 2

Measurement of single mammalian cell growth during the complete cell-cycle

It is previously demonstrated that the SMR has the potential to weigh particles with a precision near 0.01% [22]. By repeatedly measuring buoyant mass of the same cell the growth pattern of mammalian cell was able to be observed with high precision. However, current SMR system has several limitations that impede the stable long-term monitoring of cell growth. Moreover, it is not equipped to measure the cell cycle progression. In this chapter, we describe the limitations and series of technological advancements of the SMR that enable precise measurement of cell growth and cell cycle progression.

2.1 Scale up of the SMR for mammalian cell measurement

First, we scaled up the SMR from the cross-section of 3 by 8 μm^2 to 15 by 20 μm^2 to accommodate mouse white blood cells. Utmost design consideration was to maximize the mass sensitivity while minimizing the detection noise. Mass sensitivity is determined by

$$\frac{\Delta f}{f} \approx -\frac{1}{2}\frac{\Delta m}{m} \tag{2.1}$$

where f is the resonant frequency, m is total mass of the cantilever. Mass sensitivity can therefore be optimized by minimizing the mass of the cantilever, by maximizing the resonant frequency, or by minimizing the baseline frequency noise. The only free parameter that affects the mass was the length of cantilever since the cross-section was predetermined to fit the cells. Shorter cantilever would result in higher mass sensitivity. The resonant frequency also increases as the length gets shorter. On the other hand, the baseline frequency noise follows the opposite relationship. Even though the theoretical minimum of noise is determined by thermo-elastic noise [23], the practical limit of the system is an order of magnitude larger and affected by several factors such as feedback circuits, optical alignment of the laser. Among these, amplitude of cantilever oscillation largely affects the noise and the amplitude is determined by

$$a_n \approx \frac{L^3 Q}{EI} f_n \tag{2.2}$$

where a_n is the amplitude of oscillation at the nth vibration mode, L is the length, E is Young's modulus, Q is the quality factor, I is the second moment of inertia, f_n is the resonant frequency at the nth mode. Based on the simulation of oscillation amplitude and the empirically known baseline noise of existing cantilever, the length was carefully determined to 320μm to achieve the maximum mass resolution. Mass sensitivity and baseline noise was determined to 0.7Hz/pg and 100mHz at 1kHz bandwidth at the first mode.

2.2 Flow configuration of dynamic trap

In order to repeatedly monitor the mass of the same cell, a feedback algorithm was previously devised to reverse the direction of fluid flow upon detecting a cell

transiting through the SMR, thereby reintroducing the cell into the cantilever. Continuously alternating flow direction created a dynamic trap that allows for consecutive buoyant mass measurements of the same cell [24]. The ability to reintroduce the same cell relies mainly on two considerations: 1. precise flow control, 2. removal of other cells in the vicinity of the SMR to prevent them from interrupting the trapping of the original cell. These two considerations were currently not controlled reliably, thus limiting the average trapping time to tens of minutes.

The current system design suffered from the leakage flow that was often large enough to make the cell drift against the desired flow direction and escape from the dynamic trap. To find the source of the leakage flow an upright modular microscope was integrated into the system and the flow in the chip was monitored.

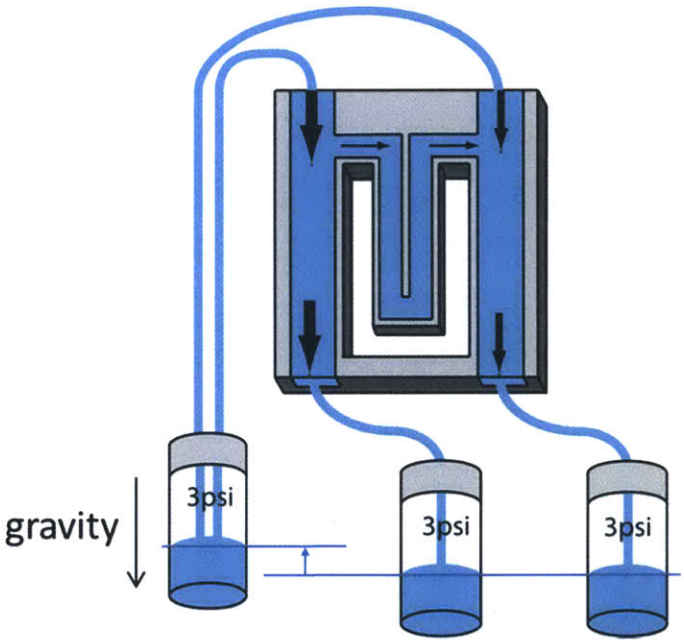

Figure 2-1: Leakage flow induced by the hydrostatic pressure. Even though the constant gauge pressure 3psi is applied to all three sample vials, elevation of fluid level in the upstream vial generates the leakage flow in the bypass channels and the buried channel. The flow rate is qualitatively shown with the thick (high) and thin (low) arrows. Mismatch of the net fluidic resistance between the two bypass channels and tubing results in different flow rate in either side of the channels.

This observation showed that if the fluid levels of upstream and downstream sample vials are not matched well, the variations in hydrostatic pressure can generate substantial leakage flow (Fig 2-1); for example, 1cm level difference would induce the pressure difference of ~0.015psi, which in turn generates the bypass channel leakage flow on the order of 100μm/s. To address this, sample vials were mounted in the manual vertical translation stages and adjusted to match the fluid level. This enabled us to almost stop the cell in the bypass channel and thus enhance the reliability of the dynamic trap.

Next, to prevent the other cells in the bypass channel from flowing into the SMR and interrupting the trapping of the original cell, a unique cell-loading scheme was devised (Fig 2-2). It loaded the sample from the downstream of the SMR and caused the entire sample plug to flow into the SMR by balancing the pressure applied across the sample bypass channel. It was crucial to make sure that none of the sample flows to the upstream direction pass the SMR since this can later flow downward to the vicinity of the SMR and interrupt the trapping. Once a cell was trapped the rest of the sample plug was in the downstream of the SMR and it was rinsed away by flow from the upstream direction during the dynamic trap.

Finally, the delivery of fresh media had to be considered to be able to grow a cell in a long term. When culturing cells in a long term, most of the microfluidic systems suffer from the change in media properties due to dehydration or acidification [25]. This is attributable to the air-permeable property of polydimethylsiloxane (PDMS), the material most commonly used in microfluidic systems[26]. It is not a concern for the SMR since it is made of the air-impermeable pyrex glass and silicon. On the other hand, the small fluid volume in the chip made it easy to be affected by molecules consumed or secreted by cells. The flow configuration of the new dynamic trap ensured that the downward flow replenishes the fresh media in one bypass channel every time a cell transits through the buried channel. As shown in Fig 2-3, the volume of replenishing media was determined by how much a cell travels to the downstream direction before it stops in the bypass channel. The frequency of replenishment was determined by how often cell transits through the SMR and this had to be carefully determined to minimize the shear-

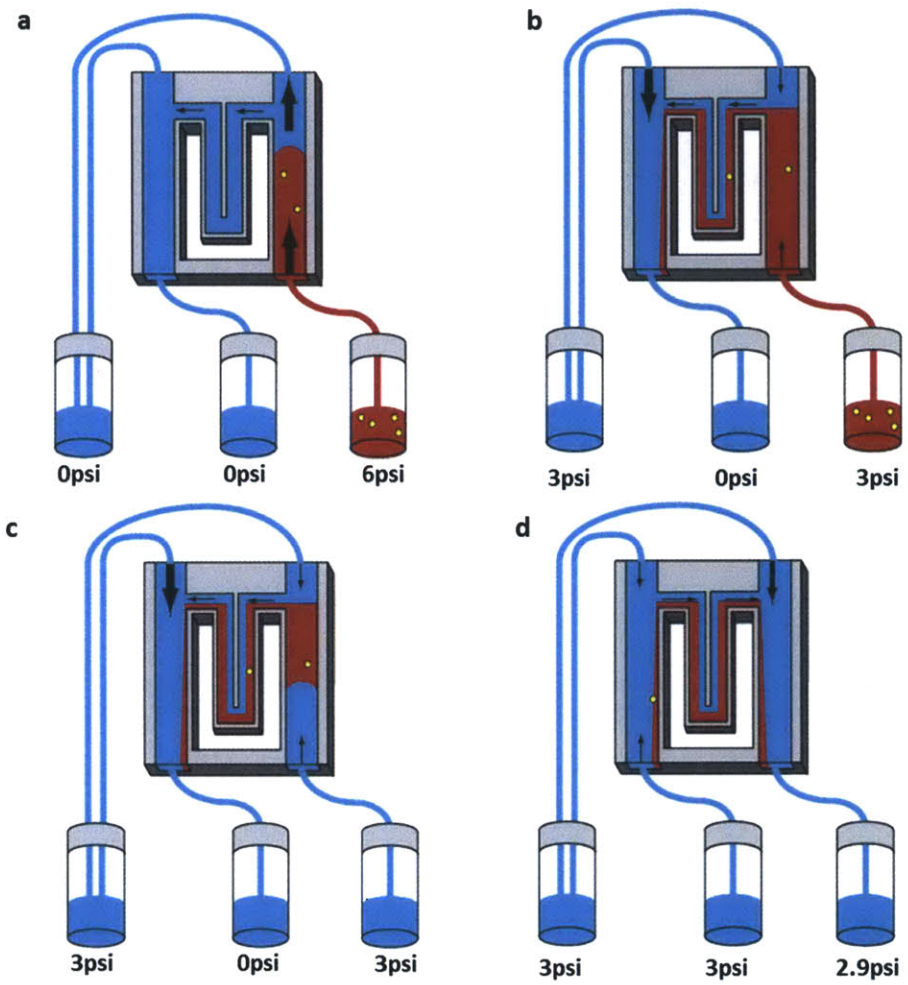

Figure 2-2: Single cell loading in SMR for long-term growth measurement. a) One upstream and two downstream vials are pressurized by independent pressure regulators. The system is primed with media (blue) before a cell is loaded. During cell loading, only the downstream vial on the right is pressurized (6 psi) and the sample plug (red) flows into the chip. The flow rate is qualitatively shown with the thick (high) and thin (low) arrows. b) As the sample plug moves toward the SMR, an equal pressure (3 psi) is applied to both the upstream and downstream vials. By balancing the pressure applied across the bypass, fluid from both the upstream and downstream directions enter the SMR. As a result, the flow path of the cell is confined to either the inner or outer region of the channel, which minimizes the position dependent error (see Supplemental Figure 2). c) After the sample has been completely loaded, all pressure sources are turned off and the sample vial is exchanged to media. The downstream vial is then pressurized again to keep the cell in transit. d) As soon as a cell of a desirable size transits through the SMR, the flow direction is reversed and the flow rate is reduced by elevating the downstream pressure to 2.9 psi. The sample plug on the right bypass channel is rinsed away by flow from the upstream direction. The liquid level in all three vials is matched in order to remove any leakage flow induced by variations in hydrostatic pressure.

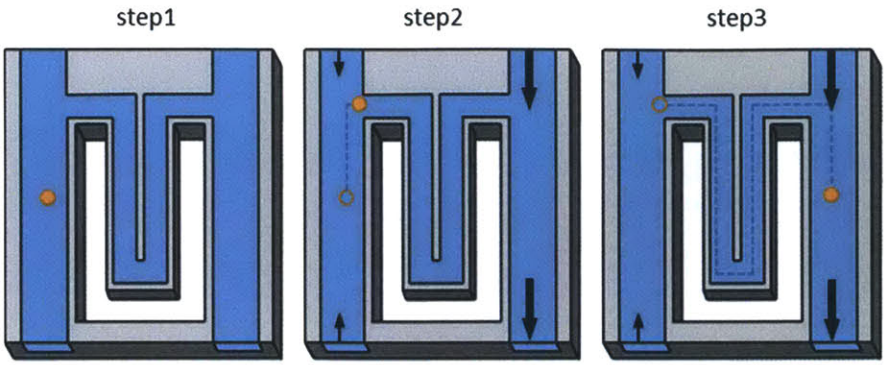

Figure 2-3: The schematic of dynamic trapping. It shows half of the full trap cycle. In step1, the cell rests in the bypass channel for 25 seconds. In step2, the cell slowly migrates toward the upstream direction at the speed of about 100μm/sec. This step can take up to ten seconds depending on the initial location of the cell. In the meantime, fresh media is replenished in the other side of the bypass channel at the flow rate of several nanoliters per second. In step3, the cell transits through the buried channel and stops at precisely controlled position in the bypass channel, which takes less than a second.

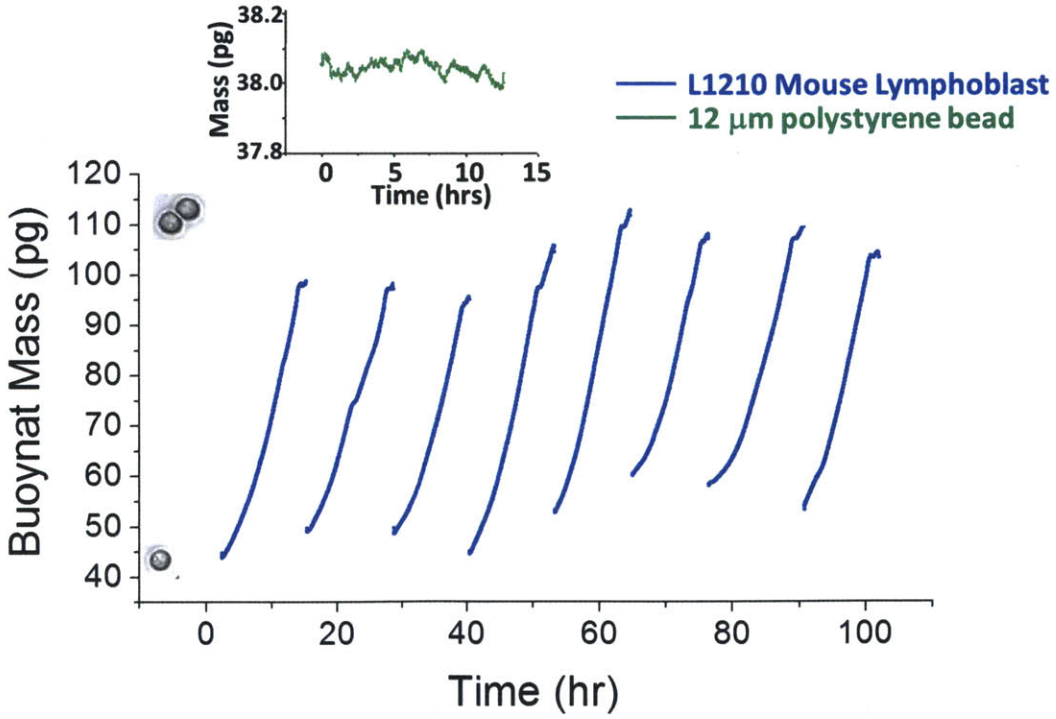

Figure 2-4: Lineage growth trajectories of L1210 cells. Inset) buoyant mass measurement of 12 μm polystyrene bead for 12 hours.

stress to the cell (see chapter 2.3) and pH fluctuation in the bypass channels (see chapter 2.4). Conventional time-lapse assays based on the culture of cell population suffer from constant change of the media condition due to the depletion of nutrient and addition of the molecules secreted from cells. The unique 'media-clamp' allowed by the new dynamic trapping scheme provides the true steady-state environment for cells and has a potential to provide the new culture system when implemented with high-throughput (see chapter 4).

To validate the capability of the system that cultures a single cell long-term, we sought to measure the growth of a well-studied mouse lymphatic leukemia (L210). Fig 2-4 shows the growth of a lineage of L1210 for 8 generations. Mass measurement error was characterized by beads or fixed cells and showed an estimation error of 0.05% when smoothened with 30mins moving average filter. As expected a cell doubled the mass and divided to two daughter cells. Upon division, the feedback algorithm of the dynamic trap automatically kept one cell for further trapping and flushed the other to the downstream direction.

We repeated this measurement up to 120 trajectories and the running time of 1000hrs. Fig 2-5 shows the growth trajectories compiled in a density map. For the analysis, we excluded the cells that did not grow well based on the two criteria: i.) obvious cell death characterized by rapid loss of mass (Fig 2-6), primarily due to imperfect system rinsing, contaminated or unstable culture. ii.) Odd features in growth trajectories such as very asymmetric division, insufficient growth, or extremely long cell cycle. The latter criterion is less clear and it is possible that we lost some of the natural growth phenotype that existed in the culture. To clearly confirm this, we would need an independent measurement of single cell interdivision time variability, division asymmetry, and the degree of proportional growth in one cycle but these extend beyond the scope of this study. Nevertheless, these outliers are likely to arise from the different growth programming and it is reasonable to analyze them separately when studying the steady-state growth of cells. For the ones selected for the analysis, we confirm that the average interdivision time agrees well to the doubling time of bulk culture (Fig 2-7).

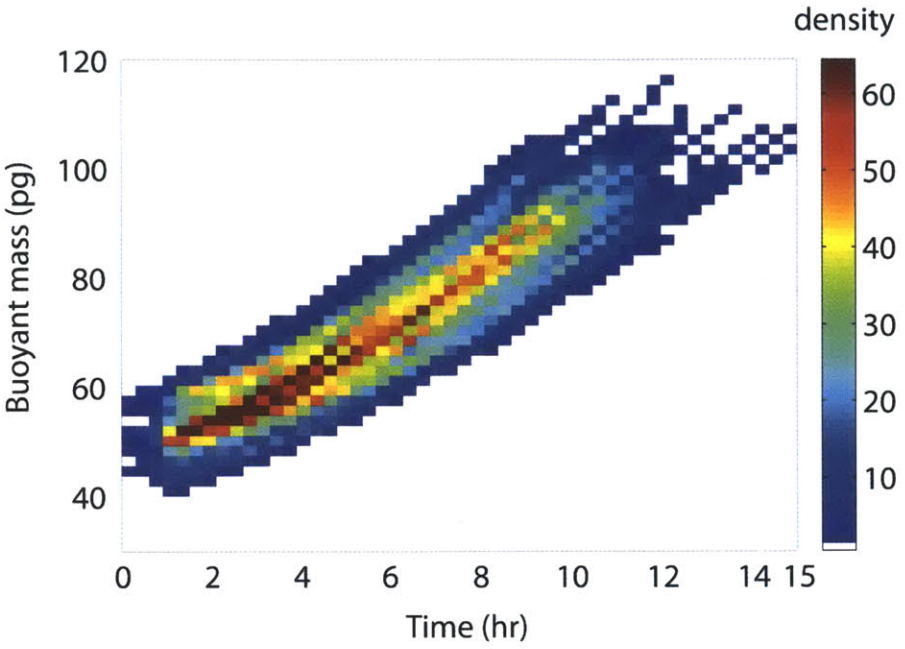

Figure 2-5: Accumulated growth trajectories of L1210 single cells. 122 growth curves are overlaid and the density is shown for each pixel in the color map.

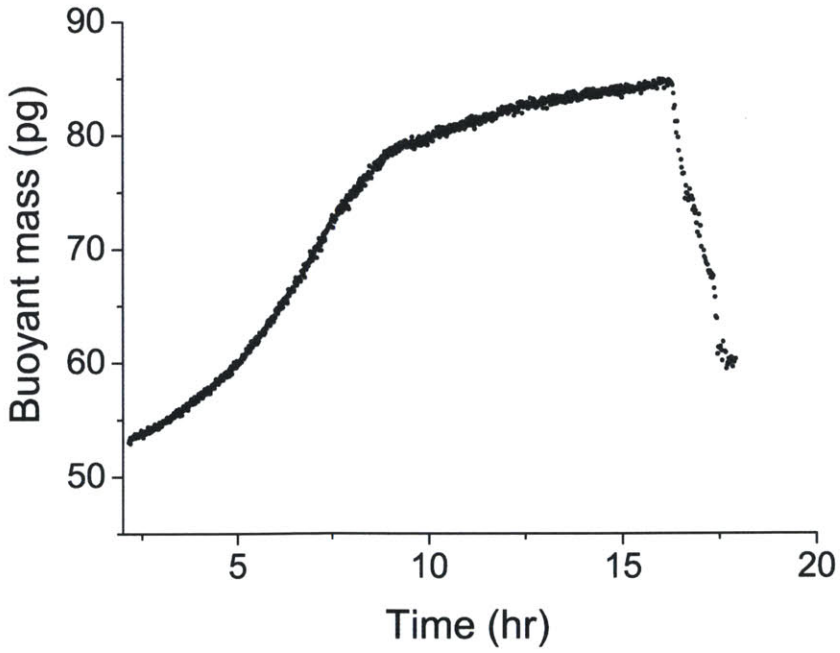

Figure 2-6: Rapid loss of mass. A cell suddenly loses its mass after the long period of attenuated growth.

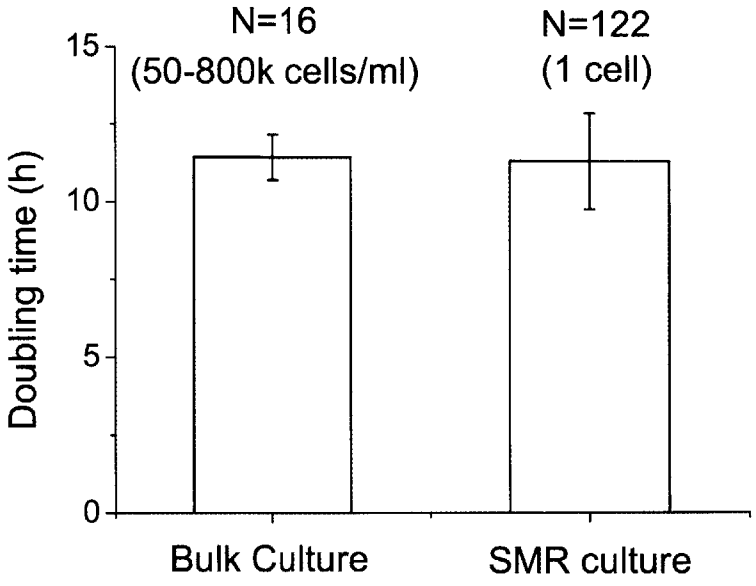

Figure 2-7: Interdivision time of the cells grown in the SMR agrees to the doubling time of the bulk culture. For bulk doubling time of the culture, cell proliferation during 48hrs were measured every 24hrs in 16 independent runs.

2.3 Shear stress

Due to the nature of the SMR that measures cells in flow, the shear stress may impose the detrimental effect on cell growth and it has to be carefully characterized. The degree of accrued stress is related to the frequency and the speed of cell transit through the SMR, which has the inner cross-section (15 by 20 μm^2) comparable to the cell diameter (5 to 15 μm). First, to emulate physiologically relevant conditions, we fixed the speed of cell transit to the order of 10mm/sec, which is equivalent to the average flow rateof leukocytes in microcapillary [27]. We then characterized the growth phenotype based on two different periods of trapping, transit every 10 second or 30 second. Surprisingly, cells exhibited different growth phenotype when exposed to higher shear stress; the trajectory deviated from the pure exponential pattern (Fig 2-8). Interestingly, this subtle but significant growth phenotype change did not result in appreciable change either in size or interdivision time (Fig 2-9), implying that the traditional way of assessing the cell viability based on doubling-

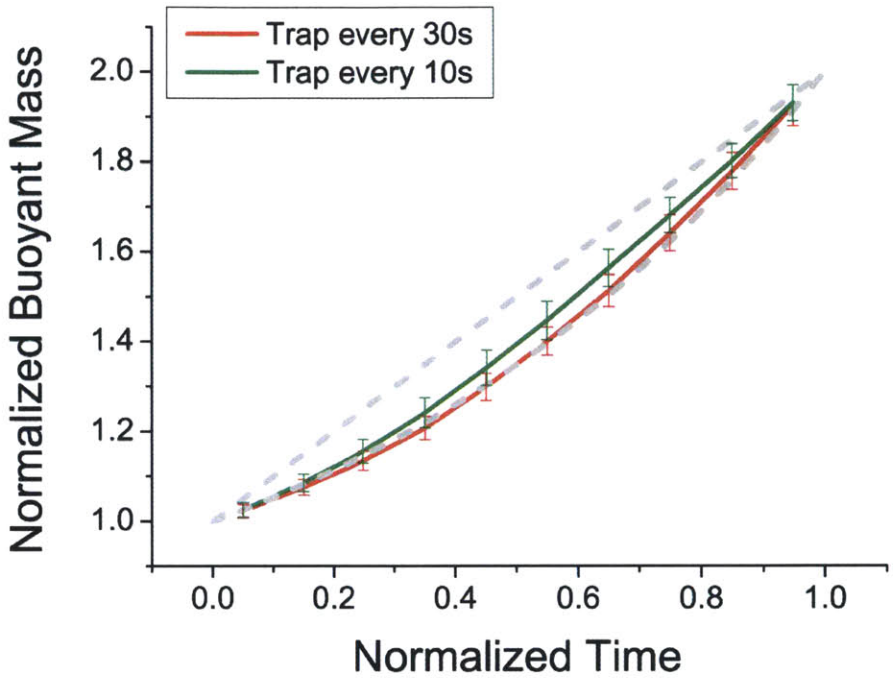

Figure 2-8: The effect of shear stress on cell growth. Red (n=9) and green (n=8) curves show the normalized mean growth trajectories under low and medium shear stress respectively. P-value (two-sample Student's t-test) was calculated in the binned time window and it was smaller than 0.01 for all the bins from time 0.2 to 0.8. Dotted line indicates the pure linear or exponential growth trajectory.

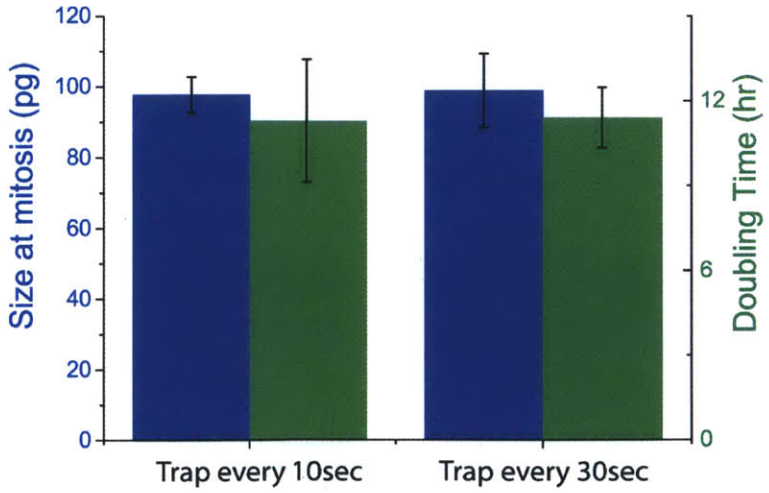

Figure 2-9: The effect of shear stress on bulk growth parameters. P-value from the Student's two-sample t-test gives 0.79 for size, 0.96 for doubling time.

time would provide only limited information. Further increasing the trapping period over 30 seconds did not result in a change in growth phenotype (data not shown). Since more frequent trapping would improve the measurement precision and long-term pH stability as well as media replenishment, we maintained the trapping period of 30 second throughout the study.

2.4 Control of pH

General tissue culture media such as RPMI or DMEM requires certain amount of CO_2 for bicarbonate buffering. In case it is difficult to produce a suitable atmosphere with CO_2, a specialized media formulation, Leibovitz L-15 medium, is designed to eliminate CO_2 through the use of sodium pyruvate and buffering with high amino acid concentrations. However, L-15 provides only partial solution since many cell lines do not adapt well to L-15 medium [28]. To make the SMR applicable to growth study of various cell types we sought to render the system to maintain constant CO_2 level.

To achieve this, the media vials were pressurized with 5% CO_2 gas (Airgas), which stabilized the pH of media in the vial. However, due to the CO_2 leakage in the tubing and the gasket, dissolved CO_2 was lost from the media on the way to the chip and limited cell growth in the bypass channels. PEEK tubing (IDEX), which has minimum gas permeability, was used to reduce CO_2 leakage. Nevertheless, CO_2 leakage still occurred at the tubing-to-chip gasket interface. As a result, on-chip pH monitoring was required for determining the optimal flow conditions and device geometry for maintaining a stable pH. This was accomplished by utilizing the fluorescent indicator BCECF (2′,7′-bis-(2-carboxyethyl)-5-(and-6)-carboxyfluorescein), which is often used for monitoring intracellular pH. The pH sensitivity of BCECF in the SMR-optical system (see chapter 2.6) was calibrated by using a plate reader (Tecan) (Fig A-1). Real-time monitoring in the bypass reservoir revealed that the pH would increase within 1-2 hours if the media was not replenished with sufficient frequency (Fig 2-10) and it resulted in gradual cell death.

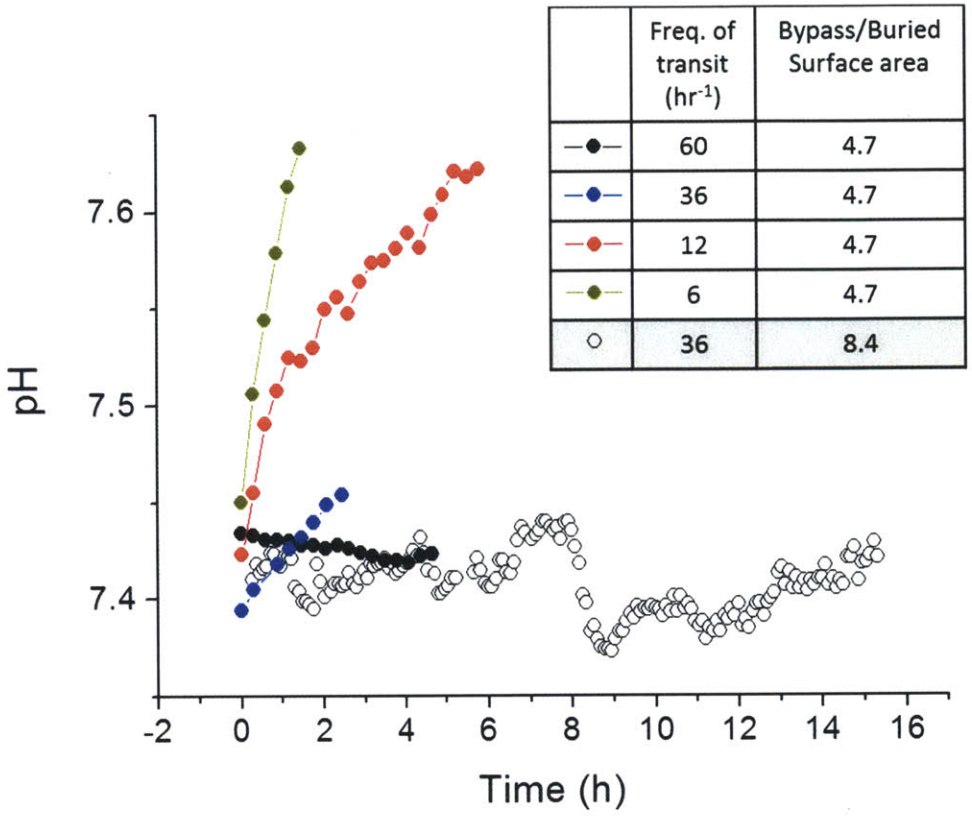

Figure 2-10: pH stability in the bypass reservoir. The pH in the bypass reservoir was measured over time for four cell transit conditions and two SMR chip designs (see Table). Transit conditions were determined by how frequently the cell transited through the SMR, which together with the bypass-to-buried surface area ratio, determined the media replenishment rate in the chip. pH in the chip slowly increased when the replenishment rate was too low due to the local leakage of CO2 that occurs in the tubing-to-chip gasket interface. For the design with the low bypass-to-buried-surface-area ratio, it was necessary to transit the cell every minute in order to maintain constant pH (black filled circles). However, for FL5.12 cells, this level of shear stress was detrimental. By using a SMR chip with a larger bypass-to-buried-surface-area ratio, the pH was stably maintained over extended periods of time with a low transit frequency (black open circles).

Since the media replenishment rate is governed by the cell transit frequency, achieving stable pH came at the cost of exposing the cell to detrimentally high levels of shear (Fig A-2). To overcome this, the new SMR chip was designed with enlarged bypass reservoirs (cross-sectional dimensions were increased by two-fold from 1400 μm^2 to 2800 μm^2), which enabled the replenishment rate to be increased by five-fold for the same transit frequency. As a result, a stable pH was observed for more than 15 hours when the cell transited the SMR as infrequently as once every 100 sec (Fig 2-10).

We measured the growth of FL5.12, mouse pro-B-cell lymphoid cell supplemented with RPMI media. FL5.12 is a widely used model system for metabolism or signaling study [29]. To grow single FL5.12 in the SMR, a specific growth factor IL-3 and 10% condition media were added. Fig 2-11 shows the growth of FL5.12 over multiple generations (Fig 2-11).

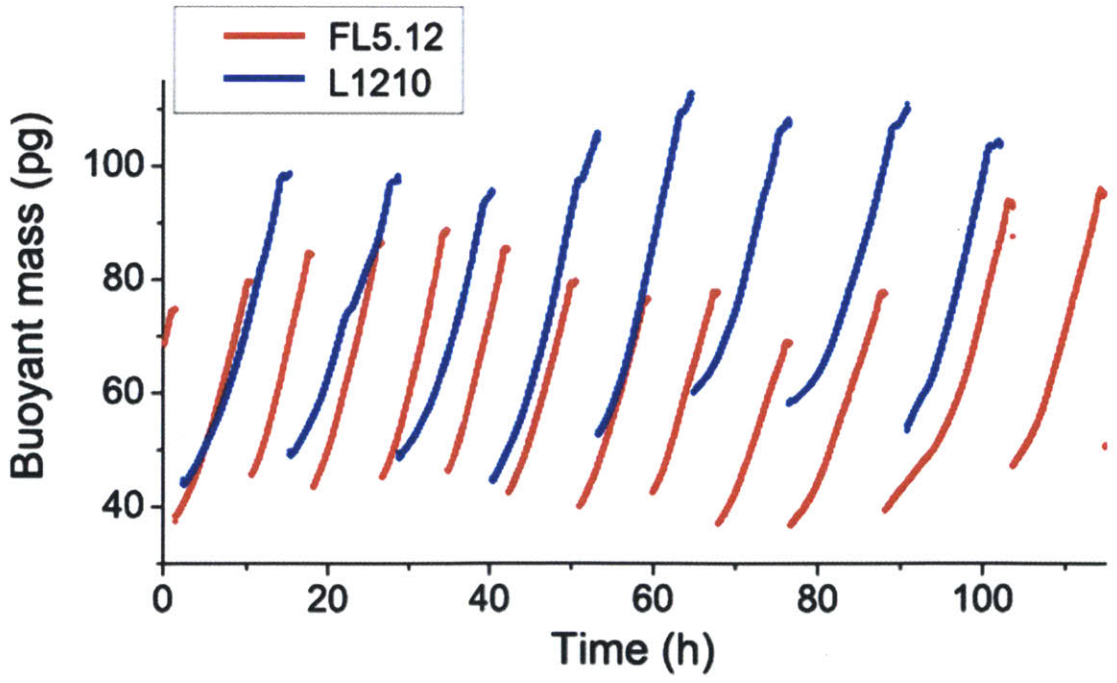

Figure 2-11: Lineage growth trajectories of L1210 and FL5.12 cells.

2.5 Improving measurement precision

When a particle flows through the resonator's microchannel, the resonance frequency shift is position-dependent, with the maximum frequency shift occurring when the particle is at the SMR tip. Since the microchannel width is designed to accommodate a range of particle sizes and reduce clogging, the particle flow path near the tip of the SMR is uncertain and reduces the precision of the mass measurement (Fig 2-12). Even though the SMR has the potential to weigh a particle with a precision near 0.01%, this limits the actual precision to the order of 1%. Even though this can be further reduced by smoothing the data, it comes at the cost of losing the information that varies rapidly such as rapid-loss-of-mass or immediate drug response. Yet another approach in data processing is to use the peak shape as a determinant of cell transit path and compensate for it when calculating mass (Fig A-3). Here we introduce two independent methods to address position-dependent error.

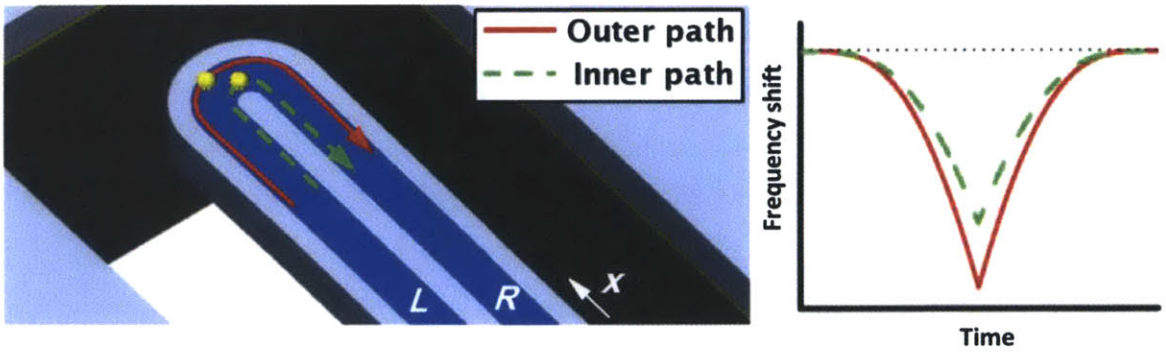

Figure 2-12: Schematic of the position-dependent error. A particle in the SMR may transit anywhere between the inner and outer channel wall. A particle that makes a U-turn near the inner wall (dashed green line) causes a smaller frequency shift than if it turns near the outer wall (solid red line). (Figure adapted from Lee *et. al.* [30])

First, a unique form of hydrodynamic focusing can be used to confine the flow path of the cell as it travels through the SMR (Fig 2-13). To achieve this, we balanced the pressure along the bypass and flow entered the SMR from the top and bottom sides and the particle's path was focused. When smoothened with 30 minutes moving average, this enabled the cell's buoyant mass and growth rate to be

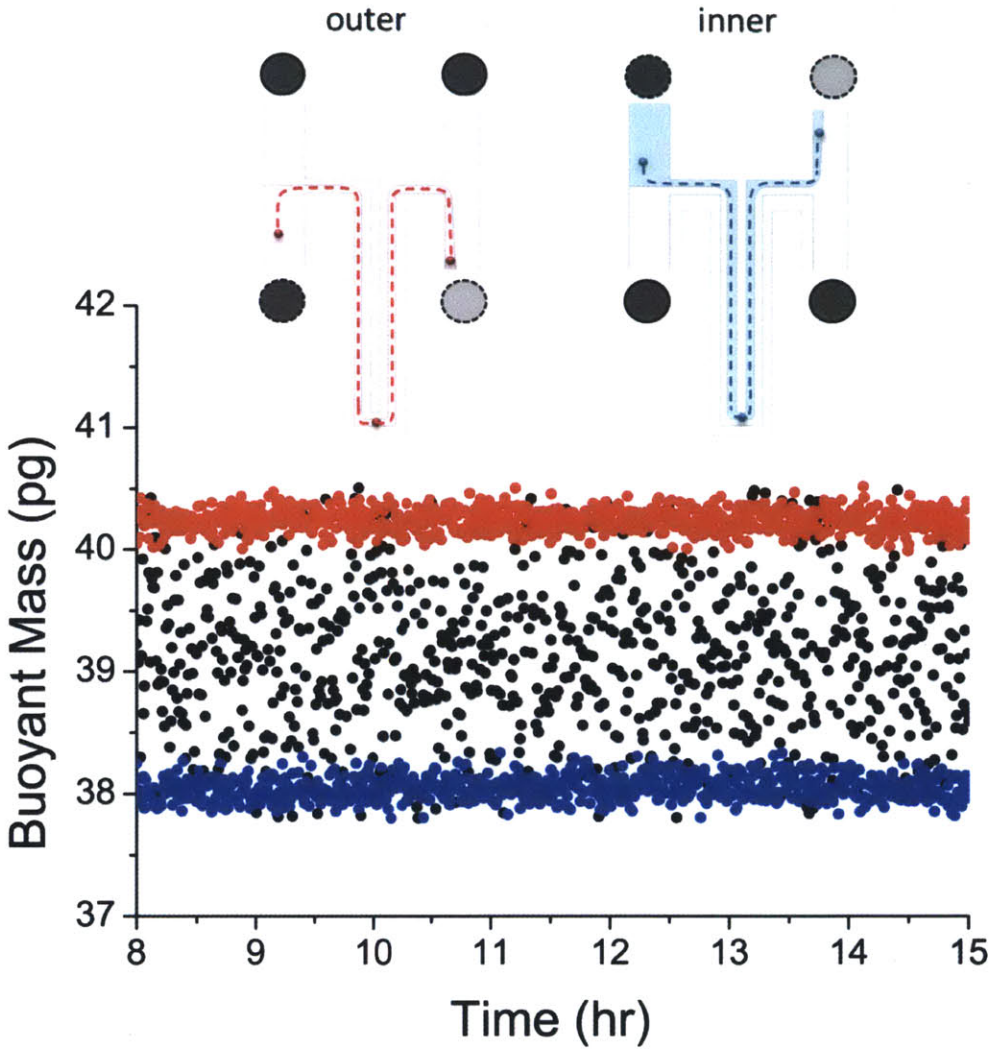

Figure 2-13: Hydrodynamic focusing constrains the flow path of a cell that transits the SMR. The cartoon shows the pressure configurations in the four ports: high pressure (dark grey) and low pressure (light grey). Solid black lines indicate a fixed pressure and dashed black lines indicate an alternating pressure. If a pressure gradient exists along the bypass channel, then particles that enter the SMR will travel through it with a highly variable flow path. This is evident when the resonant frequency shift from a 12 μm polystyrene bead is repetitively measured (black points on plot). By balancing the pressure along the bypass, flow enters the SMR from the top and bottom sides and the particle's path is focused. The dashed red line in the cartoon indicates focusing through the outer flow path (red points on plot) and the dashed blue line indicates focusing through the inner flow path (blue points on plot).

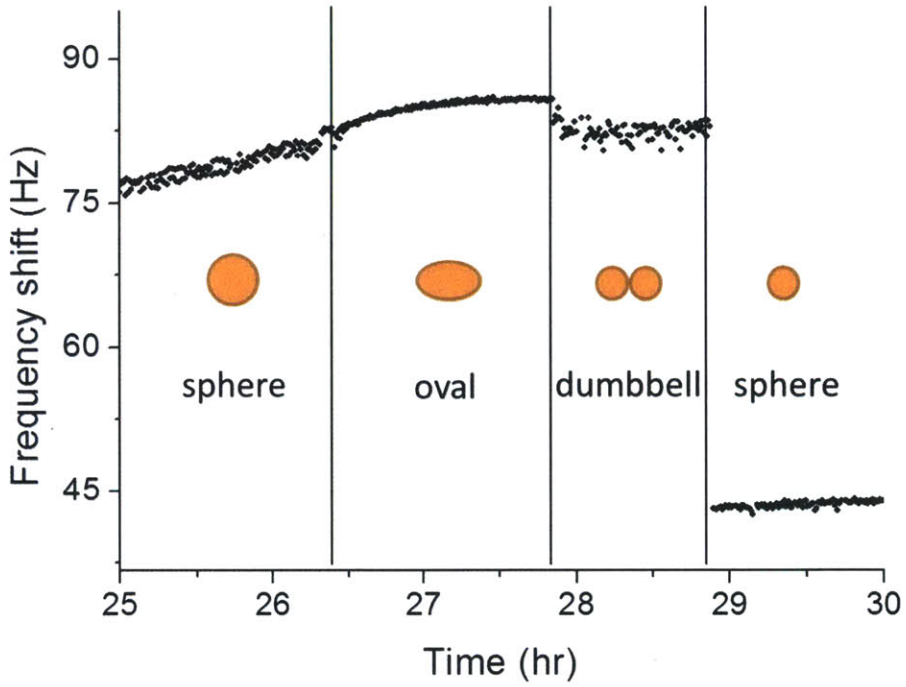

Figure 2-14: Frequency shift during cytokinesis. The quality of measurement varies depending on the geometry of the cell, which is shown schematically.

measured with an error near 0.05% and 3% in standard deviation, respectively, which represents a ten–fold improvement. Even though this effectively works with the spherical white blood cells, however, the shape of the cell could affect the quality of focusing. For example, cells became unfocused and measurement error temporally increased as the cell went through cytokinesis (Fig 2-14). More fundamental solution was necessary to improve the measurement precision for various cell types that have non-spherical geometry.

Second, the second vibration mode was deployed to fundamentally remove the position dependent error [30]. Briefly, the relative resonance frequency shift of a cantilever with added mass Δm is estimated by

$$\left(\frac{\Delta f}{f}\right)_n = -1 + \left[1 + u_n \left(\frac{x}{l}\right)^2 \cdot \frac{\Delta m}{m_{eff}}\right]^{-0.5}$$

where $u_n\left(\frac{x}{l}\right)$ is displacement at a position normalized by the cantilever length, l is the cantilever length, f is the resonance frequency, and m_{eff} is the effective mass of the unloaded cantilever. The second mode exhibits an antinode, which corresponds to local maximum displacements and generates local maximum frequency shifts when a minuscule mass is added on the cantilever (Fig 2-15). Since the frequency shifts measured at the antinode are nearly insensitive to the lateral position of the particle, there is no position-dependent error and mass sensing at the antinode is mostly limited by the system frequency resolution.

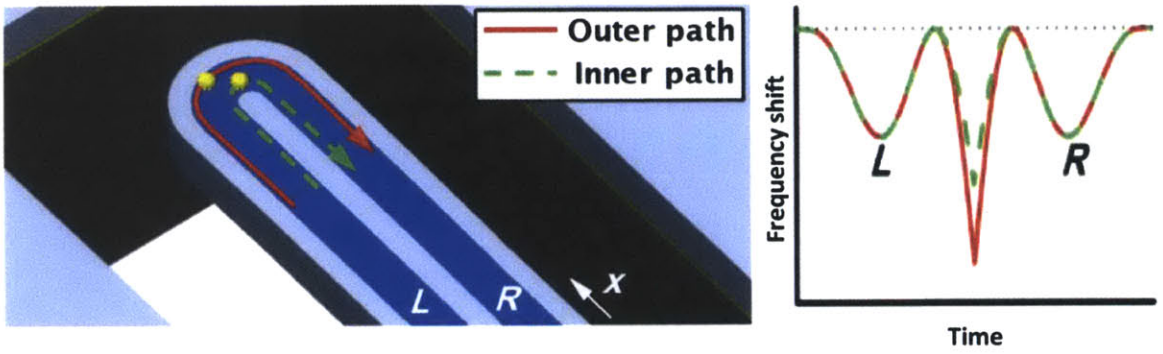

Figure 2-15: Resonance frequency shifts of the second flexural bending mode upon point mass transit through a cantilever. There are three peaks in the frequency shift (one at the free end and two at the antinode). Letters "L" and "R" indicate left and right hand side of the microchannel in which the corresponding antinode peaks occur. (Figure adapted from Lee et. al. [30])

Achieving second vibration mode often requires strong actuation of the cantilever and sensitive detection of the bending since the amplitude of vibration decreases in the higher mode due to the increased effective stiffness [31]. The LSMR is particularly stiff comparing to the normal SMR due to the large height to length ratio and it results in attenuated second mode vibration. To overcome this and operate the system in the second vibration mode, we amplified the cantilever actuation by replacing the electrostatic actuation to the mechanical actuation using a piezocrystal of the dimension 2mm × 2mm x 2mm (PL022.31, Physik Instrument). Previously, it was demonstrated that this mechanical actuation could amplify the deflection of cantilever by 5-folds comparing to the electrostatic actuation [32].

Since the impedance of the piezocrystal can be very small depending on the actuation frequency, we further stabilized the operation by using an op-amp that supports high output current (LT1206, Linear Technology). Qualitative measurement of the deflection amplitude showed about 10-folds increase and it was indispensable to operate the system in closed-loop operation. Finally we added a band-pass filter to effectively filter out otherwise dominant first mode signal and operate the system in closed-loop.

With the second vibrational mode operation, the point mass measurement error was reduced from 1.5% to 0.05%, or 10fg minimum detectable error (Fig 2-16), which represents a 6–folds improvement even comparing to the hydrodynamic focusing. In a biological unit, this accounts to about 9 million base pairs of DNA (0.3% of total genome), 1 million average sized proteins (0.02% of total cellular protein), or 30 million molecules of glucose [33].

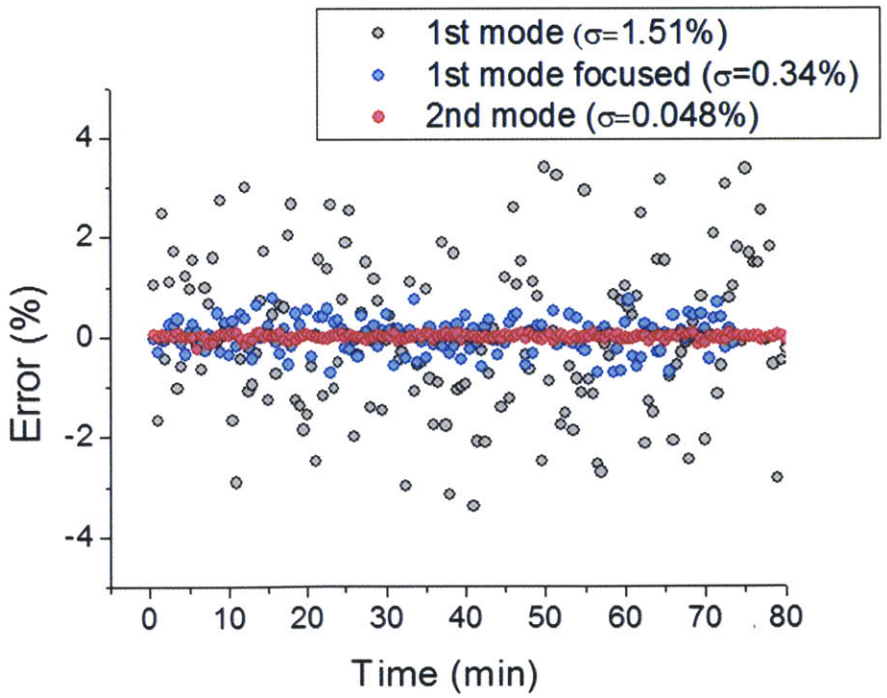

Figure 2-16: Measurement precision of the first and second bending mode. In each condition, fixed L1210 cells of similar size was trapped for about an hour and the percent error was found by normalizing the data with the average mass.

2.6 In-situ imaging

The development of fluorescent-based molecular probe is ever increasing and allows us to determine the biological activity of live or fixed cells in different levels: transcription, translation, phosphorylation, or methylation, and so on. Considering the critical role of imaging in elucidating the molecular mechanism of biological systems, we sought to integrate the imaging modality with the SMR to be able to correlate the unique mass information to the molecular information.

A modular microscope (Nikon) was mounted on top of SMR and a 50x objective lens (Nikon- CFI Plan BD ELWD N.A 0.55, W.D 9.8mm) was used to collect the fluorescent signal into two separate photomultiplier tubes (H5784-02) (Fig 2-17). To measure red and green fluorescence simultaneously, wideband metal halide illumination (Lumen-200pro) was used with a dual-cavity dichroic mirror (Chroma-59004) and single cavity emission filters (red-ET585/40m, green-HQ520/20m both Chroma). Two field-stops were used to confine the area of illumination and imaging to minimize the background noise. Fluorescent signals were measured at the collimated plane. For data acquisition, analog low-pass filter with the cutoff frequency of 100 Hz is used.

First, we confirmed that the PMT is operated in the shot-noise limited regime and not interfered by dark current or Johnson noise. As shown in Fig 2-18, the noise increased linearly proportional to the square root of the signal from 0.01V to 0.5V, an indication of shot-noise limited system. Below 0.01V was interfered by dark current, above 0.5V was saturated. Second, we tested the sensitivity of the system by using MESF-FITC standard (Bangs lab). Right before the particle enters the SMR, fluorescent signal was measured in the optical window placed in the bypass channel. Among the five different groups of fluorescent intensity beads, two dim ones (MESF=2.5k, 19k) could not be resolved and three bright ones (MESF=75k, 252k, 737k) were measured as shown in Fig 2-19. It shows the sensitivity of 5.8×10^{-7}V/MESF. The limit of detection was about 10,000 MESF at 10 Hz bandwidth, which is ten-folds worse than the commercial flow cytometry system that can measure down to 1,000 MESF at 100 kHz bandwidth. Third, we tested the precision of the

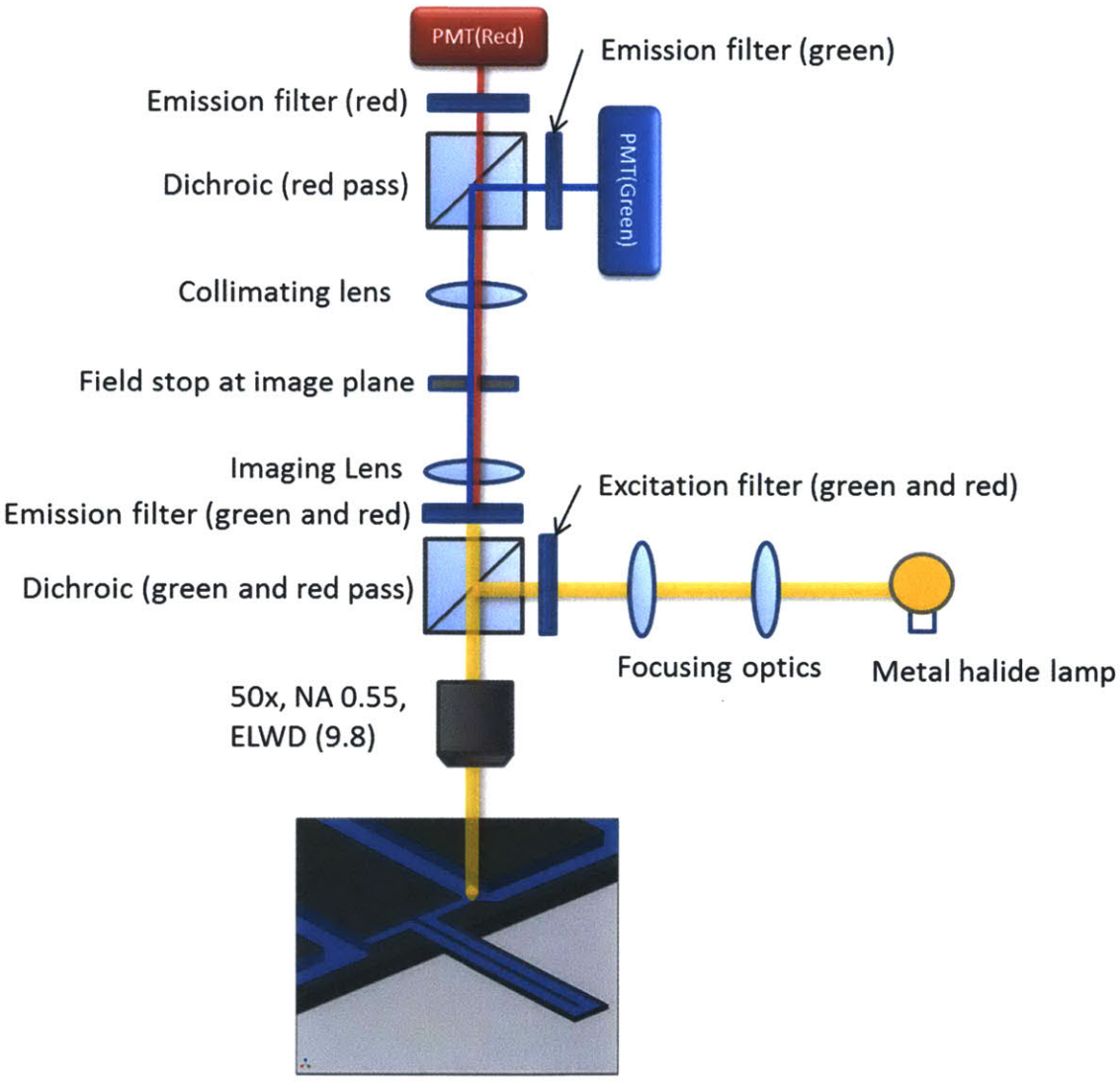

Figure 2-17: SMR-optical system for single cell fluorescence measurement.

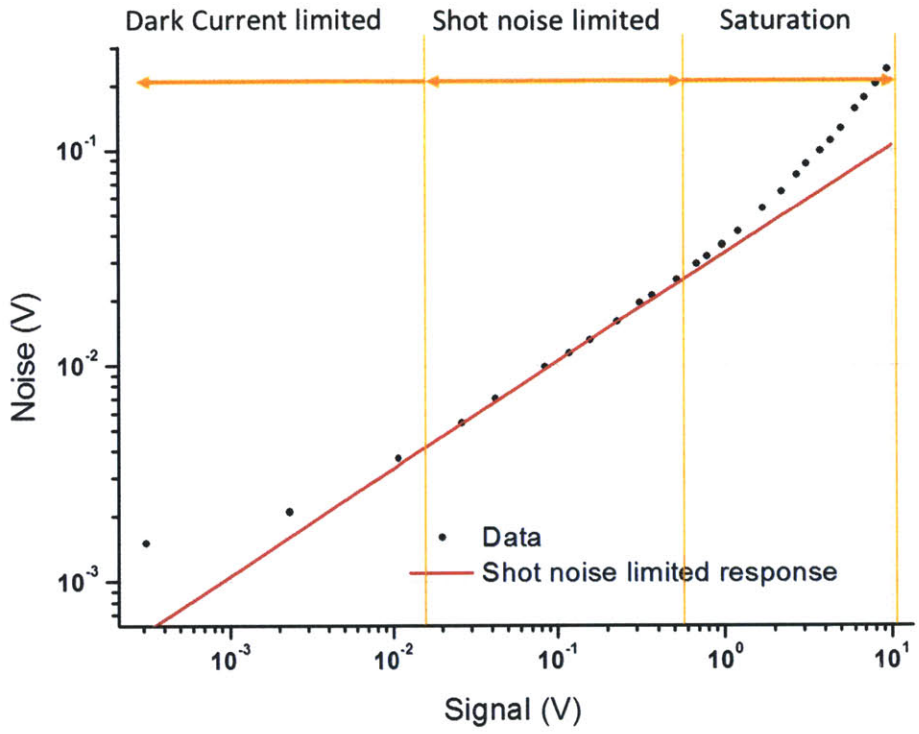

Figure 2-18: Validation of the shot-noise limited system. Red line indicates the shot noise limited response. The plot is in log-log.

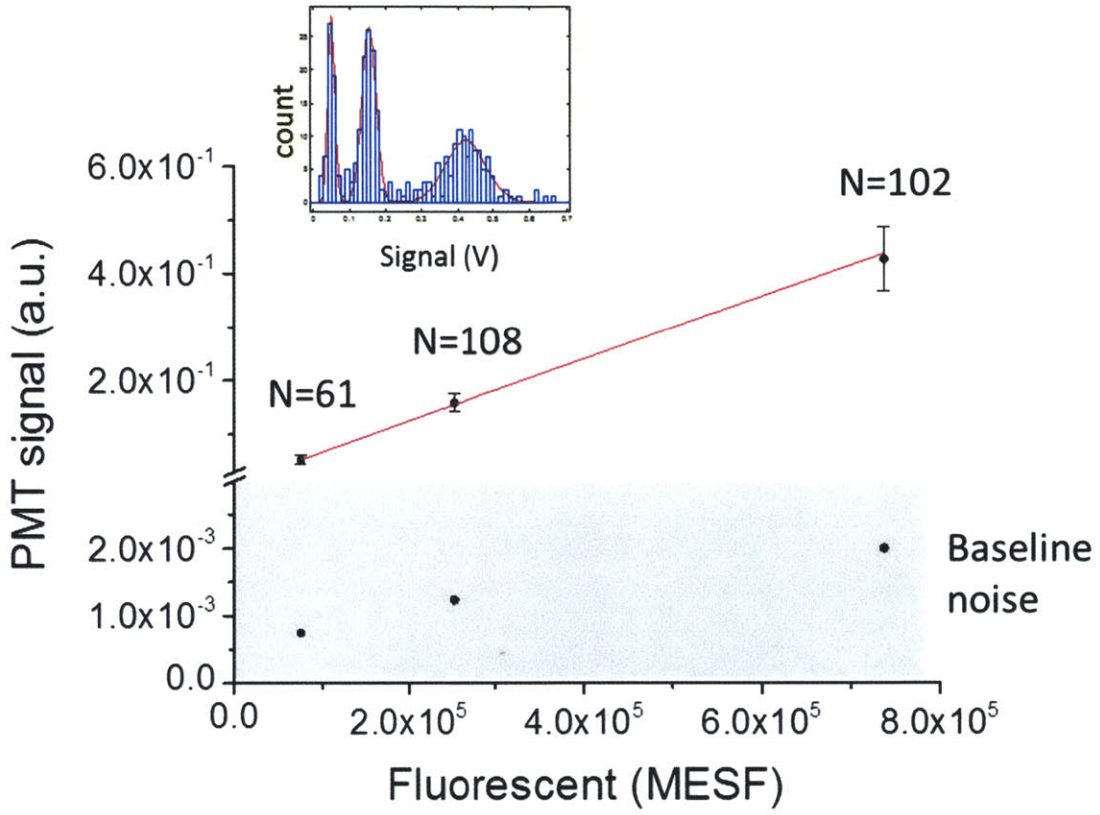

Figure 2-19: Sensitivity of the SMR optical system. Mean and standard deviation of the fluorescent signals from three different populations of MESF standard beads. Inset shows the histogram of the MESF standard mixture and the Gaussian fit (red curve). Linear fit (red, $r^2 = 0.998$) on the main plot shows the sensitivity of 5.8×10^{-7}/MESF. The corresponding baseline noise for three different signals are shown at the bottom of the plot (one sigma, acquired at 10Hz bandwidth). The signal-to-noise ratio is 70, 130, and 210, for the n = 61, 108, and 102 measurements, respectively.

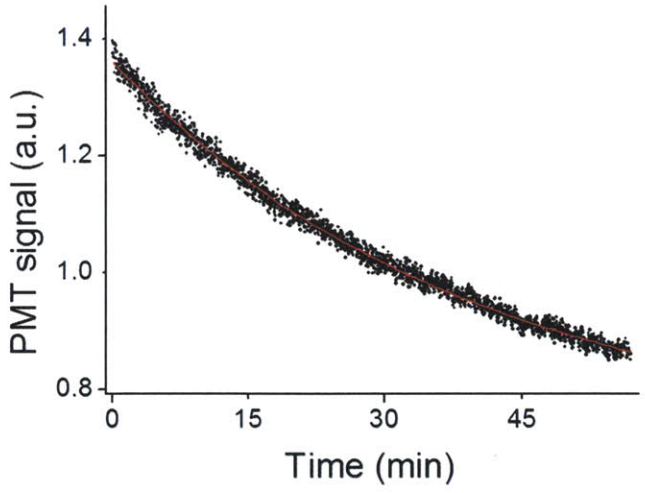

Figure 2-20: Precision of the SMR optical system. The fluorescent signal of the same bead was repeatedly measured every 3 seconds for ~1hr. The signal exponentially decays due to photo-bleaching. The RMSE is 1%.

measurement by trapping the same bead and repeatedly measuring the fluorescent intensity (Fig 2-20). The signal exponentially decayed due to the photo-bleaching and the RMSE was 1%.

This system was deployed to monitor cell cycle events using fluorescent ubiquitination-based cell cycle indicators (FUCCI) [34]. In the experiments reported here the L1210 mouse lymphoblast cells stably expressed fluorescently tagged proteins that are only present during early to late G1 phase of the cell cycle (Cdt1–mKO2, red fluorescence) or during late–G1/S/G2/M phases (Geminin– mAG, green fluorescence). As expected, varying intensity of red and green fluorescent peaks were observed along with the mass signal (Fig 2-21). Red, yellow, and green cells were selected based on the relative intensity of red and green signal and the size distribution of the sub-population was plotted (Fig 2-22). The portion of cells in each phase was proportional to the known length of each phase in cell cycle.

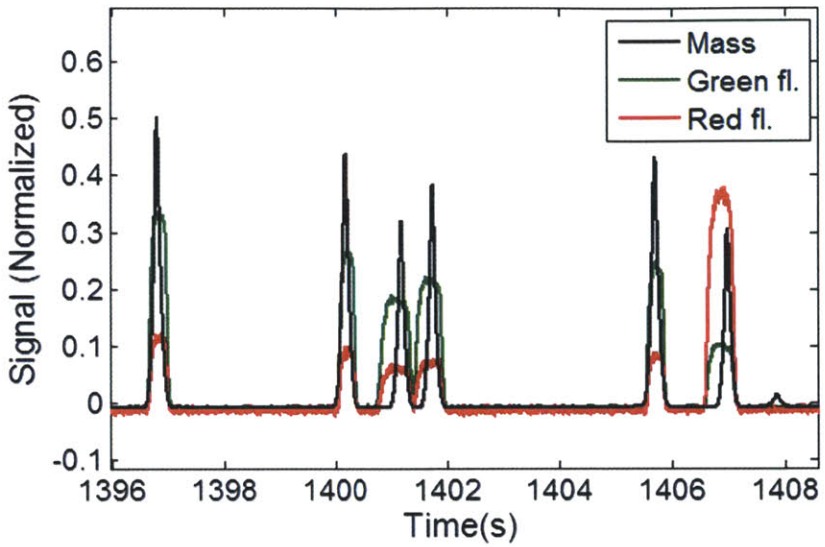

Figure 2-21: Mass (black) and fluorescent (green and red) of the L1210 cell population. Each signal was normalized by the maximum value.

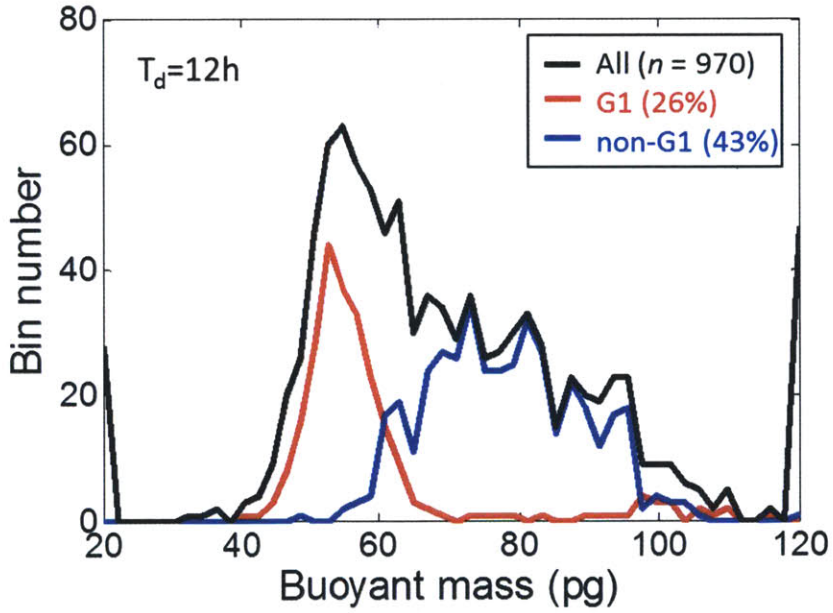

Figure 2-22: Size distributions of steady-state cell cultures. G1 (red) or post G1 (blue) cells are measured from a steady-state cell culture. Black line indicates entire population.

Chapter 3

Principles in cell growth

3.1 Growth rate threshold

The advanced SMR/imaging system (Fig 3-1) was deployed to measure the single cell growth and cell cycle progression (Fig 3-2). Measurements of single cell growth with unprecedented precision identified previously undescribed aspects of the growth trajectory. Most striking is the transition in growth rate that occurs mid–way through the cell cycle. During the first several hours after cytokinesis there is a rapid increase in growth rate, followed by a period where the growth rate increases more slowly (Fig 3-3), a behavior consistent with the prior population measurements on these cells [12]. Out of 122 cells measured, 50% showed a distinct change in growth rate transition, 20% showed a less distinct change in growth rate, while the remainder showed erratic growth trajectories (Fig 3-4). We wondered if the growth rate transition might coincide with the transition of cells out of G1 phase – which is thought to be devoted largely to growth – and into S–phase – where DNA synthesis occurs. The FUCCI signals were measured over the complete cell–cycle in 40 cells, of which 20 showed an obvious growth rate transition. There was a strong correlation between the growth rate transition and entry into S phase (Fig 3-3).

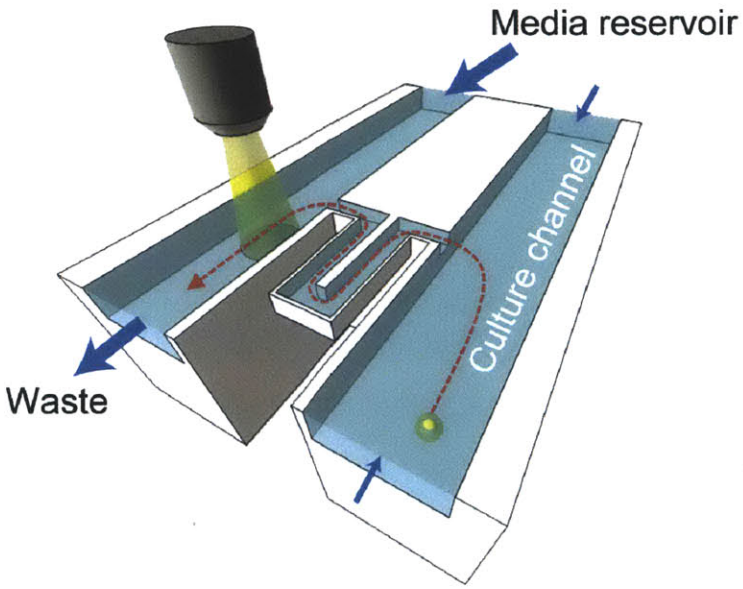

Figure 3-1: Measurement of single cell growth and cell cycle progression. (a) Pressure-driven flow (blue arrows) moves a cell between bypass channels and provides fresh media between measurements. The cell is weighed as it passes through the SMR (red path). Fluorescent signals are measured when the cell passes through the optical window in the bypass reservoir (yellow).

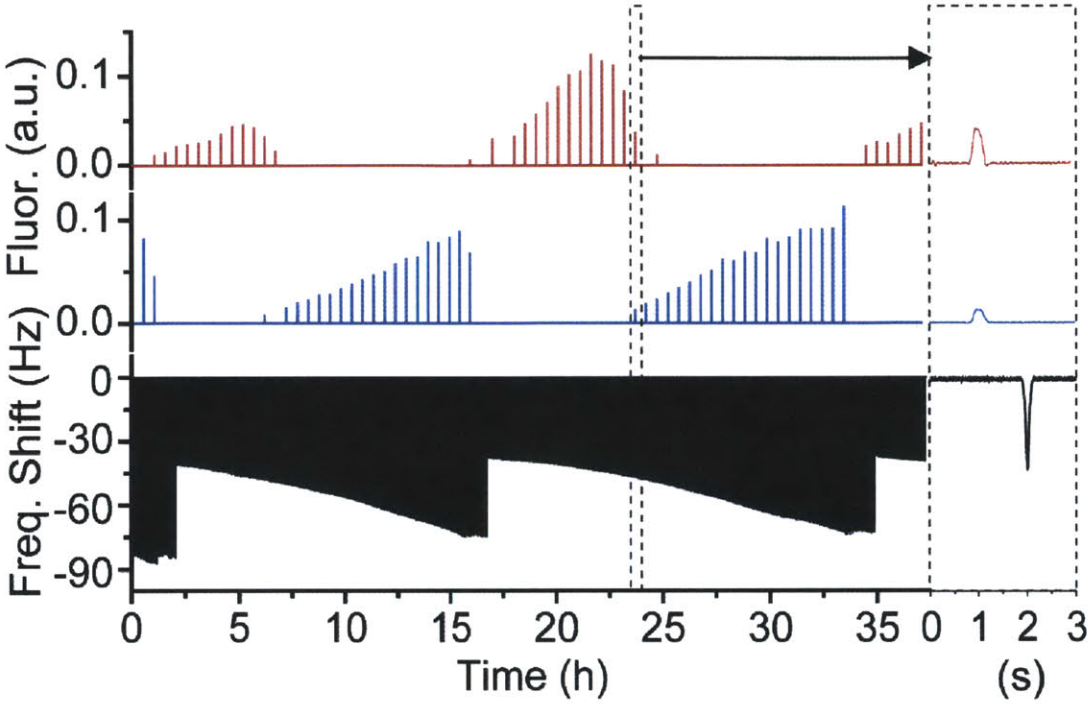

Figure 3-2: Mass (black, measured every 30 seconds) and fluorescent signals from the cell cycle reporters (blue–cdt1 and red–geminim, measured every 30 minutes) were acquired from a L1210 mouse lymphoblast cell over four generations. The dashed box at the arrow zooms-in on signals from one transit through the SMR. Automated feedback between the mass signal and pressure regulators is used to transport the cell back-and-forth between the bypass channels. Following division, one daughter triggers the feedback while the other is swept away.

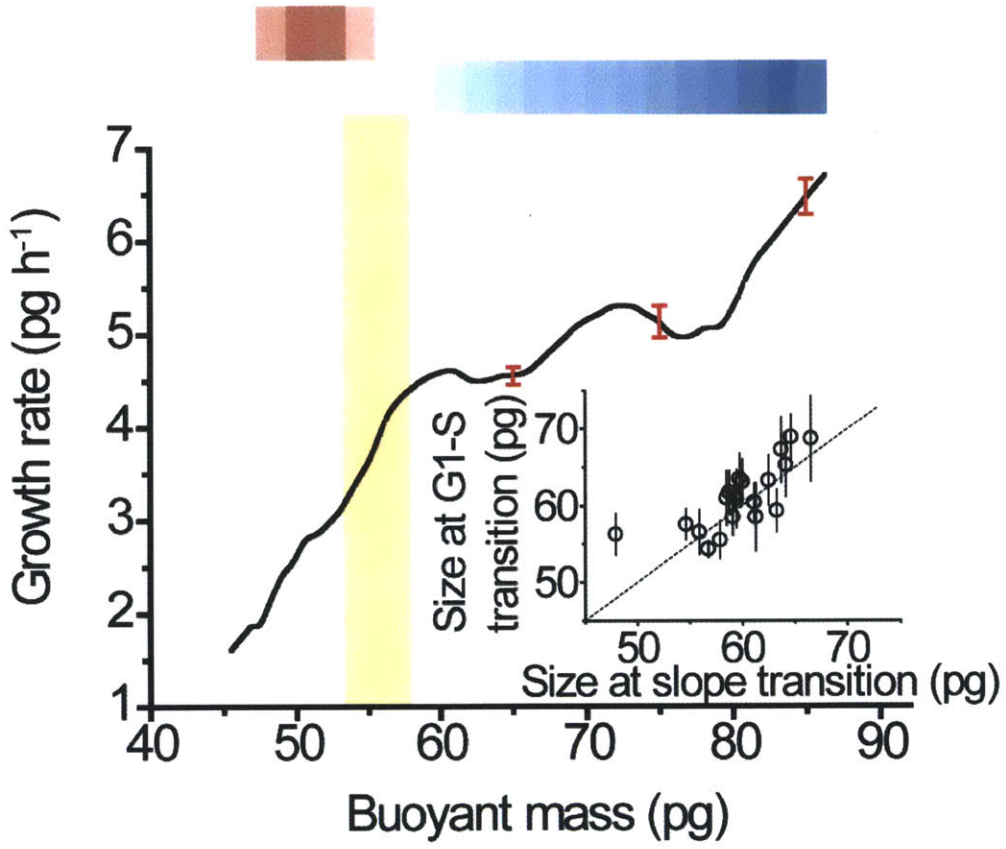

Figure 3-3: Growth rate versus cell mass obtained by measuring buoyant mass versus time of one cell from the newborn stage through division. Color bar indicates relative cdt1 (red, G1 marker) and geminin (blue, S/G2/M marker) levels. Yellow indicates the G1 to S transition. Error bars at various cell sizes are determined by measuring the growth rate of a fixed (non-growing) cell over a 12 hr period and represent one standard deviation from zero growth rate. Inset: Correlation between the size at G1-S transition and size at the growth slope transition (n = 20). Y-error bars indicate the mass change between the maximum and following minimum cdt1 levels.

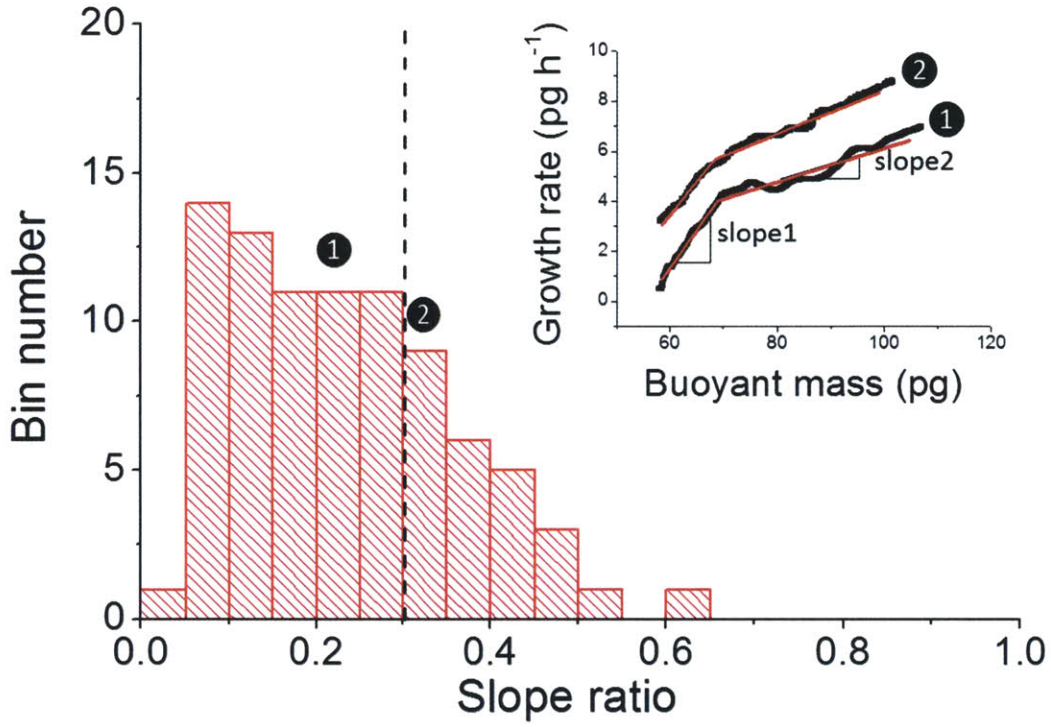

Figure 3-4: Growth rate acceleration ratio at the G1-S transition. Histogram shows the distribution of the slope ratio, which is defined by the growth rate acceleration just after the G1-S transition divided by acceleration just before the G1-S transition. The transition point was determined by a bilinear curve fit (Online Methods). There were 61 cells (out of 122) that exhibited slope ratios below 0.3 and 25 cells with ratios between 0.3 to 0.7. Inset shows two representative trajectories: ❶ slope ratio of 0.22, ❷ slope ratio of 0.34.

A unique benefit of single cell growth trajectories is the ability to register cell–to–cell variability (Fig 3-5). Within each lineage of several cells, there was variability in the instantaneous growth rate of newborn cells that typically ranged from 2 to 4 picograms/hour, and these rates were independent of size. For a given lineage of cells, the variability in growth rate decreases as cells progressed through G1 and begins to increase following the G1/S phase transition. The cell size at this transition point varies between different sets of lineages (Fig 3-6). That newborn cells closely related in lineage have different initial growth rates yet enter S phase with similar growth rates suggests that there is a threshold in growth rate. Even among independent lineages, the coefficient of variance of growth rate at birth decreased to about 60% at the G1/S phase transition (Fig 3-7). We also observe a reduction in size variation between birth and G1/S, although to a much smaller extent (1.7%).

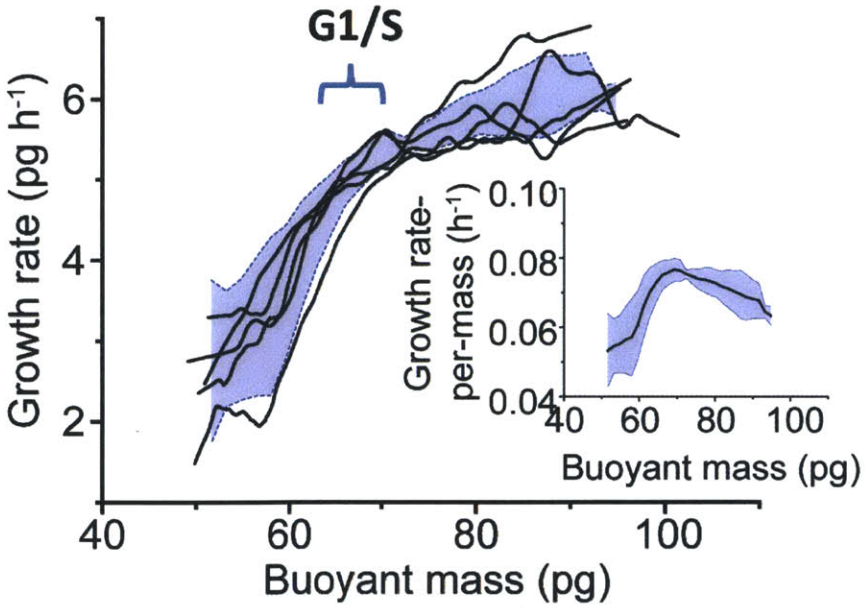

Figure 3-5: Evidence for a growth rate threshold. Single cell growth rate trajectories (black lines) for a lineage of five L1210 cells. Blue area defines five times the coefficient of variance. Inset: mean (black line) and standard deviation (blue area) of growth rate per unit mass from the lineage.

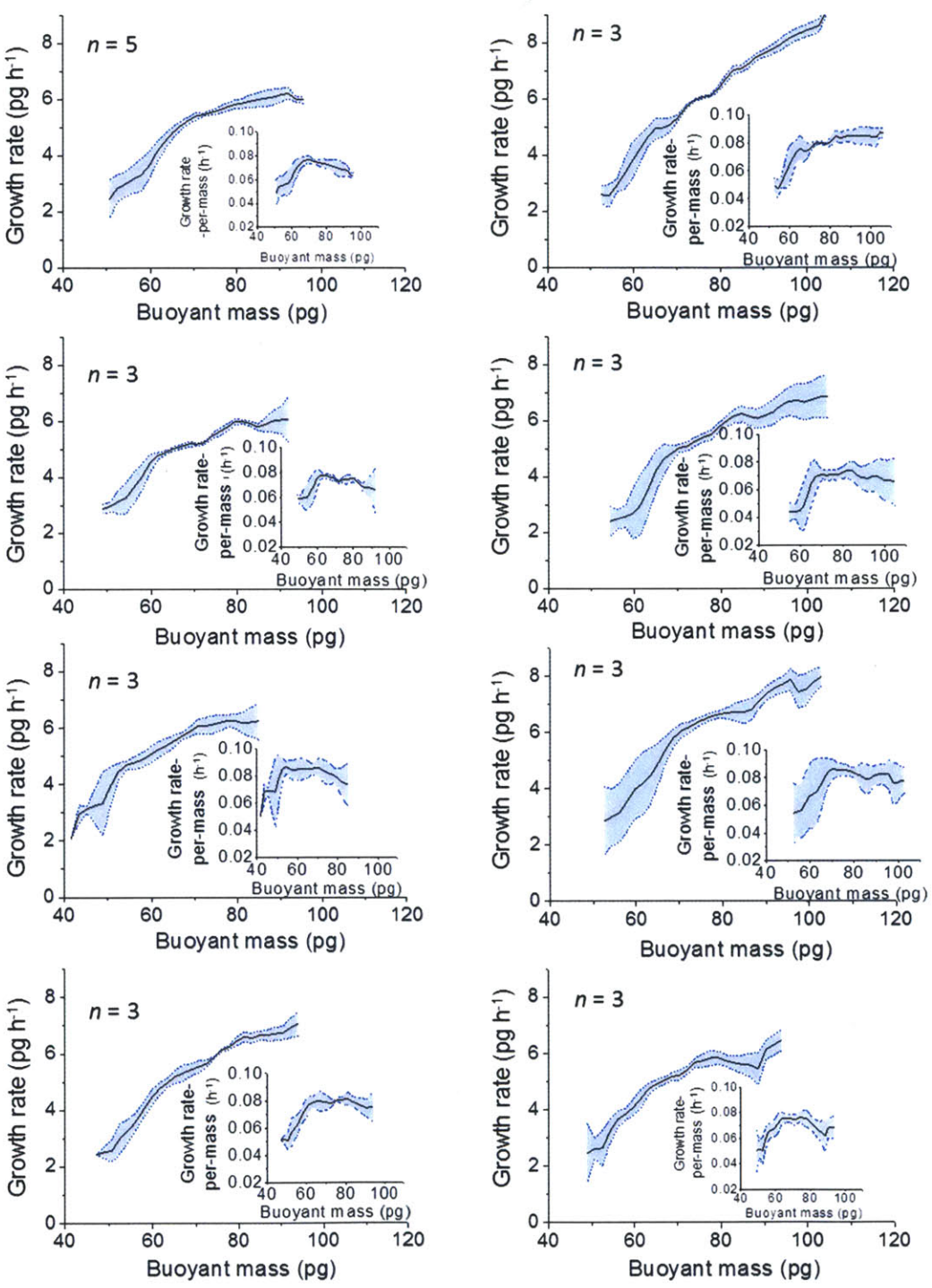

Figure 3-6: Growth rate trajectories of cell lineages. The black lines show the mean growth trajectory from all cells in a particular lineage and the blue shaded region is defined by three times the coefficient of variance. Inset: The mean (black line) and standard deviation (blue area) of the growth rate-per-mass versus mass for the lineage.

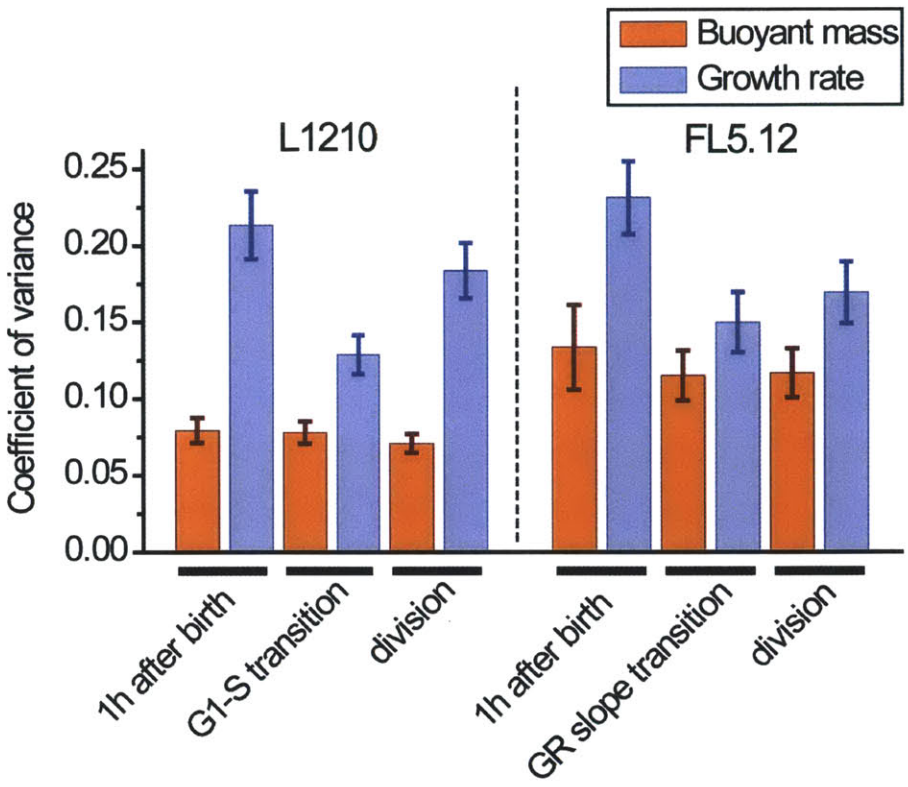

Figure 3-7: Coefficient of variance (CV) for buoyant mass (orange) and growth rate (blue) at various points in the cell cycle. n = 49 for L1210 and n = 28 for FL5.12. Error bars represent one standard deviation of the CV from bootstrapping 1,000 times.

Furthermore, the growth rate dependence on size in G1 increases at a faster than linear rate (i.e. each new unit of biomass that the cell acquires results in more efficient growth than the previous unit). This suggests that there is an active mechanism within the cell for carefully accelerating growth in G1. Considering that ribosome synthesis accounts for more than 50% of total transcription in mammalian cells [35], the active growth modulation is most likely through the regulation of ribosome activity or ribosome biogenesis. This could result from either increased activity of each ribosome or increased concentration of ribosome per unit mass in the cell. Assuming that growth is governed by net ribosome activity, growth rate-per-mass provides an estimate of this 'relative' ribosome activity. The increase of growth rate-per-mass throughout G1 and saturation upon G1/S phase transition

(Fig. 3 inset) suggests that there may exist a critical threshold in the relative ribosome activity before the G1/S phase transition [36].

Further support for a growth rate threshold on entry into S phase, is the strong negative correlation we observed between the duration of G1 and the growth rate in early G1 (Fig 3-8). Since all cells increase their growth rate in G1, slow growing newborn cells may achieve the growth rate threshold by spending more time in G1. This trend became even more pronounced as we decreased the growth rate of cells by limiting nutrients (Fig 3-9). Furthermore, contrary to previous experiments with yeast where small newborns tended to exhibit a prolonged G1 phase [37], we found that neither the duration of G1 nor the interdivision time correlates with newborn cell size (Fig 3-10). This, together with the findings shown in Fig 3-5 and 3-6, suggests that deterministic growth regulation [38] can be based on a critical growth rate rather than a critical size.

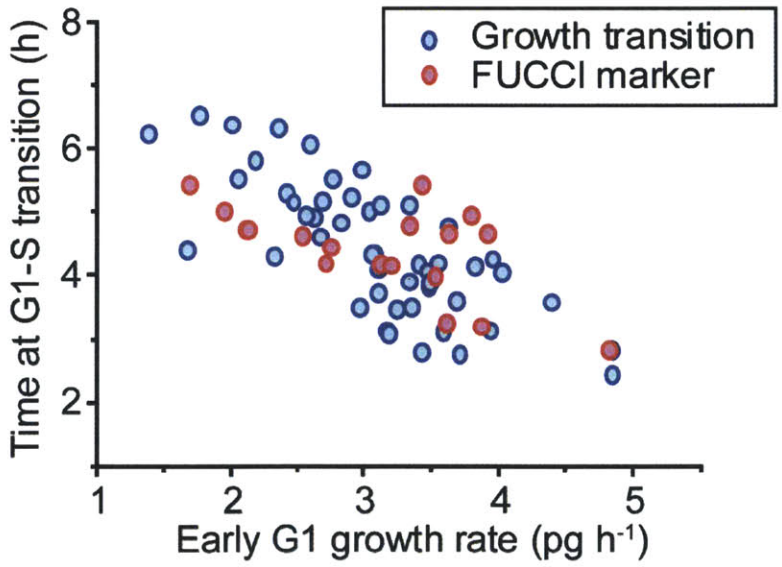

Figure 3-8: Time at G1/S phase transition versus early G1 growth rate (averaged between first and third hour of growth following division) for L1210 cells. Blue circles: G1/S transition defined by growth transition (n = 49, Pearson's correlation coefficient = –0.75). Red circles: G1/S transition defined by FUCCI (n = 18, Pearson's correlation coefficient = –0.60).

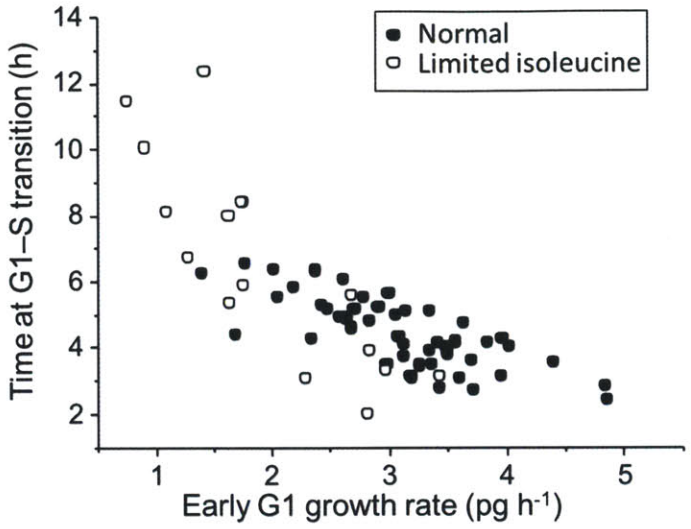

Figure 3-9: G1 duration versus early G1 growth rate in media with limited isoleucine. A negative correlation becomes more apparent when cells are grown under limited isoleucine conditions. Early G1 growth rate is determined by averaging the mass accumulation rate between the first and third hour following cell division. Normal: n = 49, Pearson's correlation coefficient = -0.75; Limited isoleucine: n = 16, Pearson's correlation coefficient = -0.83.

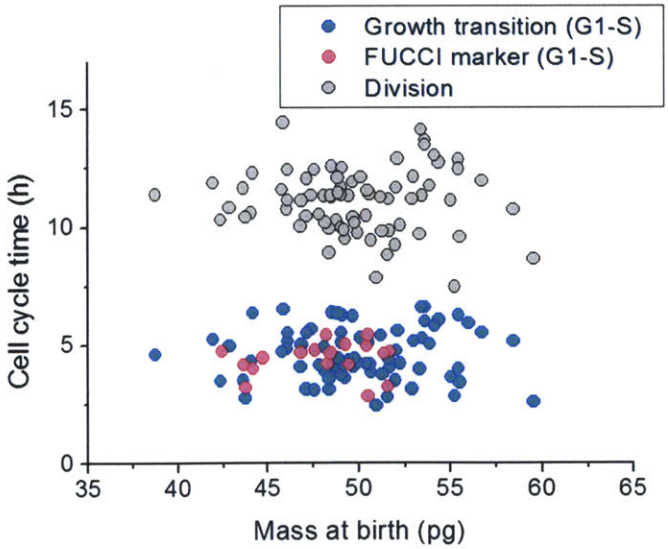

Figure 3-10: Interdivision and G1 time versus newborn cell size. L1210 mouse lymphoblast cells. Blue and red circles: Time at G1–S transition versus mass at birth (blue n = 77, Pearson's correlation coefficient = 0.03, red n = 18, Pearson's correlation coefficient = 0.10). Grey circles: time at division versus mass at birth (n = 122, Pearson's correlation coefficient = 0.08).

Growth phenotypes of FL5.12 cells also support growth rate threshold. Similar to what we observed for L1210 cells, the variability in growth rate for FL5.12 cells decreases as cells progressed through G1 and then begins to increase following the G1/S transition (Fig 3-11). Also consistent with L1210 cells, there is a strong negative correlation between the G1 duration and growth rate in early G1 (Fig 3-12). Unlike L1210 cells, which showed no correlation between the duration of G1 or the interdivision time with newborn cell size, there were measurable but weak correlations in FL5.12 cells (Fig 3-13).

Cell growth and cell size are known to adapt to external conditions. To explore this in more detail, we grew L1210 cells in limiting isoleucine. Under these conditions, the growth rate was reduced and the duration of the G1 phase and interdivision time increased by 1.6–fold (Fig 3-14). Despite this increase, the size range at both the G1/S phase transition and at cytokinesis remained virtually the same as cells in normal medium (Fig 3-15, 16). Furthermore, the presence of a strong negative correlation between the initial growth rate and the length of G1 (Fig 3-9) and a reduction in the variability of the growth rate at the G1/S phase transition (Fig 3-17) suggests that a growth rate threshold is still present.

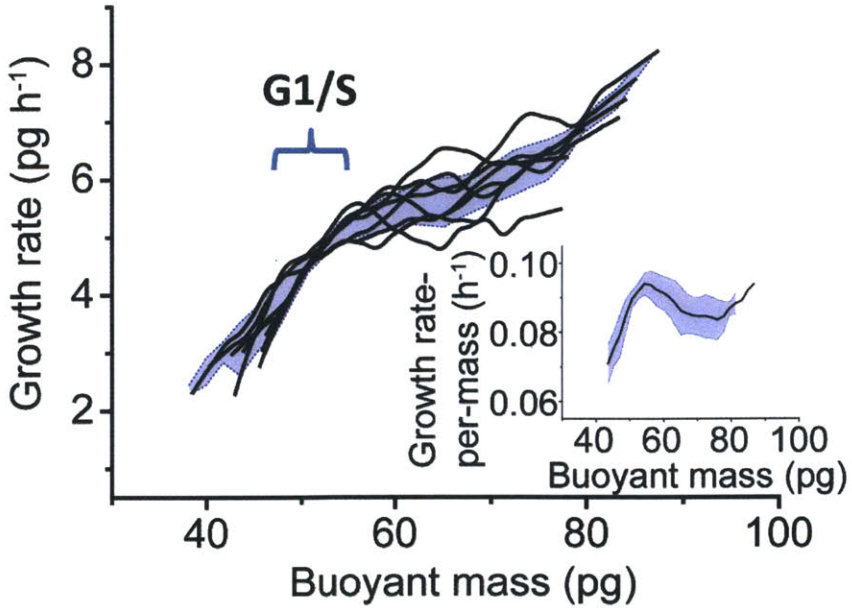

Figure 3-11: Single cell growth rate trajectories (black lines) for a lineage of eight FL5.12 cells. Blue area defines five times the coefficient of variance.

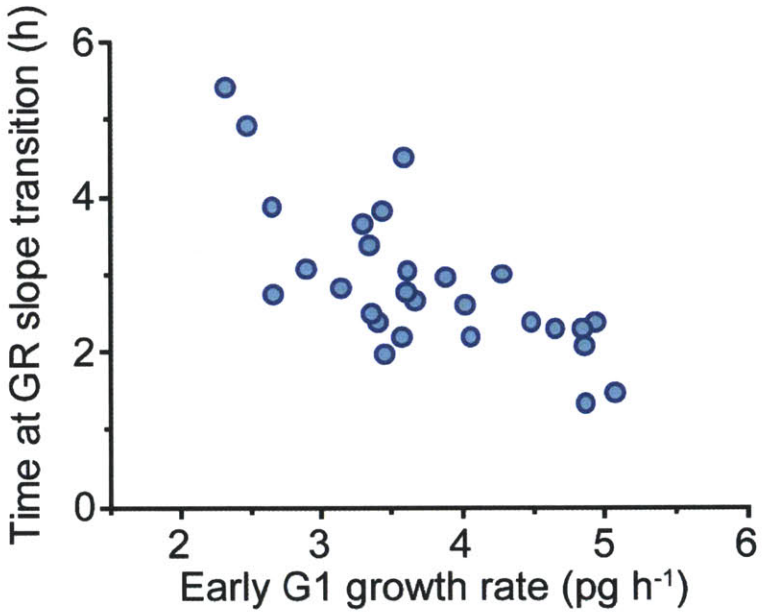

Figure 3-12: Time at G1/S phase transition versus early G1 growth rate for FL5.12 cells. G1-S transition is defined by calculating the growth transition point (n = 28, Pearson's correlation coefficient = –0.72).

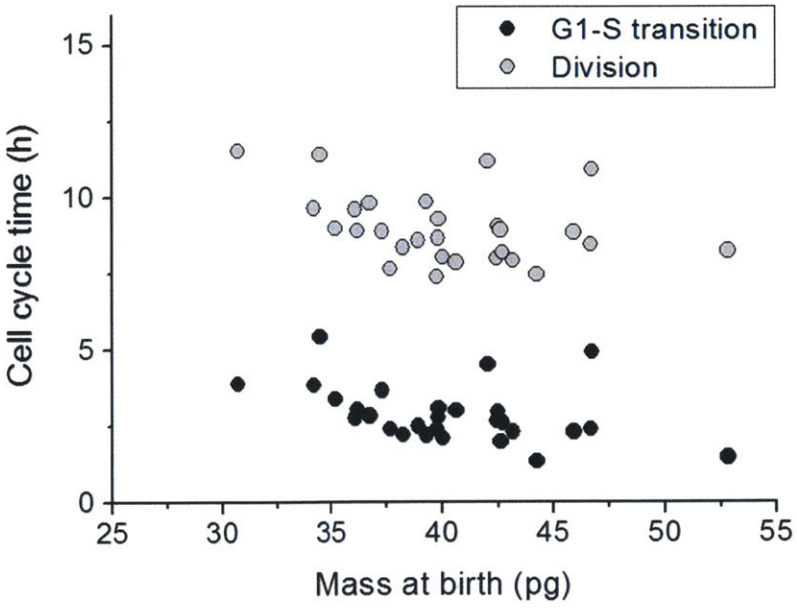

Figure 3-13: FL5.12 pro–B–cell lymphoid cells. Black circles: time at G1–S transition versus mass at birth (n = 28, Pearson's correlation coefficient = -0.42), Grey circles: time at division versus mass at birth (n = 28, Pearson's correlation coefficient = -0.36).

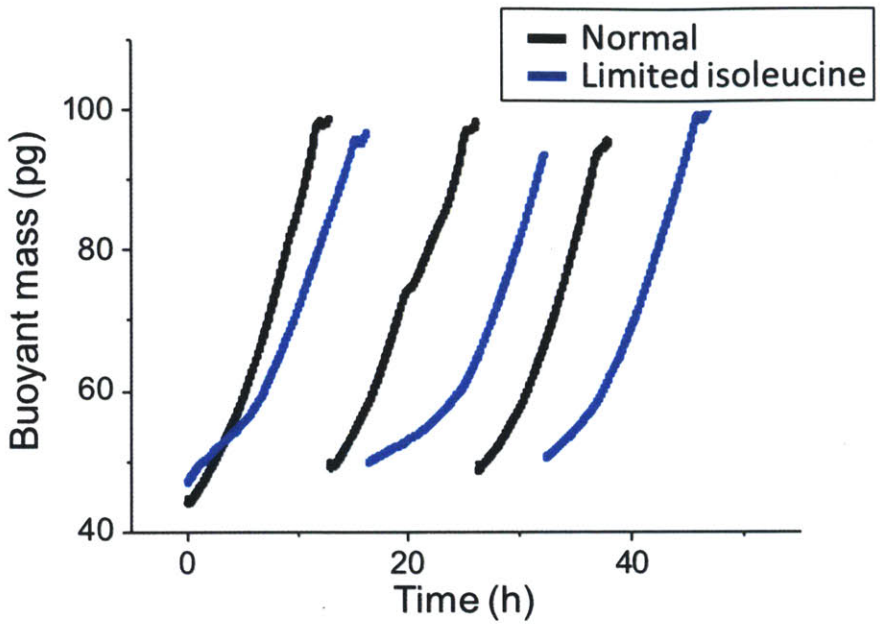

Figure 3-14: Growth of L1210 cells in media with limited isoleucine. The black line indicates cells grown in normal media and the blue line under limiting amount of Isoleucine.

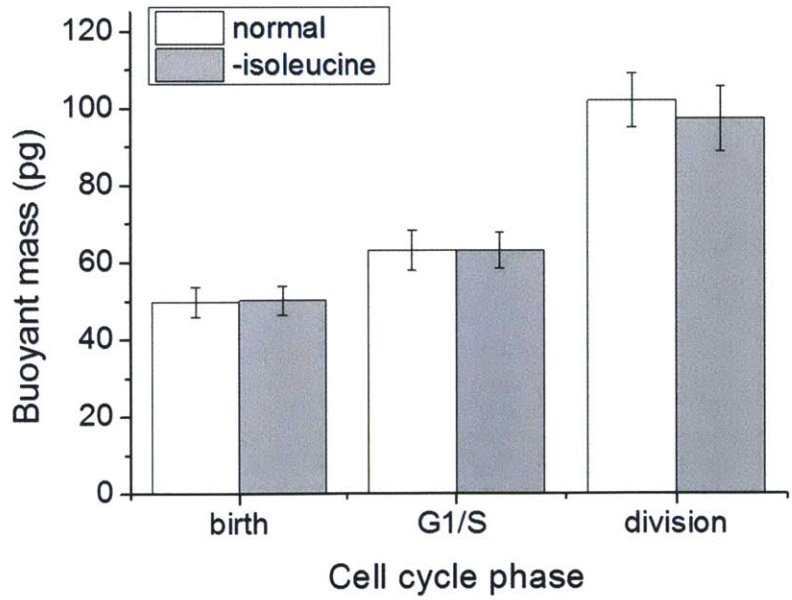

Figure 3-15: Growth of L1210 cells in media with limited isoleucine. The columns show the mean size of cells at birth, G1–S transition and division. n = 77 for normal; n = 17 for limited isoleucine.

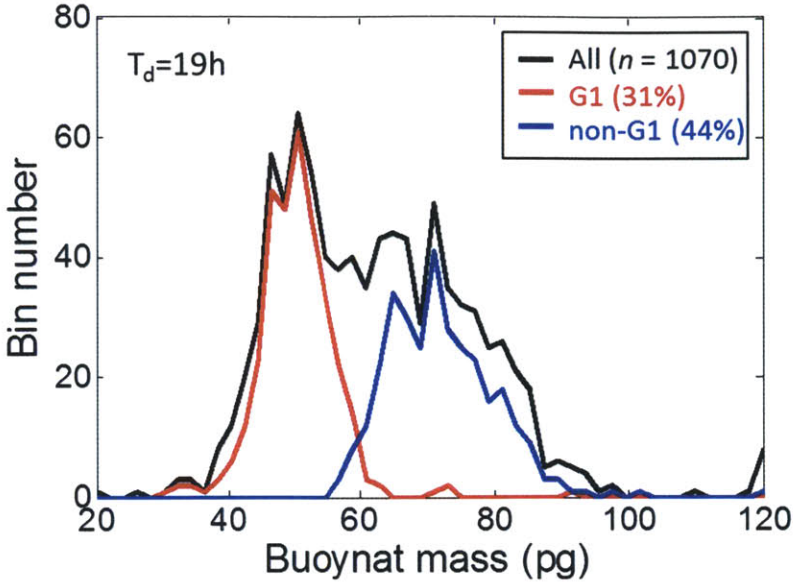

Figure 3-16: Size distributions of a culture grown in limited isoleucine media (19 h doubling time).

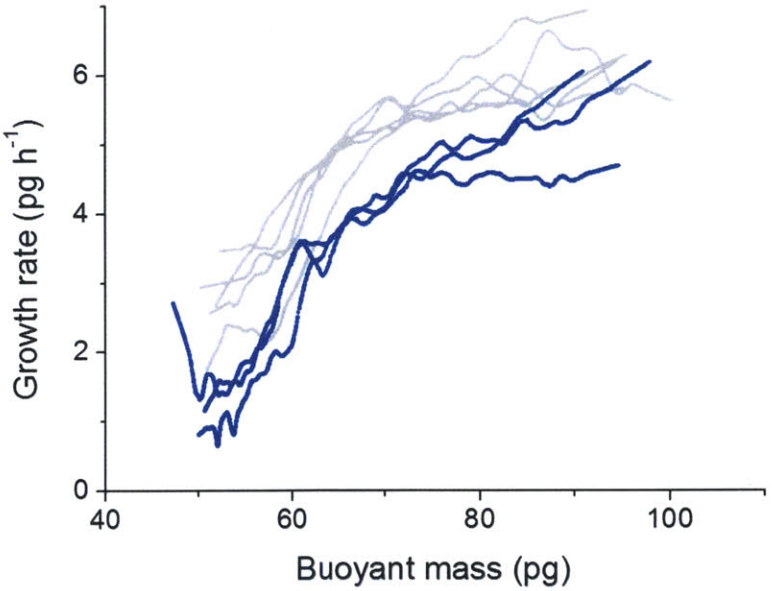

Figure 3-17: Lineage trajectories for cells grown in normal (grey) and media with limited isoleucine (blue).

3.2 Noise in growth and size homeostasis

As previously observed the growth rate-per-mass (specific growth rate) increases throughout G1 and saturate upon G1/S phase transition. It requires that the specific growth rate to drop at some point in cell cycle before the new generation. Fig 3-18 shows that the sudden drop in specific growth rate occurs at every division. We previously speculated that the gradual increase of specific growth rate throughout G1 should result from the regulation of ribosome biogenesis and activity. For it to drop quickly, however, there should exist a process that instantaneously changes the way cells uptake nutrient or synthesize macromolecules.

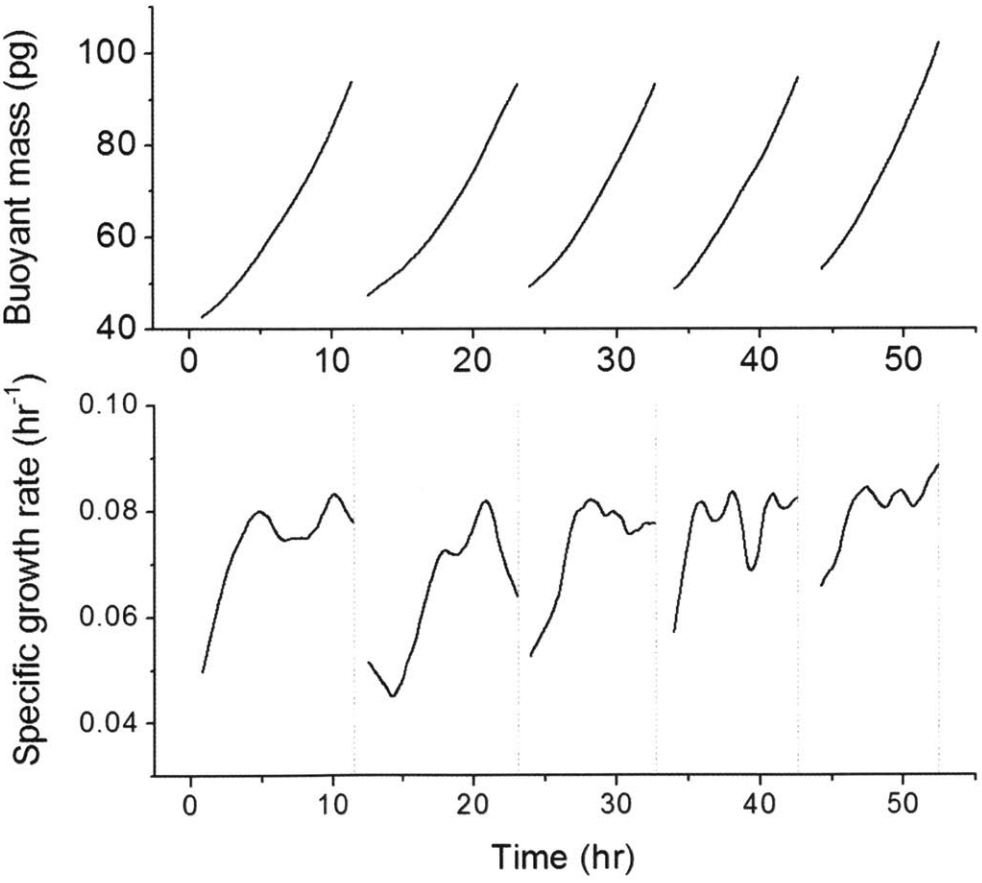

Figure 3-18: Specific growth rate trajectories of L1210 cells for 5 generations. Vertical dotted line indicates the division.

First, we sought to define the process associated with the sudden drop in specific growth rate. For this, we observed the growth profile before and after M-phase. Interestingly, cells maintained the fast growth rate throughout M phase up until cytokinesis (Fig 3-19), which contradicts the canonical belief that cells would not grow during M phase since the RNA synthesis stops [9]. In fact, cells grew at the normal rate throughout the critical events during M phase, such as the breakdown of nuclear envelope, chromosome condensation and segregation, and the intracellular structural changes associated with mitotic spindle and centrosome formation. On the other hand, the growth rate dropped almost immediately upon cytokinesis. It is possible that the cellular uptake is uncoupled from protein synthesis during mitosis and upregulated uptake compensates for the decrease in protein synthesis. Alternatively, reduced RNA synthesis in M phase can result in decreased protein synthesis only in cytokinesis after some delay. Yet another possibility is that somehow protein synthesis actually continues during M phase and decreases only after cytokinesis. To clearly understand this, the level of protein synthesis in M phase has to be precisely measured, which is currently challenging.

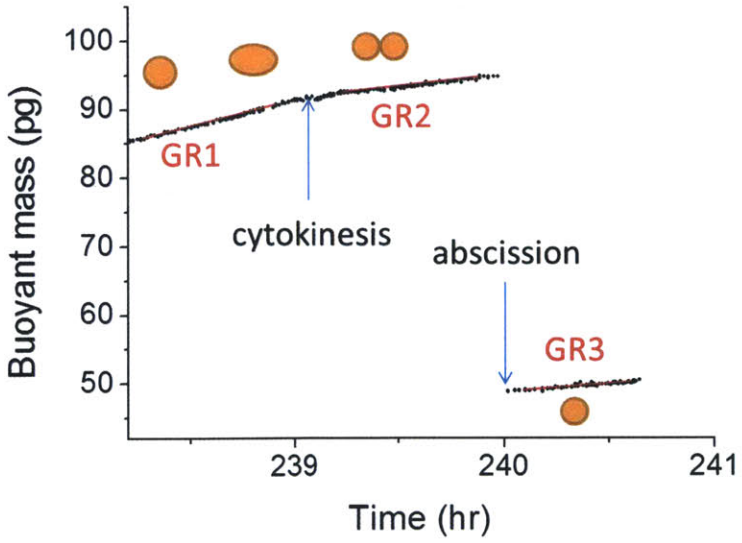

Figure 3-19: Growth during division. To avoid artifact in buoyant mass that can be induced from unstable hydrodynamic focusing, second vibration mode was used for the measurement. Red lines indicate the linear fit of finite sections in time (GR1=7.5pg/hr, GR2=3.3pg/hr, GR3=2.4pg/hr). Orange circles illustrate the geometry of the cell.

To further confirm that the drop in specific growth rate occurs predominantly in cytokinesis and not in abscission, we compared the specific growth rate before and after cytokinesis or abscission. As shown in Fig 3-20, cells exhibited large and variable drops in specific growth rate in cytokinesis but not in abscission. Since we measured the post-mitotic growth rate of only one progeny between the two, it had to be confirmed that one is representative of both. By using the SMR with the extended buried channel (see chapter 4.1), we monitored the growth of both progenies and confirmed that both size and growth rate are almost symmetric between the two related progenies (Fig 3-21). Furthermore, the growth trajectories of the two related progenies are almost identical for the complete cell cycle, whereas the growth phenotype often changes from the mother to daughter (Fig 3-22). This contradicts the findings from other studies, which claim that the variation in growth phenotype is attributable to asymmetric division, and supports that the growth variation results from cytokinesis [39].

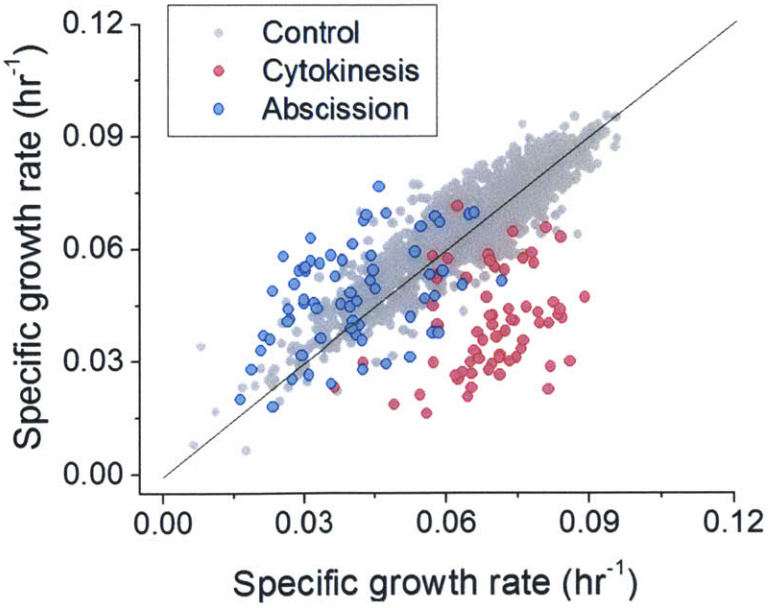

Figure 3-20: Discontinuity in specific growth rate occurs at cytokinesis. Specific growth rate before and after cytokinesis (red), abscission (blue), or 45 minutes during normal cell cycle (grey) are shown. Pearson's correlation for cytokinesis and abscission is 0.28 and 0.42 respectively. Black line indicates the perfect correlation.

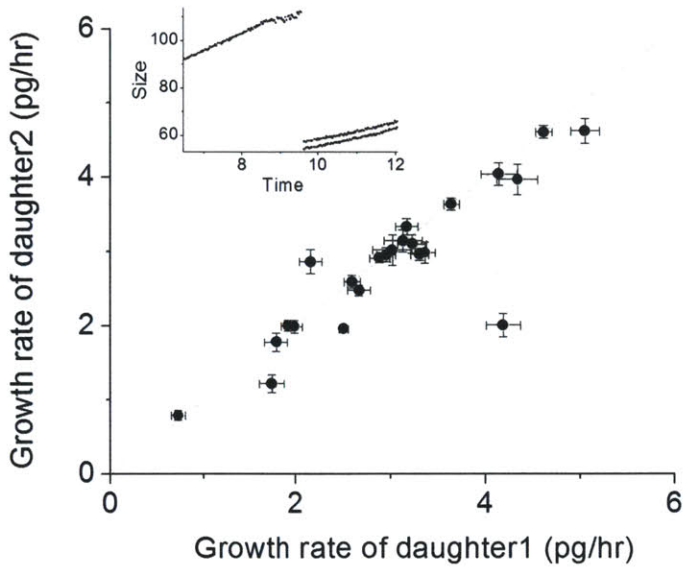

Figure 3-21: Growth rate is symmetric after division. A section of growth curves at newborn was fitted to linear curve. Error bar indicates the confidence of the slope from the linear fit. Inset shows the growth of two related progenies.

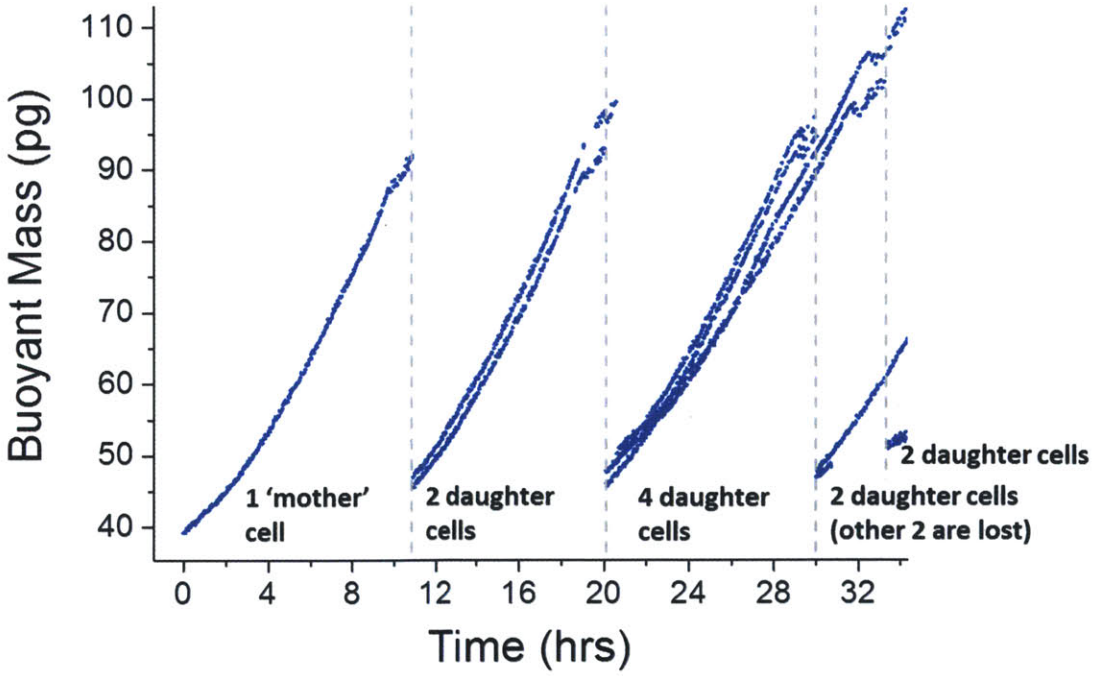

Figure 3-22: Growth of the related progenies. Grey dotted lines indicate division.

What is surprising about the drop in specific growth rate is not only the large magnitude but also the variability. This variability must be responsible for the short-term memory of growth phenotype observed in Fig 22 and it also imposes a large risk in size regulation. To overcome this initial growth rate variability and maintain the mean size in tight interdivision time (see chapter 3.1), cells should actively compensate for this. As shown in Fig 3-23, cells with the low specific growth rate at newborn gradually increase the rate throughout the cell cycle and acquire the threshold specific growth rate before division. This gradual acceleration of specific growth rate requires time as implicated in the negative correlation between the interdivision time and specific growth rate (Fig 3-24).

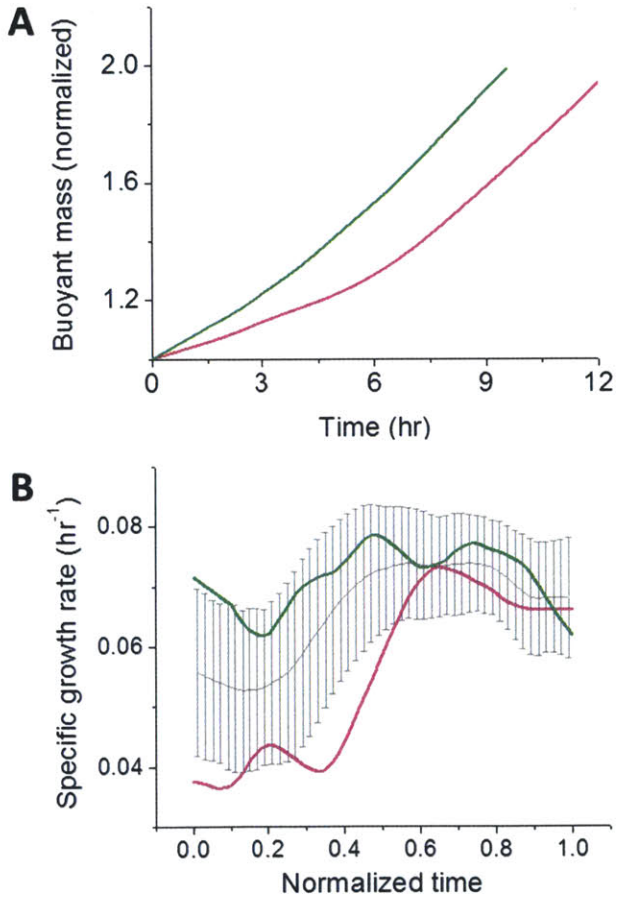

Figure 3-23: A) Representative growth curves with different initial specific growth rate at newborn. Initial specific growth rate is 0.65h^{-1} for green and 0.37 h^{-1} for magneta. B) Specific growth rate trajectories. Grey line shows the average from 122 cells.

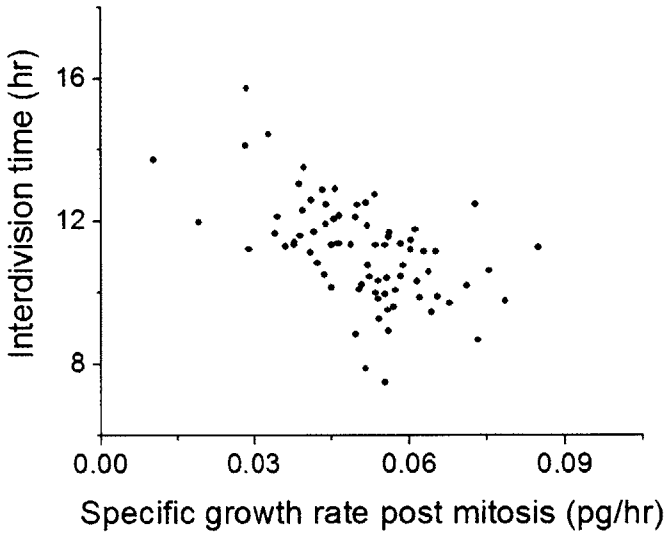

Figure 3-24: Negative correlation between the interdivision time and specific growth rate in newborn.

The elucidation of the mechanism of this discontinuity can be challenging and there can be several different possibilities. Nevertheless, there are several bulk experiments that can provide the key. For example, to verify if the growth rate change is associated with cytokinesis or with some events happened earlier in M phase, one can use drugs such as kinesin-5 or cdk1 inhibitors to increase the length of M phase and check whether the temporal pattern remains or not. To verify if the observed buoyant mass change is induced from a special volume regulation in cytokinesis and the following cell density change, one can measure the density of cells in M phase and compare with the others. To verify if the change in membrane tension during division can affect the transporter activity thus uptake, growth of cells can be monitored under varying extracellular osmotic pressure.

Chapter 4

Higher-throughput growth measurement

So far we have demonstrated the potential of the SMR as a precise growth-profiling tool for homogenous cell lines. However, the low measurement throughput of the SMR is not readily applicable to the study of heterogeneous samples such as primary immune cells or cells derived from patient tumors. In order to characterize the diverse behaviors of heterogeneous cells in a limited time, it is critical to be able to measure them with high throughput. Here we consider two main applications that require different levels of measurement throughput.

First, an efficient immune response relies on the ability of immune cells to asymmetrically divide and differentiate [40]. It has been of prime interest to study the mechanism of immune cell asymmetry and learn how growth is related in the process [41][42]. In particular, whether and how there is a difference in the early growth phenotype between the two asymmetric progenies has been unknown. To study this, the minimum system requirement is to be able to follow the growth of both related progenies instead of only one.

Second, current targeted tumor therapy based on genetic characterization has fundamental limitations since it is simply based on correlation with data from previously studied cohorts of patients [43]. For a successful treatment, it is critical to combine genetics with direct measures of patient tumor cell growth in response to drugs. Existing methods to measure cell growth rely on bulk culture and counting metabolically active cells (e.g. Cell Titer-Glo). However, these bulk assays are slow and inaccurate since tumors such as glioblastoma contain extremely heterogeneous cell populations where a significant fraction of cells have negligible growth rates due to differentiation or senescence [44]. Ideally, one should first identify actively cycling cells and screen drugs based on the immediate growth phenotype change of such cells. SMR is ideal for this since the growth rate of each cell can be determined within 15 minutes. To adapt the SMR for prognosis of such tumors, however, the throughput has to be increased 10 to 100-folds.

In this chapter we describe the two different engineering approaches to achieve these aims. Even though the findings here present only a proof of concept, the information garnered here will be indispensable for implementation of the practical device.

4.1 Simultaneous measurement of a series of cells

To monitor growth of multiple cells, we introduced the extended serpentine buried channel (Fig 4-1). The design made use of posts placed on both sides of the SMR to trap up to about 6 cells. First, cells were loaded in through the posts by applying a relatively high initial pressure drop across the SMR. Then by alternating the pressure drop between the two adjacent bypass channels, the cells flew back and forth through the SMR. Loading pressure was determined by considering the deformability of the cell and the gap between the posts. In the current study, 3psi was enough to move relatively deformable L1210 or FL5.12 cells through the 3μm gap. When trapping, the upper pressure limit was determined to retain the cells within the buried channel and the lower pressure limit was determined to avoid inertial trapping at the tip of the SMR, or to avoid sticking. For the given design,

about 0.03psi was used for trapping. Cells moved either every 60s or 90s to minimize the shear stress that cells experience during the passage through the small buried channel.

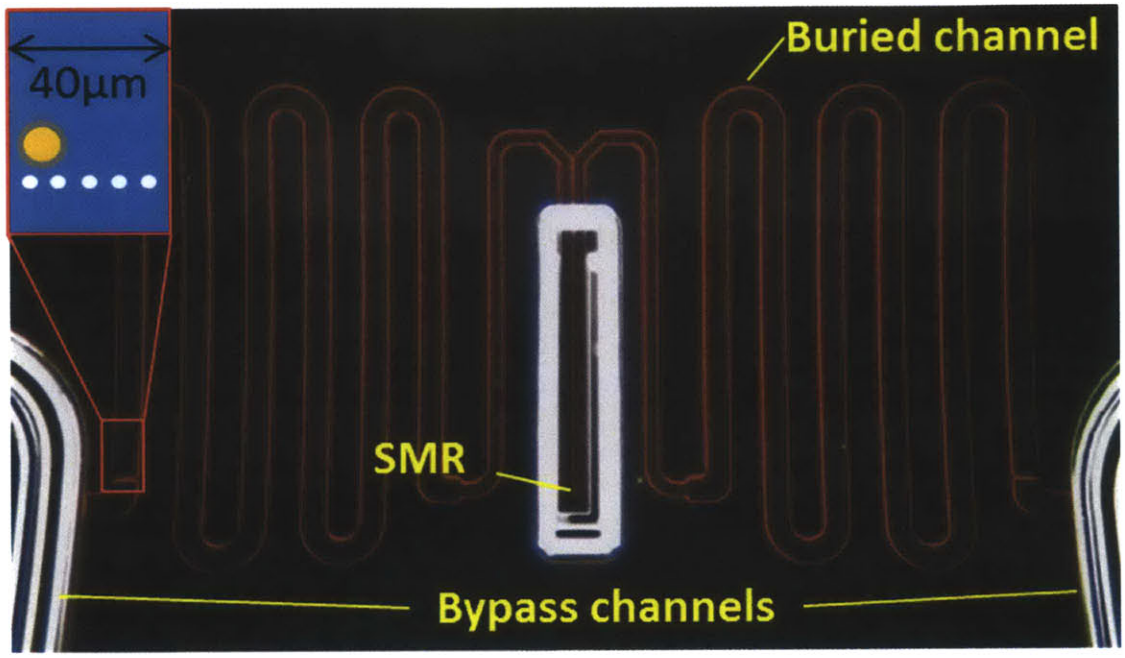

Figure 4-1: Micrograph of the SMR with the extended serpentine buried channel. Serpentine part of the channel is wider (40μm) than the SMR (20μm) and minimizes the shear stress cells experience during transit. A series of posts are placed at both ends of the serpentine channel. Total length of one side of the serpentine channel is about 5mm, which is long enough to contain about 6 cells with spatial separation.

As shown in chapter 3.2, this enabled the growth trajectories from all the cells within the buried channel to be measured over long time periods, even if the order of the cells was altered. Since the mass precision of the SMR is near 0.05%, ideally each cell can be uniquely identified by its mass measurement. However, overlapping peaks reduced the measurement precision and eventually limited the number of cells that can be simultaneously measured. Overlapping peaks were introduced when the distance between two cells randomly became so small that both cells in transit resided in the sensitive part of the SMR at the same time. To address this, the overlapping peaks were fitted based on the analytical curve and the

buried single peaks were deconvoluted (Fig 4-2). Briefly, a single or group of peaks was first selected depending on the distance among the peaks. For the selected peaks, baseline slope and the position of apexes were predetermined based on a specific threshold. Afterwards, an analytical curve was fitted to the data with two free parameters: peak width and peak height. Once the best fit was found by the iterative search, the peak height was adjusted to reflect the apex shape difference of the analytical and real peak. This method works for more than two overlapping peaks. Fig 4-3 shows the accuracy of the deconvolution depending on the distance of two cells.

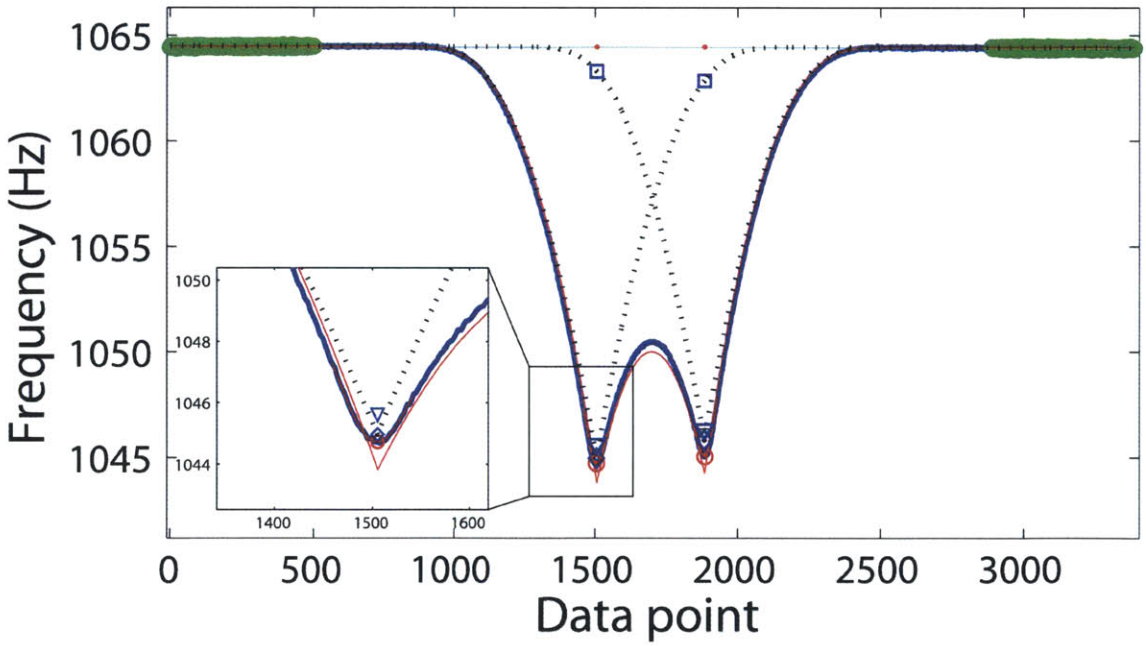

Figure 4-2: Deconvolution of multiple peaks. Blue curve and green line show the raw data and baseline respectively. Two individual peaks of the analytical shape were fitted to raw data (red curve) and each peak was deconvoluted (black dotted curves). Red dots indicate the position of the peaks. Blue squares show the mass contribution of the other peak to the current one. (Inset) Red open circles show the apex of the raw data, which is lower than that of the reconstructed curve since the cantilever width at the tip is not infinitesimal thus the turn is not as sharp. The gap between the two was subtracted from the deconvoluted peak (blue diamond) and shown in the blue triangle.

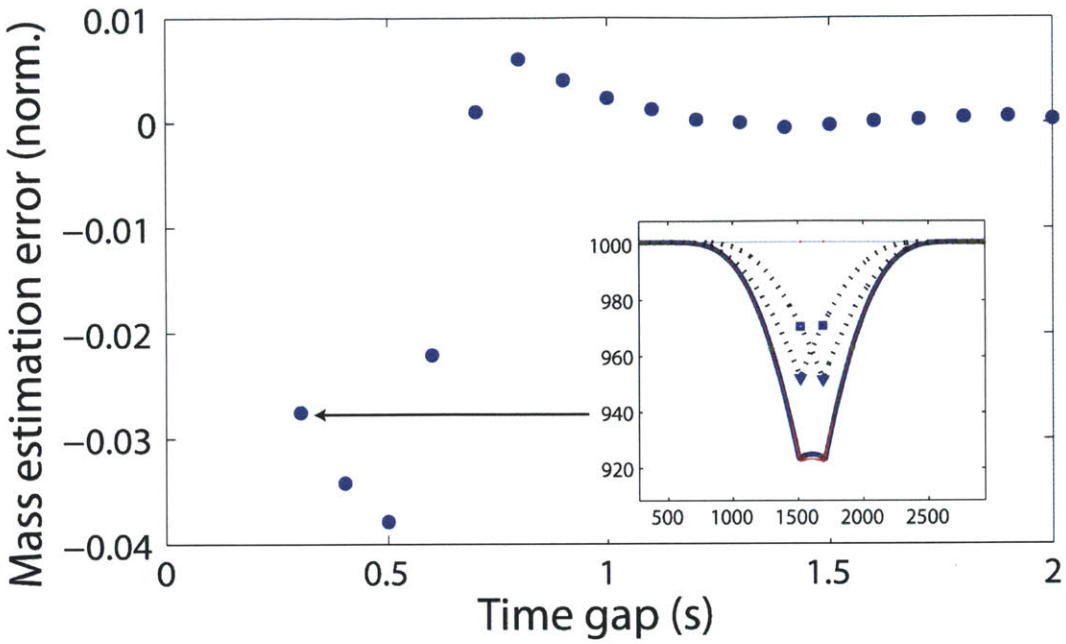

Figure 4-3: Mass estimation error of the deconvolution method. Two peaks of varying distance were simulated and fitted using the deconvolution method. Each peak was simulated to have the full width half maximum 0.4 second, mass 60pg.

Even though the device functioned as designed, two main problems prevented the stable long-term monitoring of multiple cell growth. First, there was a large variation in the flow rate of cells. Part of the variation was induced by the size of the cell (Fig 4-4). As a cell grows bigger it blocks more channel cross-section, making the flow profile more plug-like around the cell rather than parabolic, which in turn makes the linear flow rate of the cell slower. On the other hand, even larger variation often resulted from the surface stickiness of cells. Even though all the channels in the device were coated with PEG (1 mg/ml, PLL(20)-g[3.5]-PEG(2), Surface Technology) for passivation and this almost completely prevented cell sticking during normal trapping, cells in the extended SMR could stick due to the low flow rate that was used. The stickiness depended on the size or type of cells. This was particularly problematic since it caused some or all of the cells in the channel to not transit through the SMR (Fig 4-5), which resulted in the partial loss of data or complete stop of the run. To address this, it is necessary to establish a super-low fouling surface using molecules such as zwitterionic polymers [45].

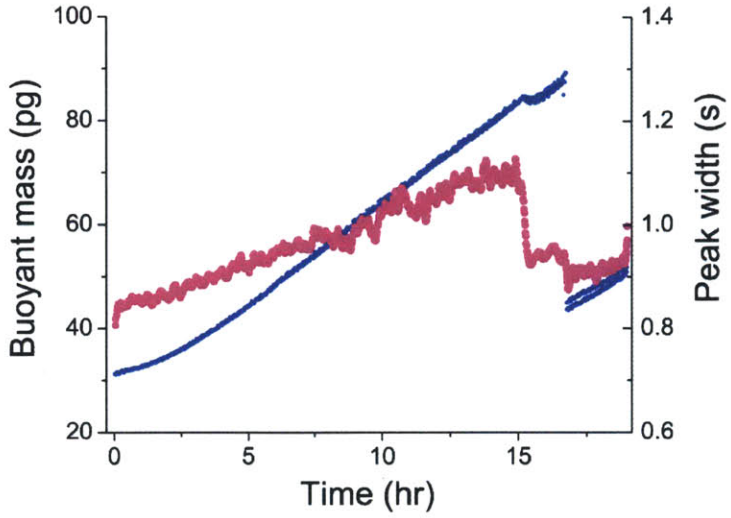

Figure 4-4: Flow rate of the cell decreases with the size. For a cell trapped for the complete cell cycle, peak width (FWHM) increased with the size and dropped upon cytokinesis. Blue and magenta indicate the mass and peak width of the cell respectively.

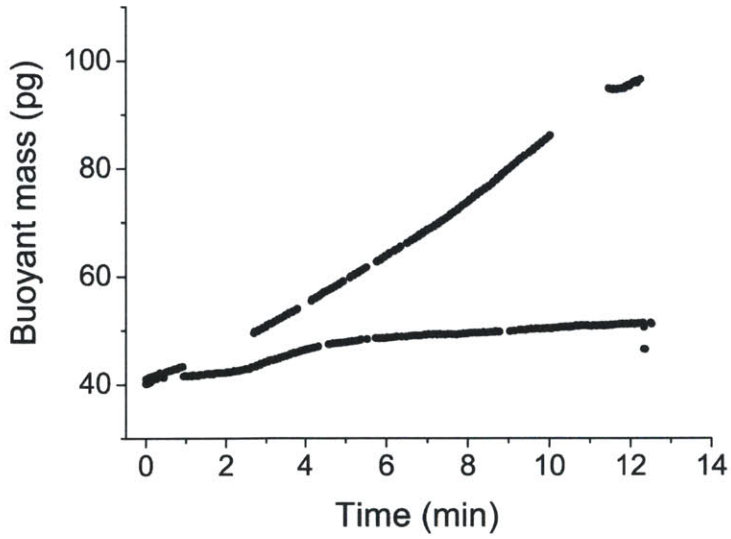

Figure 4-5: Mass measurement was skipped due to the flow rate variation. Two related progenies that exhibited different growth phenotypes were trapped together for about 13 hours. Missing part of the trajectories indicate only one cell transit through SMR.

Second, we suffered from unhealthy growth of cells in the extended buried channel particularly when measured in the second vibration mode. We wondered if the strong acoustic actuation required for the second mode caused too much mechanical vibration that could be detrimental to cells. To test this, we made a mock device that contains all the fluidic features except for the suspended microchannel. Using a microscope, we were able to visually confirm that cells grew normally in the mock device under the same flow conditions used in SMR. This suggested that the vibration of the cantilever or the whole chip could be harmful for cells within the confined channel connected to the cantilever and abolished the possibility that shear stress or nutrient delivery limited the cell growth. Since cells grew well in the normal SMR even in the second vibration mode, we assumed that the vibration of the cantilever rather than the whole chip caused the detrimental effect. One plausible hypothesis is sonoporation, which is a phenomenon deliberately used for cellular delivery of macromolecules since the ultrasonic frequency wave can modify the membrane permeability of cells [46]. It has previously been shown that SMR can pump fluid in and out if the embedded channel is asymmetrically etched about the midplane of the cantilever [47]. It is possible that about 1MHz ultrasonic waves generated by the cantilever pumping affect the cells confined in the extended channel. However, since the power of ultrasonic wave depends on several parameters that are hard to characterize such as asymmetry of embedded channel or dissipation of energy within the extended channel, it would be more practical to redesign the fluidic path that includes buffers between the trap structures and the cantilever.

4.2 Trap-and-release

Even though the serpentine SMR helped monitor the growth of more than one progeny, it did not substantially increase the measurement throughput due to the overlapping peaks that ultimately limit the maximum number of cells. In addition, identification of each cell based on mass suffered as the number of cells in the channel increased since it contained more number of similar size cells. The fact that

cells have to go through the posts in loading raised a concern about the condition of cells after loading as evident from the observation of giant cells (Fig A-4), or about the feasibility of trapping less deformable cells. Finally, the scalability of the serpentine design is limited. When operating the array of extended buried channel SMRs, each SMR will require slightly different timing for switching the applied pressure drop. Even though the difference will be small for adjacent SMRs, large arrays will suffer from significant variations that will cause cells to be uncontrollably ejected into the bypass channels.

To address this limitation, we adapted a microfluidic structure originally introduced by Tan and Takeuchi that exploits hydrodynamic forces to reliably trap and release a large number of particles [48]. By placing this structure on either side of the SMR with opposing orientations, cells could sequentially pass through the SMR and be subsequently captured without the need for precise timing for switching the applied pressure between the bypass channels (Fig 4-6). Consequently, each cell was able to be identified based on the sequence of their transit, not their mass. Once a group of cells have been measured, a large pressure drop across the bypass channels could be used to eject them.

For the current study, the dimensions and arrangement of the trap and release structures was optimized for the lymphocytes and considering the integration with the SMR. Fig 4-7 and Table 4-1 shows the design parameters of the trap and release structure. W, L, and H are the width, length, and the height of the channel respectively. Q denotes the volume flow rate. Two sets of the main (path2) and narrow (path1) channel dimensions were determined based on the three criteria: First, trapping efficiency, which is proportional to the flow rate ratio Q1/Q2, should be maximized. Second, the change of flow rate Q1/Q2 upon trapping a cell should be maximized. Third, the distance between the two cells in transit has to be larger than the flow path of the SMR to prevent overlapping peaks. Since the normal lymphocyte of diameter 10μm fills half the width of the path upon entering to the branch, it was predicted that Q1/Q2 of 4 guarantees almost complete trapping [48]. Q1/Q2 when a trap is occupied was calculated based on an assumption that cells moderately stretch vertically when blocking the slit of path1.

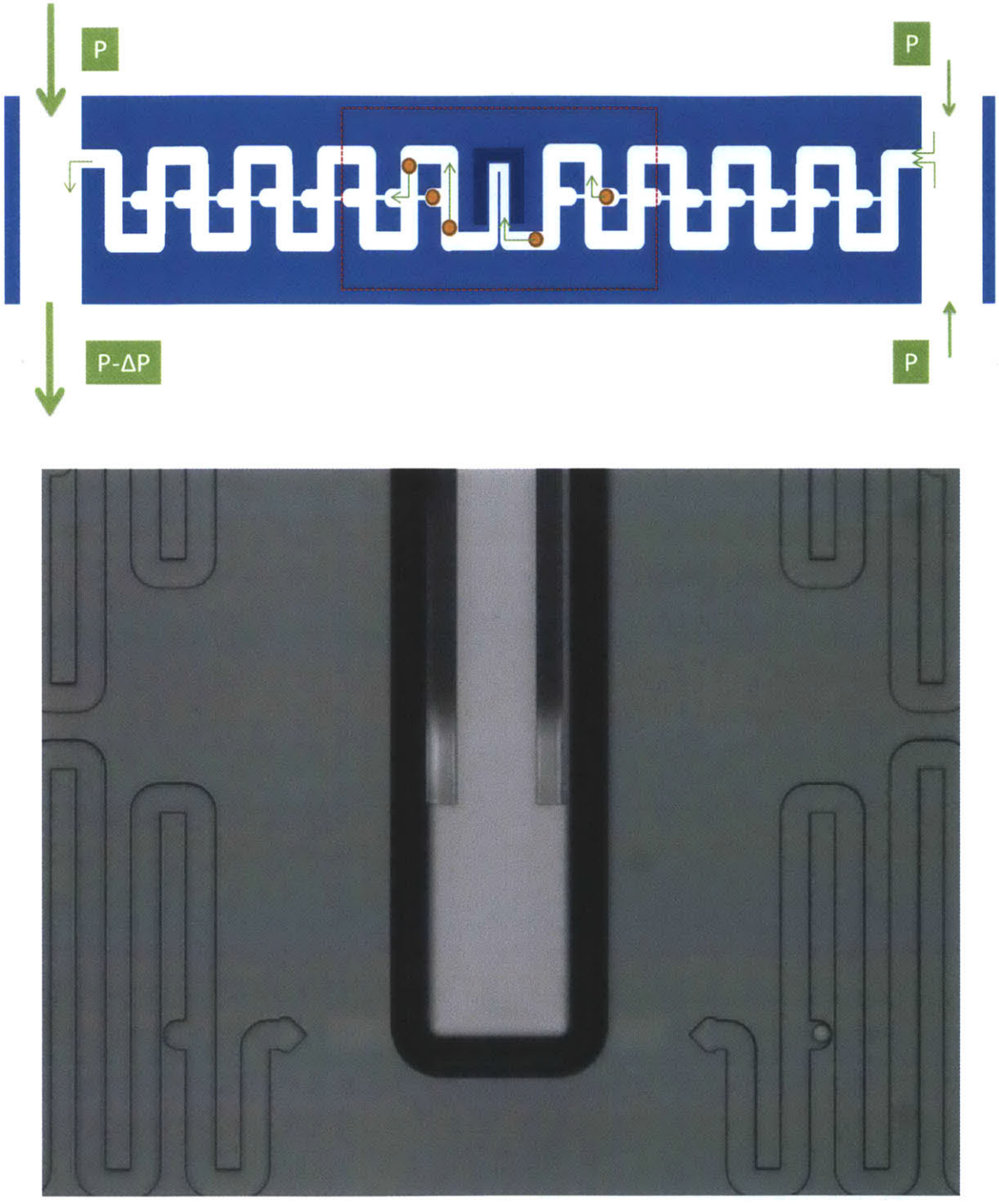

Figure 4-6: Illustration and micrograph of the SMR / trap-and-release. Green arrows qualitatively show the direction and rate of flow. In the micrograph (marked with the red box in the illustration), a cell is trapped in the pocket on the right hand side.

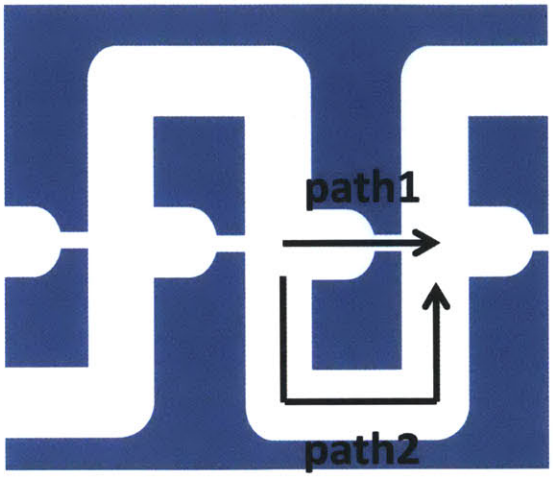

Figure 4-7: Illustration of the trap and release structure. Path1 is the direct path with lower resistance when not occupied, path2 is the alternative path.

	W1	L1	W2	L2	H1	H2	**Q1/Q2**
1 (unoccupied)	7.5	4.8	20.0	180.0	18.0	18.0	**3.863**
1 (occupied)	7.5	4.8	20.0	210.0	8.0	18.0	**1.219**
2 (unoccupied)	5.0	3.0	20.0	325.0	18.0	18.0	**3.700**
2 (occupied)	5.0	3.0	20.0	325.0	5.0	18.0	**0.525**

Table 4-1: Two different sets of trap-and-release dimensions. In both cases, Q1/Q2 is about 4 when unoccupied.

The minimum number of traps was determined to prevent the net flow rate from changing too much as each pocket is occupied. If the net flow rate changes substantially from the transit of one cell to the other, the resulting shear stress variability may cause detrimental effect. The series of trap-and-release structures can be modeled as a circuit with resistors connected in series and parallel. Fig 4-8 shows that the flow rate decreases as more traps are occupied for varying number of total traps. We determined the minimum number of traps to be 8 to limit the flow rate ratio between the first and the last cell within half.

After testing the designs with L1210 cells, we found that two main problems limit the stable trap of multiple cells. First, the flow path of cells at the time of passage to the trap area predominantly determined the fate of trap (Fig 4-9). This was different from the estimation that Q1/Q2 of 4 would guarantee almost complete success of trap and implies that the streamline of flow has to be carefully designed. Another unexpected observation was the back-trap (Fig 4-10): when transiting to the reverse direction cells were trapped in the backside of the trap-and-release pocket. This could occur since the cells only partially blocked the slit and the fast flow through the partial opening could exert high shear force that kept the cells stuck. Once stuck, cells could deform to avoid the main flow. For reliable operation the design has to be improved considering the flow path and deformability of the sample.

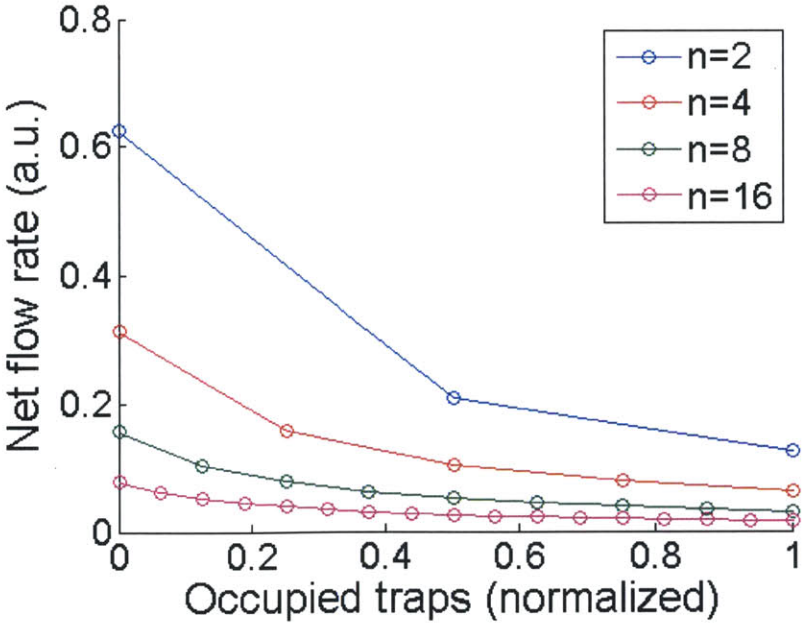

Figure 4-8: Net flow rate change as a function of total number of traps and their occupation. Q1/Q2 was assumed to be 4.

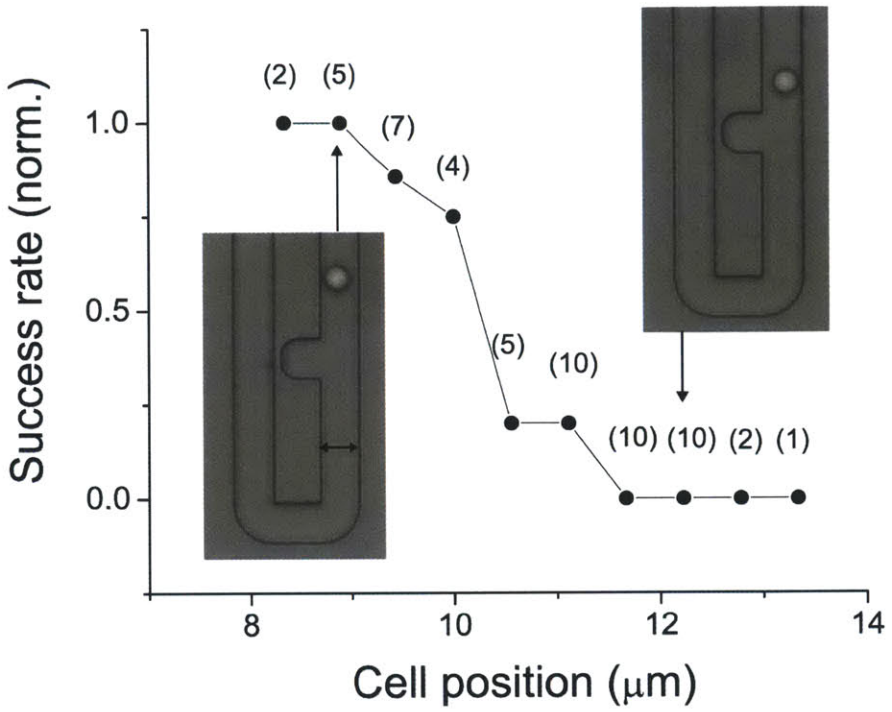

Figure 4-9: The fate of trap depends on the flow path of cells. Snapshots were taken from the video right before the cell passed the trap area. Using Matlab image processing, we calculated the center of the cell with respect to the channel walls (channel width is 20μm as indicated by the arrow, position of left wall is 0). Numbers above the dots indicate the total count of data point. For the measurement, only snapshots that contained similar cell size (13μm) were used.

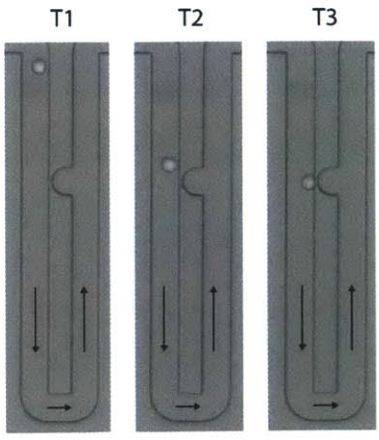

Figure 4-10: Illustration of back trap in sequence. Black arrows indicate the direction of flow.

If we maintain ten cells per SMR/trap-and-release structure and operate several tens of SMR/trap-and-release structures between a pair of bypass channels (Fig 4-11), a conservative throughput estimate would be that the instantaneous growth rate of several hundred cells could be measured in 15 minutes. Assuming it takes a few minutes to reload a new group of cells in each trap-and-release structure, it should be possible to measure over a few hundred cells per hour.

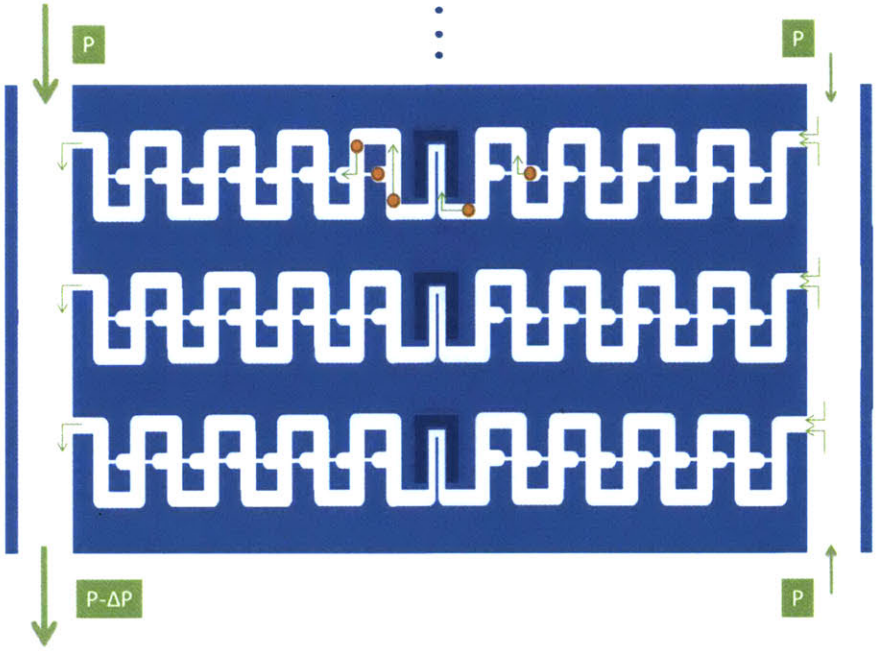

Figure 4-11: Illustration of the SMR/trap-and-release array

Chapter 5

Growth response to nutrient deprivation

Traditionally, radiolabelling of nutrients, mass spectrometry, and other techniques have enabled the mapping of metabolic flux within a cell [49]. Even though this has advanced understanding of steady-state flux of nutrients and metabolites it only partially revealed the metabolic requirements for cell growth, which is dynamic and complex. In this chapter, we describe the engineering advancements that enabled precise monitoring of growth immediately after nutrient depletion. The findings from the depletion of glucose or glutamine showed an immediate and reversible slowdown of cell growth, whose magnitude was much larger than what was expected based on the loss of simple uptake. As noted, the accounting of metabolites alone is not yet able to show the extent of signaling involved. On the other hand, growth response of cells to the depletion of nutrients is known to capture the essence of complex reactions associated with the particular metabolism. Long-term proliferation of bulk culture has often been monitored to understand the

essentiality of nutrients and predict the signaling pathways that are triggered upon the loss. We envision that short-term growth response to depletion will provide clues to the extent of active reactions and signaling, presumably more specific and different from those in longer-term.

5.1 Method of fluid exchange

Gentle and rapid fluid exchange surrounding a cell in the SMR is a major engineering challenge. Previously, we exploited the aspect of fluid replenishment in the dynamic trapping to deliver the new fluid to a trapped cell [50]. For this, we first exchanged the sample vial upstream of the SMR to the one that contained the new fluid following the trapping of a cell. After the growth of the cell was measured with the normal trapping for certain period of time we simply increased the trapping frequency, which accelerated the loading of new fluid from the sample vial. Upon completion of fluid exchange, we restored the normal trapping for further growth monitoring. This method raised a concern since it required at least 5 minutes of high frequency trapping to complete the fluid exchange, imposing high shear stress to the trapped cell. Even though the effect of this shear stress on cell growth was carefully tested and found negligible, the stress and complexity of the method essentially limited the number of fluid exchange to one. Furthermore, the method did not allow mass measurement during exchange, possibly masking crucial characteristics of the initial response. To address these concerns and gently exchange the fluid surrounding a cell while constantly measuring the mass, we devised two independent methods.

First, we exploited the high resistance of the extended serpentine SMR to rapidly exchange the fluid in the bypass channels while retaining the cells in the buried channel (Fig 5-1). In a normal SMR, it was impossible to avoid leakage flow when generating fast flow in both bypass channels at the same time and this prevented us from retaining a cell in the buried channel during the fluid exchange.

However, the extended buried channel exhibited substantially slower leakage flow due to its high resistance and this leakage flow was able to be further limited with the help of hydrostatic pressure balancing. This allowed fluid in both bypass channels to be exchanged simultaneously while safely retaining cells in the buried channel. This not only minimized shear stress experienced by the cell during exchange but also shortened the duration from 5 minutes to tens of seconds. To make it easy to exchange fluid from two different sources multiple times, a selection valve was included upstream. This method of fluid exchange was promising since it guaranteed the complete fluid exchange for multiple cells at once. However, the fluid switching and hydrostatic pressure balancing had to be manually executed, which made the process impractically laborious.

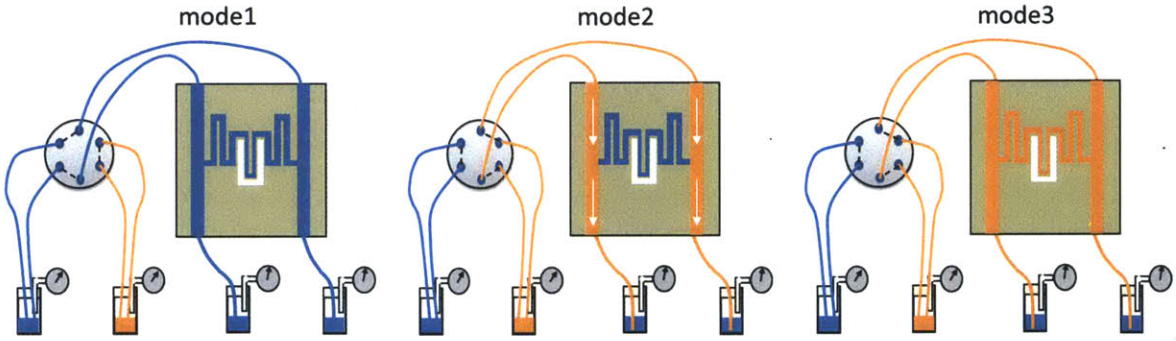

Figure 5-1: Illustration of fluid exchange using the extended serpentine SMR and a selection valve. Two vials that contain different fluids were connected to the source tubing via a selection valve. First, growth of several cells is measured (mode1). For fluid exchange, the measurement is paused and selection valve switches to feed another sample (mode2). Large pressure gradient is maintained across both bypass channels and the new fluid is replenished. The plug of old fluid in the buried channel is removed during a few subsequent trapping (mode3).

We deployed this method to minimally modulate the environment of the cells and monitor the growth response. First, a L1210 cell exhibited an instantaneous and large growth rate change when growing in the media that lacks 2mM glutamine (Fig

5-2). The growth was restored upon repletion of glutamine. This will be discussed in more detail in chapter 5.2. Second, the long-term effect of interleukin-3 (IL-3) depletion to FL5.12 cells was monitored. As demonstrated in Fig 5-3, this method allowed fluid to be exchanged for more than one cell at once. IL-3 regulates glucose uptake and metabolism and thus maintains mitochondrial homeostasis and enables anabolic pathways required for cell growth. It is found that the genes involved in glucose uptake and glycolytic commitment, those for Glut1, hexokinase 2, and phosphofructokinase1, rapidly declines following growth factor withdrawal [49]. However, our initial finding suggests that the growth can continue for several more hours even without the IL-3 and cells do not become smaller during the ongoing generation until they divide. Therefore, previously observed cell size reduction in population-level upon IL-3 withdrawal may not accurately describe the process of size change in single cell level.

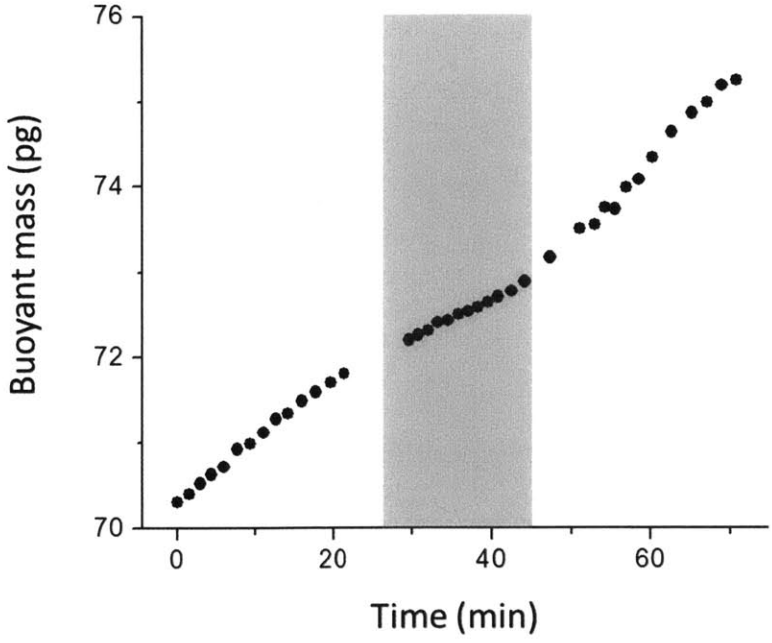

Figure 5-2: Growth of a L1210 cell upon depletion and repletion of glutamine. The buoyant mass was measured in about every one minute. Grey box marks the duration where glutamine was depleted. Mass measurement stopped for about five minutes during the fluid exchange.

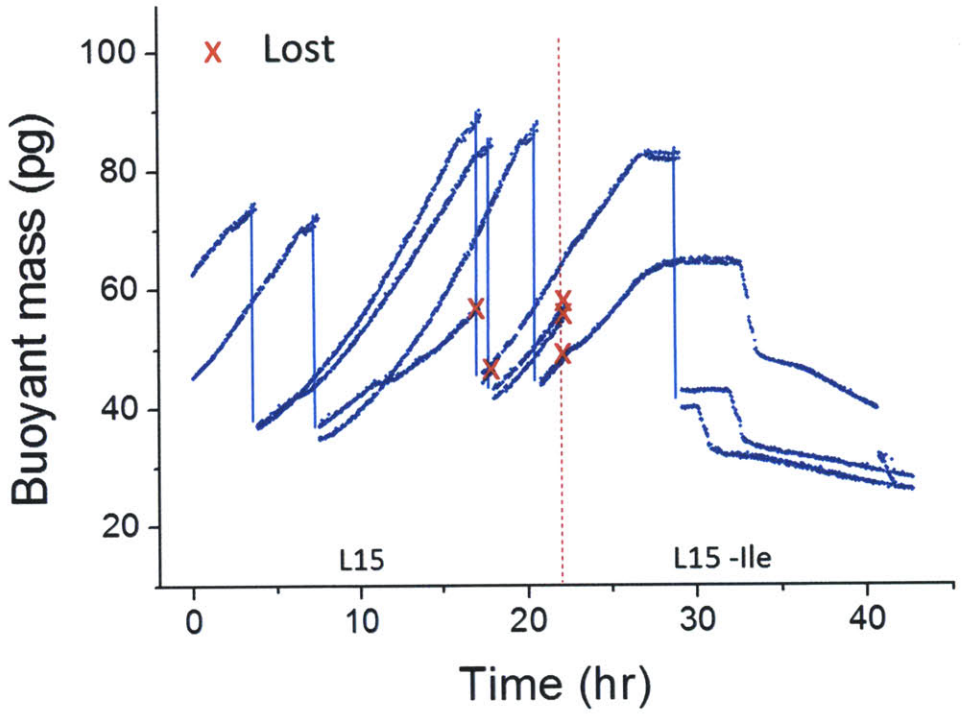

Figure 5-3: Growth of FL5.12 cells upon depletion of IL-3. Red line indicates the exchange of the fluid to the media that lacks IL-3. Blue vertical line marks the division and red cross marks the lost cells. All the three cells grown under IL-3 depletion went through the rapid-loss-of-mass.

Second, we took an alternative approach by filling two different fluids in each bypass channel and modulating the resident time of a cell between them. Instead of the normal trapping, where the cell spends equal amount of time in each bypass channels, this scheme maintained the cell mostly in one side and brought it to the other side only momentarily for the mass measurement. This way a cell spends more than 90% of its time in one fluid during the corresponding cycle (Fig 5-4). Since this method did not require the actual exchange of the fluid, it allowed very rapid and flexible fluid exchange without elevated shear stress exacerbating the cell. However, the simplicity came at the cost of short exposure of a cell to the opposite side fluid. Furthermore, the leakage flow through the cantilever in each cell transit could introduce some of the other fluid. We carefully characterized the effect of this by undertaking two independent controls.

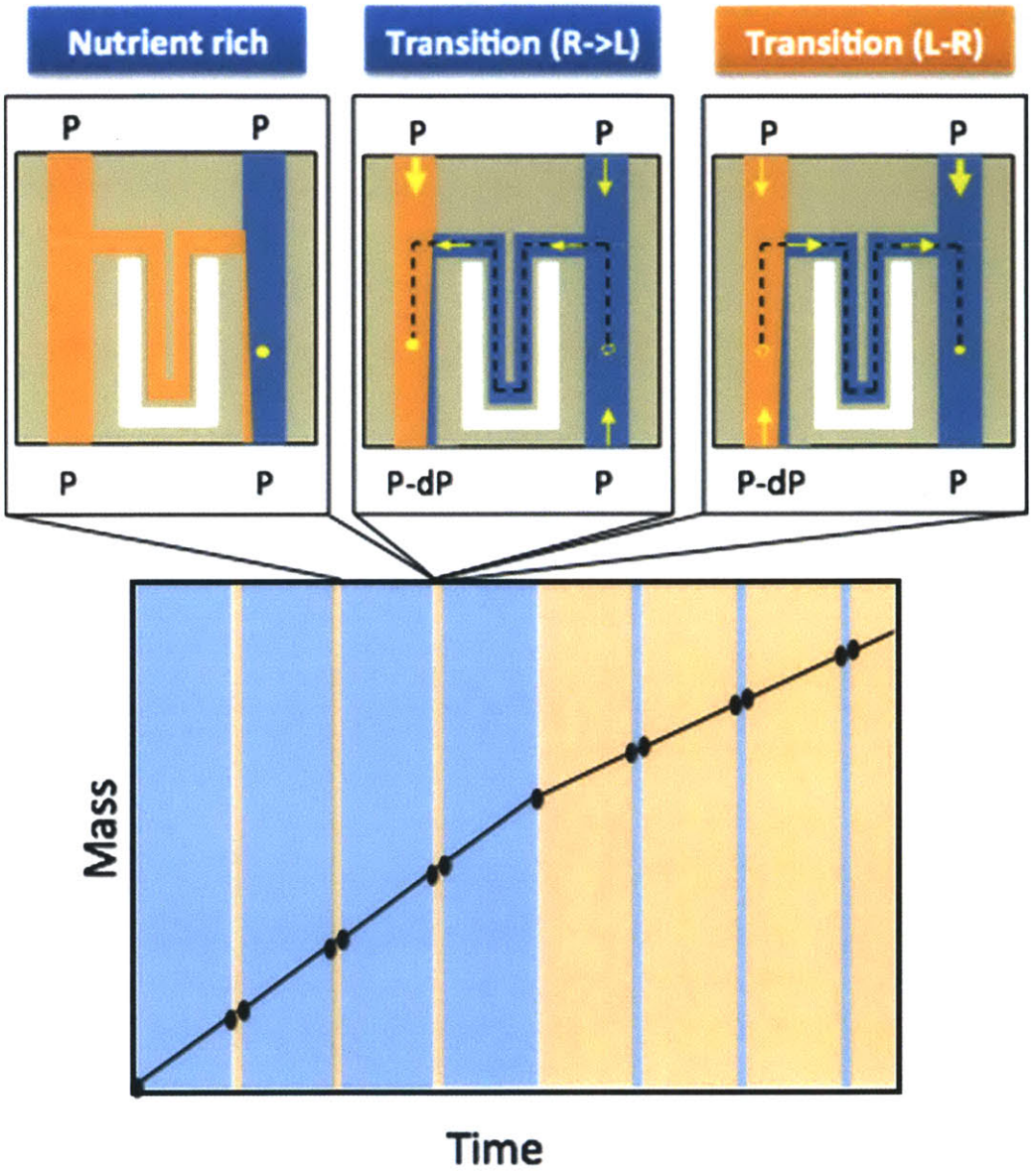

Figure 5-4: Illustration of the instantaneous fluid exchange method. First, a cell stays in the nutrient rich media for the specified period (usually 90 seconds, thick blue columns in the bottom plot). Afterwards, the cell moves to the other side bypass channel and immediately returns back (usually less than 10 seconds, thin orange columns). The mass is monitored in the process (black dots). This duty cycle continues for one repletion cycle and the depletion cycle begins with the reverse duty cycle.

First, to confirm that the short exposure to the repletion media during depletion cycle has a negligible effect, or *vice versa*, we measured growth between the complete RPMI media and PBS (Fig 5-5). To minimize an artifact in buoyant mass induced from osmotic volume change, the osmolarity of RPMI media was adjusted to match PBS by adding a specific amount of Mannitol (Sigma-Aldrich). The initial growth in the repletion cycle showed normal rate for the given size, which is confirmed by comparing to the long-term growth measurement of cells in normal media (data not shown). On the other hand, there was no mass accumulation when in PBS, supporting that the effect of short exposure to the repletion media was negligible. The slow reduction of mass in PBS is an indication of constant cell secretion.

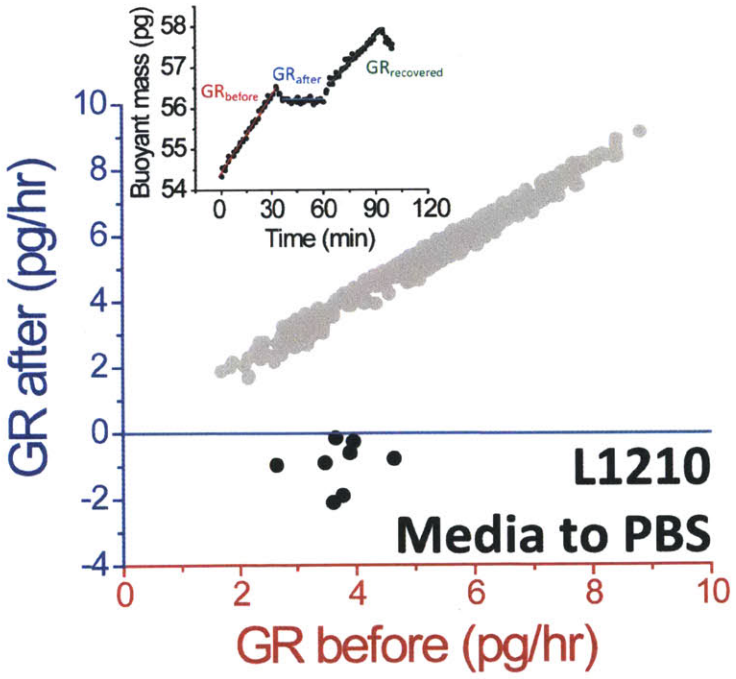

Figure 5-5: Environmental exchange negative control. Growth of cells in PBS was compared to growth in complete media before depletion. For this, initial growth, depleted growth, and repleted growth were measured for 30 minutes respectively and linear fit gave the instantaneous growth rate (inset). For control, growth rate of two consecutive 30 minutes setions were compared at arbitrary points in cell-cycle (grey dots).

Second, to confirm that growth responds to the absolute level of depletion and not to the gradient, we depleted glucose to multiple levels above the physiological concentrations. As shown in Fig 5-6, there was no significant change in growth.

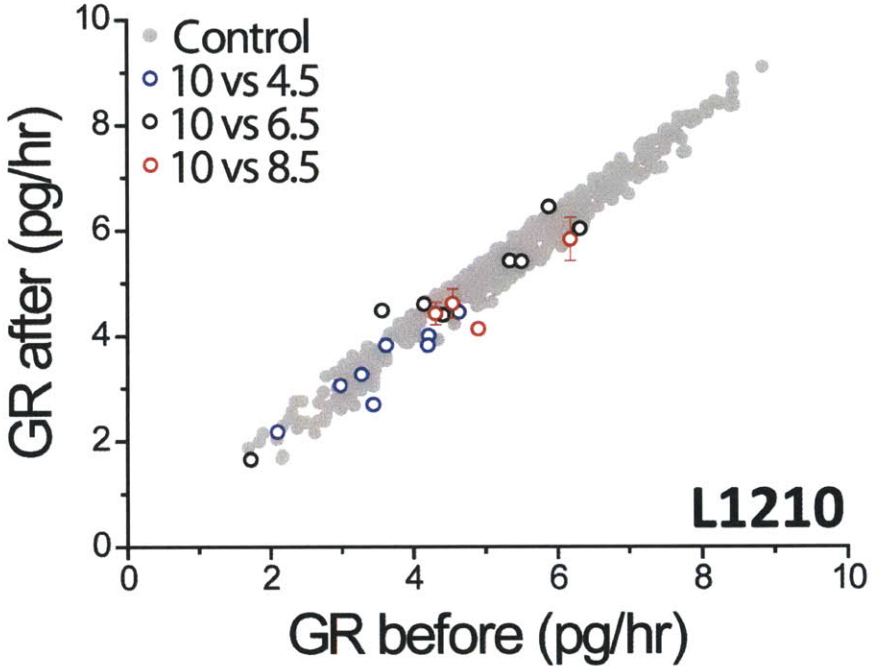

Figure 5-6: Environmental exchange positive control. Depletions took place in multiple glucose concentrations all above physiological level. Red circles include the error of growth rate estimation.

5.2 Growth response to nutrient depletion

Glucose and glutamine are the key substrates for anabolic and energetic metabolism of actively growing cells. Expectedly, bulk culture showed severely reduced proliferation upon depletion of those nutrients (Fig 5-7 A, B). However, the bulk volume trajectories of glucose and glutamine depletions showed distinct characteristics (Fig 5-7 C, D), which may imply that the responses could be driven by two different mechanisms. For example, glucose depleted culture showed transiently increased volume, suggesting that growth can be temporally sustained without glucose even after cell division cycle is arrested. On the other hand, cells deprived of glutamine decreased their volume in relatively short time scale (about

half of culture doubling time), which suggests that cells may have gone through atrophy. It is possible that glutamine is indispensable for cell growth since it is an exclusive source of nitrogen, whereas cells deprived of glucose may be able to use alternative carbon sources to survive on the short-term. In the long-term depletion, however, vast amount of reactions and signaling can be altered, making it hard to understand the driving mechanisms of the response.

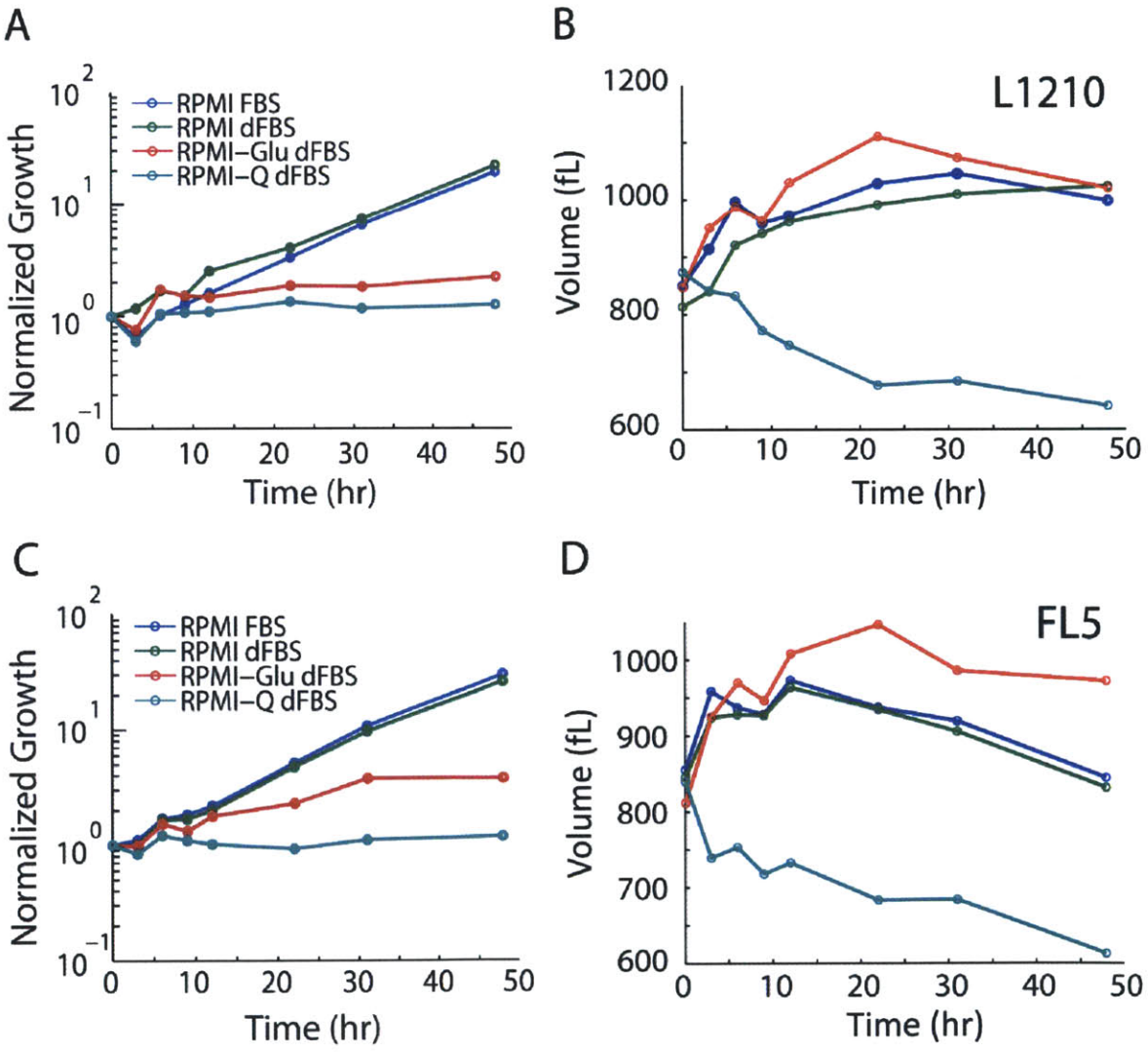

Figure 5-7: Bulk culture proliferation or volume curves for depletions of glucose (A, B) and glutamine (C, D) in L1210 and FL5.12 cell lines, compared to controlled growth in standard culture conditions (RPMI FBS) and culture conditions utilizing dialyzed FBS (RPMI dFBS).

It is possible that short-term growth response to nutrient depletion captures the essence of reactions and signaling involved in a particular metabolism. In the simplest case where no signaling or secondary reactions are associated with the metabolism of the given nutrient, growth slowdown to depletion will simply represent the uptake rate. On the other hand, if metabolic intermediates of a particular nutrient are involved in signaling and regulations of transporters or growth factors, growth can decrease more than what is expected from the loss of uptake. For example, a study has shown that glucose-deprived hematopoietic cells down-regulated glutamine metabolism since glucose flux through the hexosamine biosynthesis pathway regulates glutamine consumption [51]. This suggests that metabolites themselves can promote cell growth by altering cell signaling [52].

Initial glucose depletion experiments in the SMR showed a switch-like growth rate change that occurred immediately following the environmental shift (Fig 5-8). Reversibility of the response suggested that this short depletion of 30 minutes did not induce a detrimental effect permanent to cells. To quantify the magnitude of growth rate drop more thoroughly, we repeated the same experiment to more cells and compiled the initial depletion responses. As shown in Fig 5-9A, growth rate during depletion was proportional to the initial growth rate and this allowed a slope of linear fit to represent the extent of growth rate slowdown. Upon glucose depletion, L1210 and FL5.12 cells dropped growth rate by 40% and 36%, respectively (Fig 5-9A). This is several times larger than what is expected from the loss of uptake based on previous radiolabel measurements [53][54]. To confirm that our particular cell lines actually exhibit low level of glucose uptake, we measured the amount of radiolabeled glucose within L1210 cells and found it comprised only about 3% of cell mass (data not shown). Upon glutamine depletion, L1210 and FL5.12 cells dropped growth rate by 29% and 28%, respectively (Fig 5-9B). This is also much larger than previously known amount of glutamine uptake [55]. Radiolabel of glutamine carbon showed that glutamine comprises about 5% of cell mass. These large growth responses exceeding the uptake suggest that nutrient depletion induced several alterations in cell signaling and in turn more severe growth slowdown.

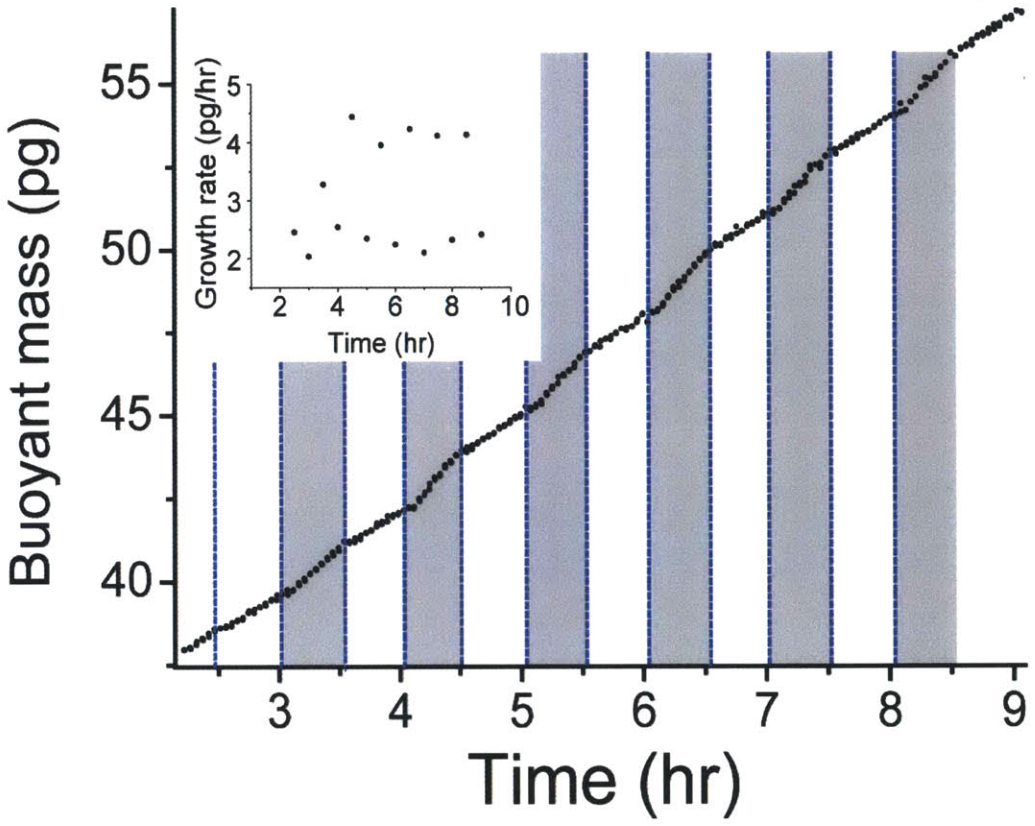

Figure 5-8: Instantaneous growth response to partial nutrient depletion. Growth of FL5.12 cell was measured as cells alter between the media supplemented either with 2mM (grey) or 0.5mM glucose (white). Alterations occurred every 30 minutes. Inset) Instantaneous growth rate of each section was detertmined by linear fit.

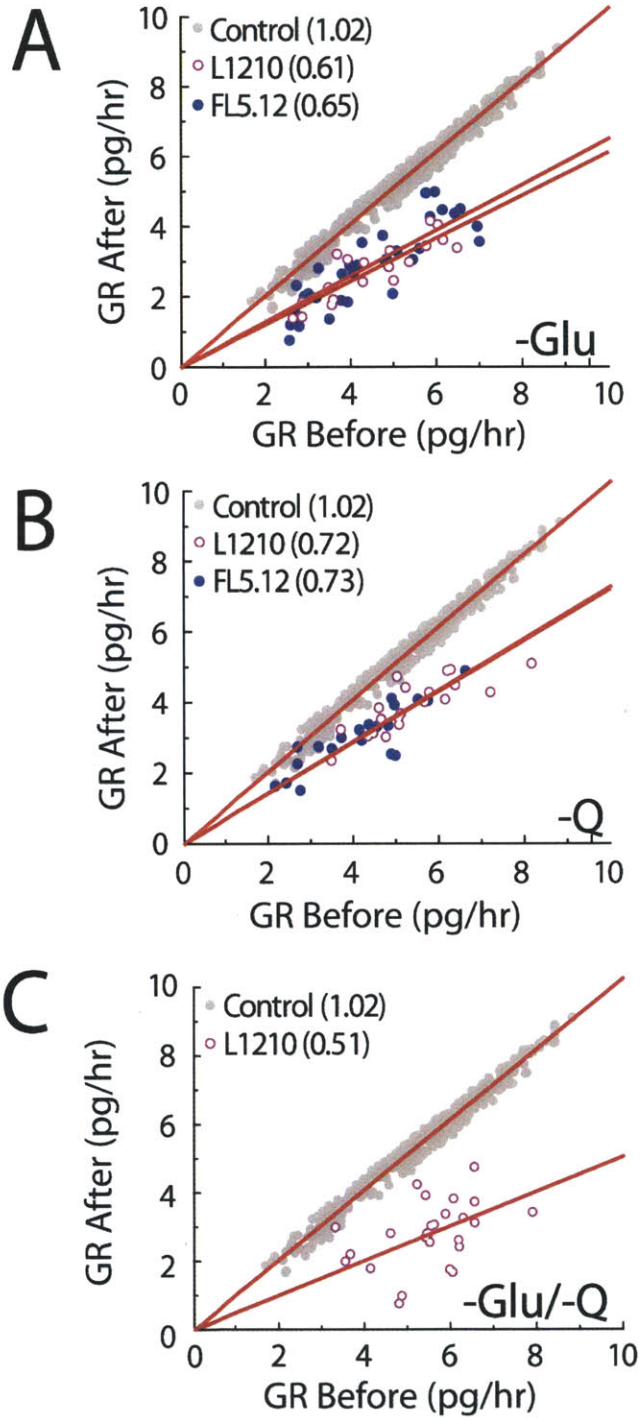

Figure 5-9: Growth rate change upon complete depletions of specific nutrients. Both L1210 and FL5.12 cells were depleted of glucose (A), glutamine (B), or both substrates (C). Red lines show the linear fit and the slope is shown in the legend.

It may be possible to find how much of signaling overlaps between glucose and glutamine by depleting both and comparing to the response from single depletions. Depletion of both glucose and glutamine on L1210 cells dropped growth rate by 50% of the initial rate, far less than an additive response of ~69% (Fig 5-9C, 10). This suggests that signaling of glucose and glutamine metabolism shares the large portion but not all.

It is noteworthy that growth response of either depletion demonstrates no correlation to cell size or cell cycle position, despite previous work showing variable glucose and glutamine uptake over the cell cycle [56]. Even though the amount of uptake can vary with cell cycle, it is possible that their role in sustaining growth by signaling may remain crucial throughout the whole cell cycle.

By exploiting this instantaneous growth response as a 'cell signaling sensor', we envision to quantify the role of metabolites in sustaining growth beyond merely constituting mass. High-throughput screening of growth response to depletions of various metabolites may find certain nutrients crucial in growth regardless of their low uptake level [57]. Furthermore, when the metabolomic profiles measured by growth response are compared in many different cells it has a potential to provide a new metric of cell characterization.

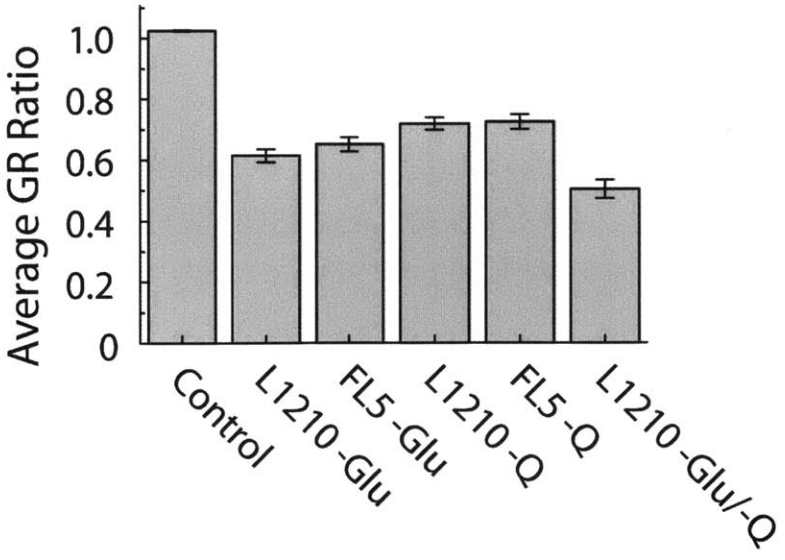

Figure 5-10: Average growth rate change upon nutrient depletions. Error bars show the error of slope from the linear fit shown in Fig 5-9.

Appendix A

Supplementary Figures

A.1 Chapter 2 Supplementary Figures

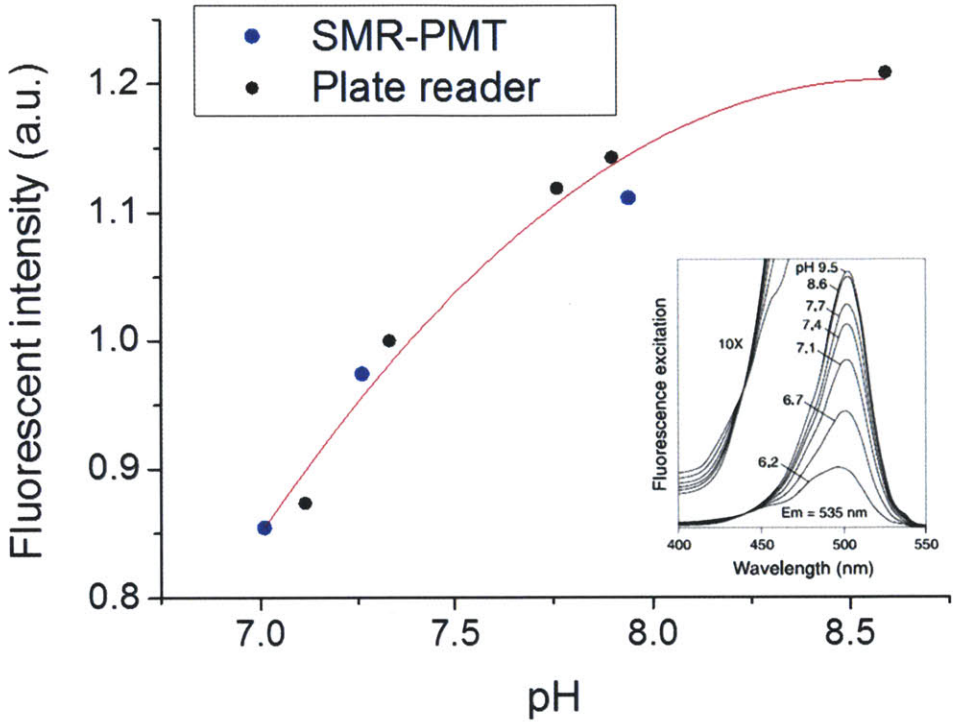

Figure A-1. BCECF calibration. 10ug/ml of BCECF was mixed in buffers of varying pH and the fluorescence was measured either by SMR-PMT or a plate reader (Tecan). In the plate reader, the emission (detected at 525nm) from ~475nm excitation was normalized by the emission from excitation of its isosbestic point (~450nm). With the SMR, only one excitation (475nm) was used and the emission was detected at 525nm. Measurements from two different systems were normalized using different normalization factors and combined for 2nd order polynomial fit. This fit was used to determine the pH when the fluorescent intensity was measured from the SMR-PMT system.

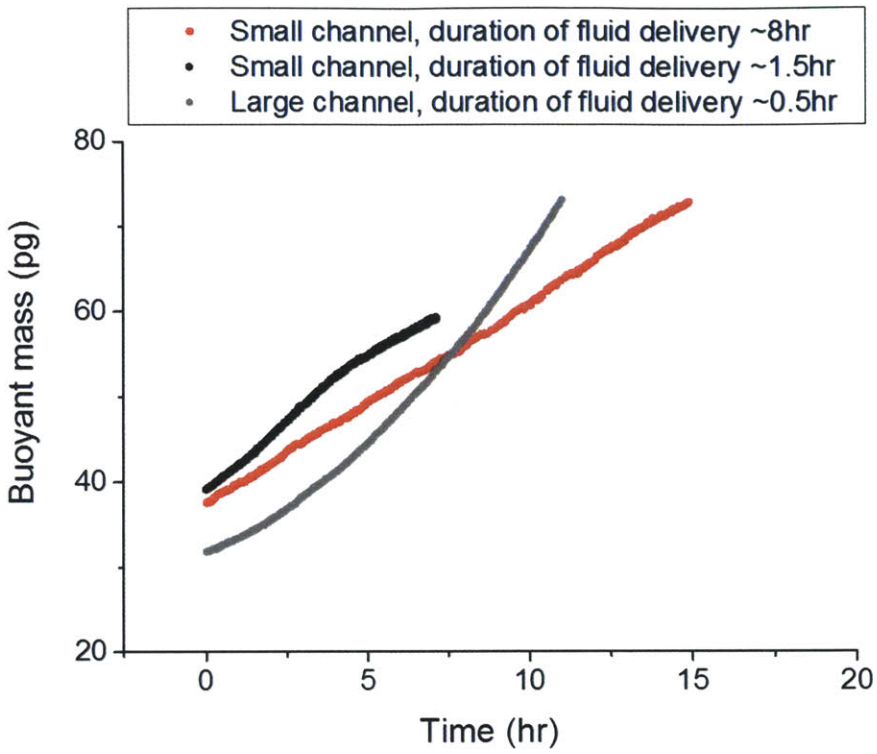

Figure A-2. Growth of FL5.12 cells under different type of stress. Black line shows the growth when shear stress is a dominant detrimental factor. Red line shows the growth when the elevated pH is a dominant detrimental factor. Grey shows a healthy growth.

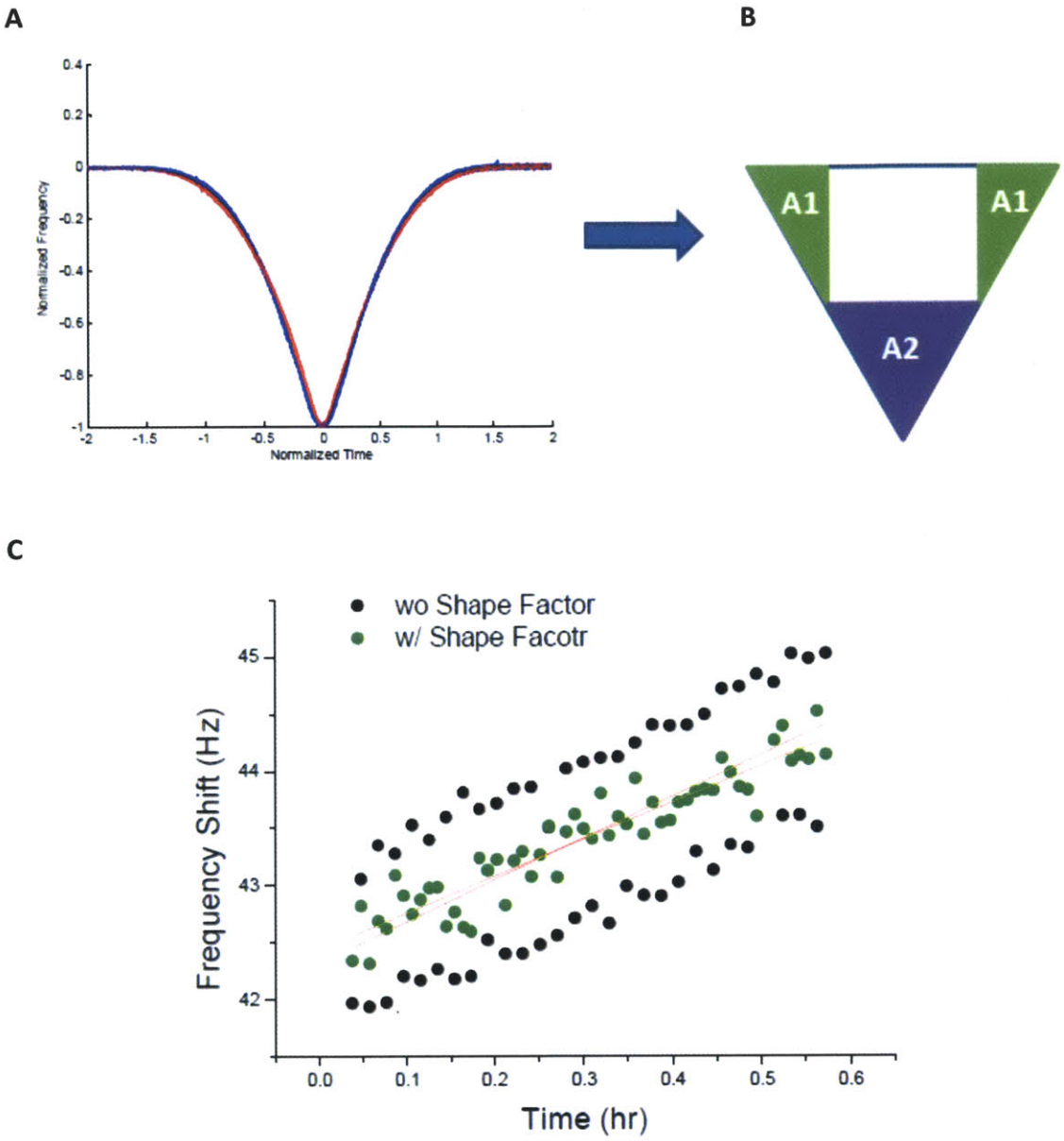

Figure A-3. Peak shape as a determinant of the path of cell transit. A. Peaks from the same cell trapped in two different extreme paths show distinct shapes (red – inner turn, blue – outer turn). B. To quantify the peak shape associated with cell transit path, area of the part of peak (green and violet) was calculated as shown in the illustration. C. The height of peaks from cell passage of two different paths (black) was compensated by using the shape factor obtained from A1/A2 in B (green).

A.2 Chapter 4 Supplementary Figures

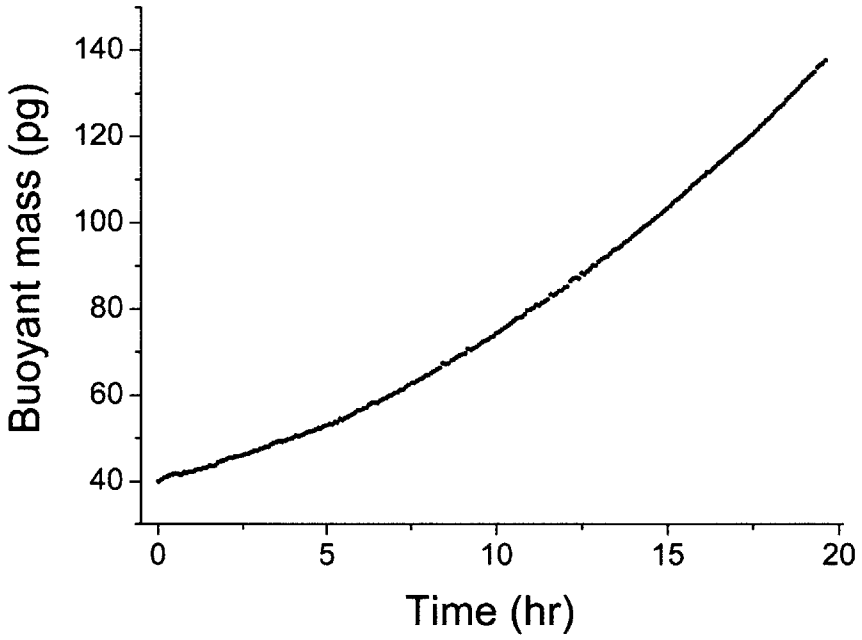

Figure A-4: A giant cell. A cell loaded into the serpentine channel SMR through the posts at the entry grew a few cycles without division and accumulated almost 4 times the initial mass.

A.3 Chapter 5 Supplementary Figures

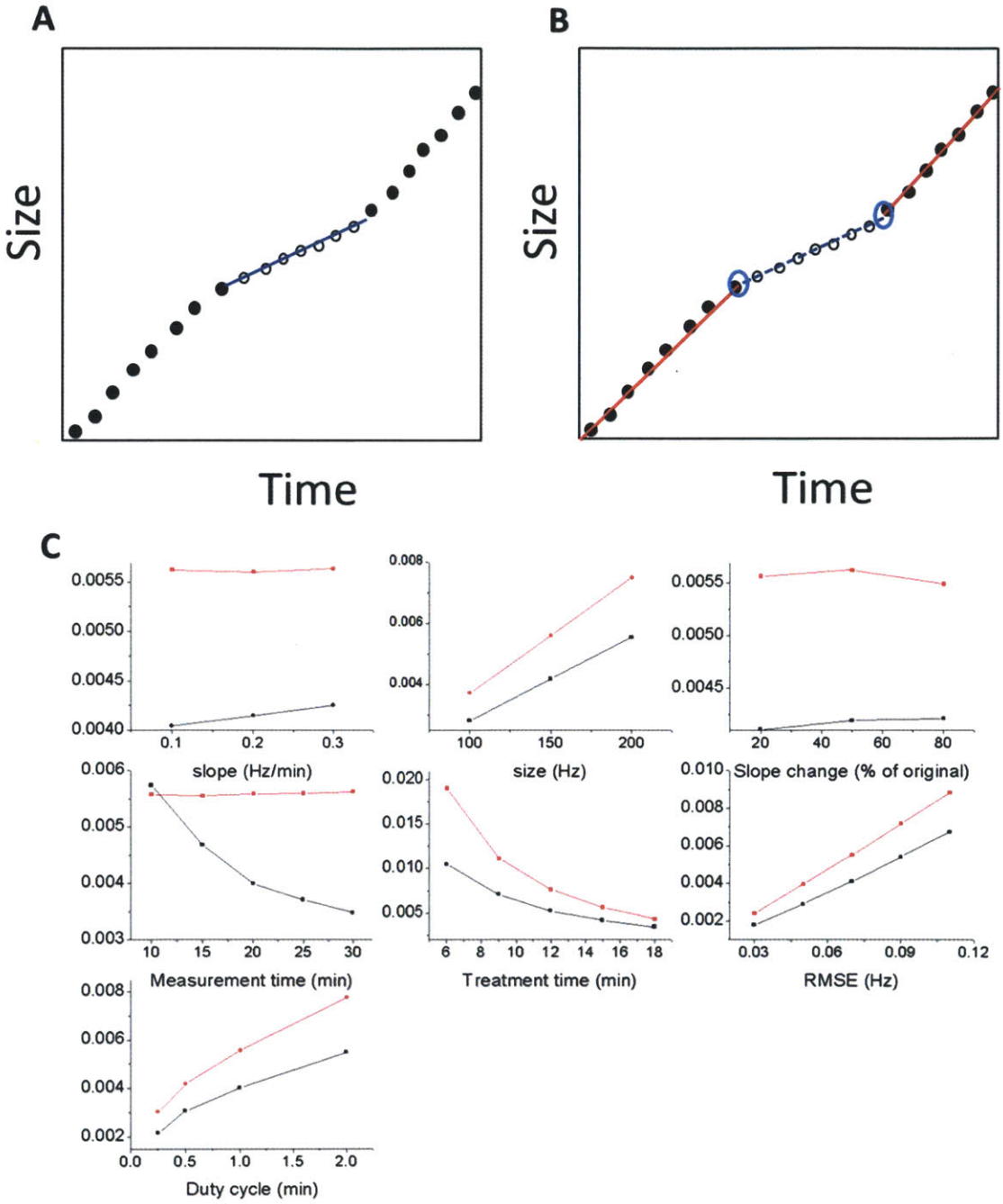

Figure A-5. Instantaneous growth rate estimation error in two different approaches. To estimate the slope of depleted region, scheme A applies a linear fit directly to the depleted portion (closed circle – growth in rich media, open circle – growth in depleted media, blue line – linear fit). Scheme B fits the portion before and after depletion (red lines) to estimate the size of end points (blue circle). The slope of depleted portion is then estimated by extrapolating from the two points (blue dotted line). C) the error of slope estimation (a.u.) is simulated for various parameters.

Bibliography

[1] S. W. Sherwood, D. Rush, J. L. Ellsworth, and R. T. Schimke, "Defining cellular senescence in IMR-90 cells: a flow cytometric analysis," *Proceedings of the National Academy of Sciences*, vol. 85, no. 23, pp. 9086-9090, 1988.

[2] G. C. Johnston, J. R. Pringle, and L. H. Hartwell, "Coordination of growth with cell division in the yeast Saccharomyces cerevisiae.," *Experimental Cell Research*, vol. 105, no. 1, p. 79, 1977.

[3] J. B. Moseley, A. Mayeux, A. Paoletti, and P. Nurse, "A spatial gradient coordinates cell size and mitotic entry in fission yeast," *Nature*, vol. 459, no. 7248, pp. 857-860, Jun. 2009.

[4] L. H. Hartwell and M. W. Unger, "Unequal division in Saccharomyces cerevisiae and its implications for the control of cell division.," *The Journal of Cell Biology*, vol. 75, no. 2, pp. 422-435, Nov. 1977.

[5] S. Gasser, "Visualizing chromatin dynamics in interphase nuclei," *Science*, Jan. 2002.

[6] A. Zetterberg, "A quantitative cytochemical investigation of the relationship between cell mass and initiation of DNA synthesis in mouse fibroblasts in vitro.," *Experimental Cell Research*, vol. 40, no. 1, pp. 12-20, Oct. 1965.

[7] T. O. Fox and A. B. Pardee, "Animal cells: noncorrelation of length of G1 phase with size after mitosis.," *Science*, vol. 167, no. 3914, pp. 80-82, Jan. 1970.

[8] I. conlon and M. raff, "Differences in the way a amammalian cell and yeast cells coordinate cell growth and cell-cycle progression," *Journal of biology*, pp. 1-10, May 2003.

[9] J. M. Mitchison, "Growth during the cell cycle," *International review of cytology*, vol. 226, pp. 165-258, 2003.

[10] R. F. Brooks and R. Shields, "Cell growth, cell division and cell size homeostasis in Swiss 3T3 cells.," *Experimental Cell Research*, vol. 156, no. 1, pp. 1-6, Jan. 1985.

[11] A. Zetterberg, "Quantitative cytochemical studies on interphase growth. II. Derivation of synthesis curves from the distribution of DNA, RNA and mass values of individual mouse fibroblasts in vitro.," *Experimental Cell Research*, vol. 39, no. 1, pp. 22-32, Aug. 1965.

[12] A. Tzur, R. Kafri, V. S. LeBleu, G. Lahav, and M. W. Kirschner, "Cell Growth and Size Homeostasis in Proliferating Animal Cells," *Science*, vol. 325, no. 5937, pp. 167-171, Jul. 2009.

[13] P. Echave, I. J. Conlon, and A. C. Lloyd, "Cell size regulation in mammalian cells.," *Cell cycle (Georgetown, Tex.)*, vol. 6, no. 2, pp. 218-224, Jan. 2007.

[14] M. Leslie, "Mysteries of the cell. How does a cell know its size?," *Science*, vol. 334, no. 6059, pp. 1047-1048, 25-Nov.-2011.

[15] S. Y. Lunt and M. G. vander Heiden, "Aerobic Glycolysis: Meeting the Metabolic Requirements of Cell Proliferation," *Annu Rev Cell Dev Biol*, vol. 27, no. 1, pp. 441-464, Nov. 2011.

[16] M. G. vander Heiden, L. C. Cantley, and C. B. Thompson, "Understanding the Warburg effect: the metabolic requirements of cell proliferation," *Science Signalling*, vol. 324, no. 5930, p. 1029, 2009.

[17] G. Windt and Pearce, "Metabolic switching and fuel choice during T-cell differentiation and memory development," *Immunological Reviews*, Jan. 2012.

[18] R. Lockart and H. Eagle, "Requirements for growth of single human cells.," *Science (New York*, Jan. 1959.

[19] S. Cooper, *BMC Cell Biology*, vol. 5, no. 1, p. 35, 2004.

[20] S. D. Di Talia, J. M. Skotheim, J. M. Bean, E. D. Siggia, and F. R. Cross, "The effects of molecular noise and size control on variability in the budding yeast cell cycle," *Nature*, vol. 448, no. 7156, pp. 947-951, Aug. 2007.

[21] H. Davies and M. Wilkins, "Interference microscopy and mass determination," *Nature*, Jan. 1952.

[22] T. P. Burg, M. Godin, S. M. Knudsen, W. Shen, G. Carlson, J. S. Foster, K. Babcock, and S. R. Manalis, "Weighing of Biomolecules, Single Cells and Single Nanoparticles in Fluid," *Nature*, vol. 446, no. 7139, pp. 1066-1069, Apr. 2007.

[23] K. L. Ekinci, "Ultimate limits to inertial mass sensing based upon nanoelectromechanical systems," *Journal of Applied Physics*, vol. 95, no. 5, p. 2682, Jan. 2004.

[24] M. Godin, F. F. Delgado, S. Son, W. H. Grover, A. K. Bryan, A. Tzur, P. Jorgensen, K. Payer, A. D. Grossman, M. W. Kirschner, and S. R. Manalis, "Using buoyant mass to measure the growth of single cells," *Nature Methods*, vol. 7, no. 5, pp. 387-390, Apr. 2010.

[25] V. Lecault, M. VanInsberghe, S. Sekulovic, D. J. H. F. Knapp, S. Wohrer, W. Bowden, F. Viel, T. McLaughlin, A. Jarandehei, M. M. Miller, D. Falconnet, A. K. White, D. G. Kent, M. R. Copley, F. Taghipour, C. J. Eaves, R. K. Humphries, J. M. Piret, and C. L. Hansen, "High-throughput analysis of single hematopoietic stem cell proliferation in microfluidic cell culture arrays," *Nature Methods*, pp. 1-9, May 2011.

[26] J. C. McDonald and G. M. Whitesides, "Poly(dimethylsiloxane) as a Material for Fabricating Microfluidic Devices," *Accounts of Chemical Research*, vol. 35, no. 7, pp. 491-499, Jul. 2002.

[27] Y. Chisti, "Hydrodynamic damage to animal cells," *Critical reviews in biotechnology*, Jan. 2001.

[28] Nikon, "Maintaining Live Cells on the Microscope Stage," *MicroscopyU online*

[29] J. McCubrey and B. Fagg, "Enrichment of hematopoietic precursor cells and cloning of multipotential B-lymphocyte precursors," in *Proceedings of the*, 1985.

[30] J. Lee, A. K. Bryan, and S. R. Manalis, "High precision particle mass sensing using microchannel resonators in the second vibration mode," *Review of Scientific Instruments*, vol. 82, no. 2, p. 023704, Jan. 2011.

[31] Y. Tseytlin, "High resonant mass sensor evaluation: An effective method," *Review of Scientific Instruments*, Jan. 2005.

[32] R. Chunara, "Electronic Readout of Microchannel Resonators for Precision Mass Sensing in Solution," *MIT* doctoral thesis. May. 2010.

[33] "Key Numbers for Cell Biologists," www.Bionumbers.org, Jul. 2010.

[34] A. Sakaue-Sawano, H. Kurokawa, T. Morimura, A. Hanyu, H. Hama, H. Osawa, S. Kashiwagi, K. Fukami, T. Miyata, H. Miyoshi, T. Imamura, M. Ogawa, H. Masai, and A. Miyawaki, "Visualizing Spatiotemporal Dynamics of Multicellular Cell-Cycle Progression," *Cell*, vol. 132, no. 3, pp. 487-498, Feb. 2008.

[35] J. warner, "The economics of ribosome biosynthesis in yeast," *TIBS*, pp. 1-4, Oct. 1999.

[36] W. A. Wells, "Does size matter?," *The Journal of Cell Biology*, vol. 158, no. 7, pp. 1156-1159, Sep. 2002.

[37] P. Fantes and P. Nurse, "Control of cell size at division in fission yeast by a growth-modulated size control over nuclear division.," *Experimental Cell Research*, vol. 107, no. 2, pp. 377-86, Jul. 1977.

[38] P. Nurse, "Cell cycle control--both deterministic and probabilistic?," *Nature*, vol. 286, no. 5768, pp. 9-10, Jul. 1980.

[39] R. P. das Neves, N. S. Jones, L. Andreu, R. Gupta, T. Enver, and F. J. Iborra, "Connecting Variability in Global Transcription Rate to Mitochondrial Variability," *PLoS Biol*, vol. 8, no. 12, p. e1000560, Dec. 2010.

[40] J. T. Chang, V. R. Palanivel, I. Kinjyo, F. Schambach, A. M. Intlekofer, A. Banerjee, S. A. Longworth, K. E. Vinup, P. Mrass, J. Oliaro, N. Killeen, J. S. Orange, S. M. Russell, W. Weninger, and S. L. Reiner, "Asymmetric T Lymphocyte Division in the Initiation of Adaptive Immune Responses," *Science*, vol. 315, no. 5819, pp. 1687-1691, Mar. 2007.

[41] E. D. Hawkins, J. F. Markham, L. P. McGuinness, and P. D. Hodgkin, "A single-cell pedigree analysis of alternative stochastic lymphocyte fates," *Proceedings of the National Academy of Sciences*, vol. 106, no. 32, pp. 13457-13462, Aug. 2009.

[42] K. R. Duffy, C. J. Wellard, J. F. Markham, J. H. S. Zhou, R. Holmberg, E. D. Hawkins, J. Hasbold, M. R. Dowling, and P. D. Hodgkin, "Activation-Induced B Cell Fates Are Selected by Intracellular Stochastic Competition," *Science*, vol. 335, no. 6066, pp. 338-341, Jan. 2012.

[43] F. B. Furnari, T. Fenton, R. M. Bachoo, A. Mukasa, J. M. Stommel, A. Stegh, W. C. Hahn, K. L. Ligon, D. N. Louis, C. Brennan, L. Chin, R. A. DePinho, and W. K. Cavenee, "Malignant astrocytic glioma: genetics, biology, and paths to treatment," *Genes & Development*, vol. 21, no. 21, pp. 2683-2710, Nov. 2007.

[44] S. Singh, C. Hawkins, I. Clarke, J. Squire, and J. Bayani, "Identification of human brain tumour initiating cells", *Nature*, Jan. 2004.

[45] M. G. von Muhlen, N. D. Brault, S. M. Knudsen, S. Jiang, and S. R. Manalis, "Label-Free Biomarker Sensing in Undiluted Serum with Suspended Microchannel Resonators", *Analytical Chemistry*, vol. 82, no. 5, pp. 1905-1910, Mar. 2010.

[46] Y. Song, T. Hahn, I. P. Thompson, T. J. Mason, G. M. Preston, G. Li, L. Paniwnyk, and W. E. Huang, "Ultrasound-mediated DNA transfer for bacteria", *Nucleic Acids Research*, vol. 35, no. 19, pp. e129-e129, Oct. 2007.

[47] T. Burg, J. Sader, and S. Manalis, "Nonmonotonic Energy Dissipation in Microfluidic Resonators", *Physical Review Letters*, vol. 102, no. 22, Jun. 2009.

[48] W. Tan and S. Takeuchi, "A trap-and-release integrated microfluidic system for dynamic microarray applications", *of the National Academy of Sciences*, Jan. 2007.

[49] M. G. vander Heiden, D. R. Plas, J. C. Rathmell, C. J. Fox, M. H. Harris, and C. B. Thompson, "Growth factors can influence cell growth and survival through effects on glucose metabolism.", *Molecular and Cellular Biology*, vol. 21, no. 17, pp. 5899-912, Sep. 2001.

[50] Y. Weng, K. C. Wood, S. Son, D. M. Sabatini, and S. Manalis, "Measuring the dynamics of single-cell growth in response to drug therapy", *Submitted*, pp. 1-13, Jul. 2012.

[51] K. E. Wellen, C. Lu, A. Mancuso, J. M. S. Lemons, M. Ryczko, J. W. Dennis, J. D. Rabinowitz, H. A. Coller, and C. B. Thompson, "The hexosamine biosynthetic pathway couples growth factor-induced glutamine uptake to glucose metabolism", *Genes & Development*, vol. 24, no. 24, pp. 2784-2799, Dec. 2010.

[52] P. Ward and C. Thompson, "Metabolic Reprogramming: A Cancer Hallmark Even Warburg Did Not Anticipate", *Cancer Cell*, vol. 21, no. 3, pp. 297-308, Mar. 2012.

[53] J. J. Lum, D. E. Bauer, M. Kong, M. H. Harris, C. Li, T. Lindsten, and C. B. Thompson, "Growth Factor Regulation of Autophagy and Cell Survival in the Absence of Aptosis", *Cell*, vol. 120, no. 2, pp. 237-248, Jan. 2005.

[54] Hume, J. Radik, and E. Ferber, "Aerobic glycolysis and lymphocyte transfomation", *Biochemical*, Jan. 1978.

[55] P. Newsholme and E. A. Newsholme, "Rates of utilization of glucose, glutamine and oleate and formation of end-products by mouse peritoneal macrophages in culture.", *The Biochemical journal*, vol. 261, no. 1, pp. 211-8, Jul. 1989.

[56] S. L. Colombo, M. Palacios-Callender, N. Frakich, S. Carcamo, I. Kovacs, S. Tudzarova, and S. Moncada, "Molecular basis for the differential use of glucose and glutamine in cell proliferation as revealed by synchronized HeLa cells", *Proceedings of the National Academy of Sciences*, vol. 108, no. 52, pp. 21069-21074, 2011.

[57] M. Jain, R. Nilsson, S. Sharma, N. Madhusudhan, T. Kitami, A. L. Souza, R. Kafri, M. W. Kirschner, C. B. Clish, and K. V. Mootha, "Metabolite Profiling Identifies a Key Role for Glycine in Rapid Cancer Cell Proliferation", *Science*, vol. 336, no. 6084, pp. 1040-1044, May 2012.